

Melanie Mucke

**Employing electron-electron coincidence techniques to investigate  
the autoionisation of clusters**

**IPP 16/23  
2012**

# **Employing electron-electron coincidence techniques to investigate the autoionisation of clusters**

vorgelegt von  
Diplom-Physikerin  
Melanie Mucke  
aus Berlin

Von der Fakultät II - Mathematik und Naturwissenschaften  
der Technischen Universität Berlin  
zur Erlangung des akademischen Grades  
Doktor der Naturwissenschaften  
- Dr. rer. nat. -  
genehmigte Dissertation

Promotionsausschuß:  
Vorsitzender: Prof. Dr. Mario Dähne  
Gutachter: PD Dr. Uwe Hergenroth  
Gutachter: Prof. Dr. Thomas Möller

Tag der wissenschaftlichen Aussprache: 18.04.2011

Berlin 2011  
D83



## abstract

The topic of this thesis is the investigation of a non-local decay channel, the so-called interatomic, or intermolecular, Coulombic decay (ICD). This autoionisation process occurs only in weakly bound, extended systems where an excited electron of one atom is offered a de-excitation channel via a neighbouring atom. In order to unambiguously prove the existence of ICD on further van-der-Waals or hydrogen-bound systems, and to record energy spectra of the ICD electrons, a new coincidence technique was employed. To do so, a new magnetic bottle electron spectrometer, embedded in a new vacuum set-up and completed with a new water cluster source, was constructed and successfully launched.

Within the scope of this thesis, different rare gas clusters were investigated. For pure neon clusters a shift of the ICD energy spectrum according to the cluster size could be shown. For large clusters, the spectrum does not extend down to zero eV. Furthermore, evidence for the occurrence of ICD from neon satellite states has been found.

Also, it was possible to clearly show ICD in mixed neon-krypton clusters. Here, the ICD electron possesses an unusual high energy. It is assumed that these clusters are present in form of a krypton core surrounded by a neon layer. Enriching the gas mixture with krypton, the ICD spectra develop a shoulder, which can be attributed to a change in coordination number of the neon atoms.

Furthermore, mixed argon-xenon clusters were investigated. For this system, theoreticians expect a competition between two autoionisation processes, namely the electron transfer mediated decay (ETMD) and ICD. The latter decay channel is only opened above a certain cluster size, which seemingly has been exceeded in our experiments. Therefore, an observation of this process is assumed.

Investigations of water clusters have shown, that, according to theory, ICD occurs also in hydrogen-bound systems. The decay leads to an efficient generation of low-energy electrons which could turn out as not at all unimportant with respect to radiation induced damage of DNA.

Comparative measurements on deuterated water clusters also demonstrate the existence of ICD. With respect to the energy spectra, only minor differences could be observed.



# Kurzfassung

Anwendung von Elektron-Koinzidenz-Meßtechniken zur Untersuchung der Autoionisation von Clustern

Die Arbeit beschäftigt sich mit der Untersuchung eines nichtlokalen Relaxationskanals, dem interatomaren bzw. intermolekularen Coulomb-Zerfall (ICD). Dieser Autoionisationsprozeß tritt nur in schwach gebundenen, ausgedehnten Systemen auf, in denen für ein angeregtes Elektron eines Atoms ein Zerfallskanal über ein benachbartes Atom offensteht.

Um die Existenz von ICD an weiteren van-der-Waals- oder Wasserstoffbrücken- gebundenen Systemen eindeutig nachweisen und Spektren der ICD Elektronen aufnehmen zu können, wurde eine neuartige Koinzidenzmeßtechnik angewandt. Hierfür wurde ein magnetische Flasche Spektrometer, eingebettet in eine Vakuumapparatur und ergänzt durch eine Wasserclusterquelle, konstruiert und erfolgreich in Betrieb genommen.

Im Rahmen der Arbeit wurden verschiedene Edelgascluster untersucht. Bei reinen Neonclustern konnte gezeigt werden, daß sich das Energiespektrum des ICD-Elektrons abhängig von der Clustergröße verschiebt und bei größeren Clustern nicht bis null eV reicht. Außerdem haben sich Hinweise auf ICD von Satellitenzuständen in Neonclustern ergeben.

In gemischten Neon-Krypton-Clustern konnte ebenfalls eindeutig ein ICD-Signal nachgewiesen werden. Das ICD-Elektron weist hier die Besonderheit einer ungewöhnlich hohen Energie auf. Man vermutet, daß diese Cluster in Form eines Kryptonkerns umgeben von einer Neonschicht vorliegen. Bei erhöhtem Krypton-gehalt in der Gasmischung ist das Entstehen einer Schulter am ICD-Peak zu beobachten, die auf eine veränderte Koordination der Neonatome zurückgeführt wird.

Desweiteren wurden gemischte Argon-Xenon-Cluster untersucht. In diesen Clustern gehen Theoretiker von einer Konkurrenz zwischen zwei Autoionisationsprozessen, dem ‘electron transfer mediated decay’ (ETMD) und dem ICD aus. Letzterer ist erst ab einer bestimmten Größe möglich, die offenbar in unseren Experimenten überschritten wurde, so daß von einer Beobachtung des Prozesses ausgegangen wird.

Die Untersuchung von Wasserclustern hat gezeigt, daß, gemäß der theoretischen Vorhersage, ICD auch in Wasserstoffbrücken-gebundenen Systemen auftritt. Er führt zu einer effizienten Erzeugung von niederenergetischen Elektronen, die sich als nicht unbedeutend für durch Strahlung erzeugte DNA-Schäden herausstellen könnten.

Vergleichende Messungen an deuterierten Wasserclustern demonstrierten ebenfalls die Existenz von ICD. Es zeigen sich nur geringe Unterschiede in den Energiespektren der ICD-Elektronen.

# Contents

<b>1</b>	<b>introduction</b>	<b>7</b>
<b>2</b>	<b>basics</b>	<b>9</b>
2.1	clusters . . . . .	10
2.2	photoionisation . . . . .	15
2.2.1	single photoionisation . . . . .	15
2.2.2	photo double ionisation . . . . .	19
2.3	autoionisation . . . . .	23
2.3.1	Auger decay . . . . .	23
2.3.2	intermolecular Coulombic decay . . . . .	25
2.3.3	electron transfer mediated decay . . . . .	29
<b>3</b>	<b>experimental</b>	<b>33</b>
3.1	light source . . . . .	34
3.2	vacuum set-up . . . . .	38
3.2.1	magnetic bottle spectrometer . . . . .	38
3.2.2	‘old’ bottle . . . . .	39
3.2.3	new magnetic bottle spectrometer . . . . .	40
3.2.4	vacuum chamber . . . . .	46
3.2.5	cluster generation . . . . .	53
3.3	from experiment to spectrum . . . . .	56
3.3.1	electronics . . . . .	56
3.3.2	coincidence technique . . . . .	58
3.3.3	beamtime . . . . .	62

<b>4</b>	<b>rare gas clusters</b>	<b>65</b>
4.1	neon clusters . . . . .	65
4.2	neon-krypton clusters . . . . .	72
4.3	argon-xenon clusters . . . . .	80
<b>5</b>	<b>water clusters</b>	<b>89</b>
5.1	ICD in water clusters . . . . .	91
5.2	clusters from heavy water . . . . .	96
<b>6</b>	<b>conclusion</b>	<b>101</b>
<b>A</b>	<b>technical drawings</b>	<b>105</b>
	<b>references</b>	<b>143</b>

# Chapter 1

## introduction

*What happens if light meets matter?*

This is certainly one of the most important questions asked in natural sciences for centuries now. And for many decades, photoelectron spectroscopy keeps delivering answers to this question by recording the electrons generated when irradiating matter with photons. Constantly improving the spectroscopic methods allows to go deeper and deeper into detail and to add more information to the whole picture that we have of how nature works.

After absorption of a photon, a system is left in an excited state, being anxious to give off its surplus energy in order to reach an energetically more favourable state. This is possible in two ways: radiative by emission of photons and non-radiative. In the latter case, the molecule transmits the excess energy either to a bath via collisions or transforms it into translational energy by fragmentation which includes emission of an electron. This thesis is an attempt to shed more light on one of the non-radiative decay paths, the so-called interatomic (or intermolecular) Coulombic decay (ICD). It is an autoionisation process which proceeds similar to the well-known Auger decay: An inner valence hole left after ionisation is filled by relaxation of an outer valence electron, and the released energy is used to ionise an outer valence electron from a neighbouring atom (molecule). This process takes place within femtoseconds and is assumed to dominate all slower decay processes as soon as it becomes energetically possible. In contrast to Auger decay, where a core hole is filled by a valence electron and another valence electron of the same monomer is ionised, ICD is a non-local process. This means that it cannot take place in an isolated atom or molecule but demands an environment. This environment is constituted by neighbouring atoms/ molecules which, in our case, are bound to the initial one by van der Waals forces or hydrogen bonds. This aggregate is called a cluster.

Clusters constitute the intermediate between an isolated atom or molecule and the corresponding condensed phase. Investigating clusters is significant for un-

derstanding the interatomic/ intermolecular interactions and explores how the properties of a material gradually change upon enlargement of the system.

The first step in exploring a new field of research is done by choosing a test system which is as easy as possible before moving towards more challenging and scientifically more relevant objects. Rare gases present such model systems: they are well understood both experimentally and theoretically, and their clusters are relatively easy to produce. The ICD process has first been observed by our group on rare gas clusters, and theoretical predictions were confirmed by the experiment. Investigating the autoionisation of heterogeneous rare gas clusters is of additional interest with respect to structure determination. For this purpose, the change of the ICD characteristics in dependence on cluster composition and size was analysed. Furthermore, experiments were extended into the molecular direction, and water clusters moved into the focus of our research. Water is not only interesting as a liquid itself, but understanding it forms the basis of biologically relevant research. One of the questions stimulating research on water is whether low energetic electrons as generated by ICD contribute to radiation-induced damage of DNA.

My thesis is organised in the following way: To begin with, an introduction to clusters and their production is given in chapter 2.1. It is followed by a description of photo- and autoionisation processes that play a role for the investigated systems (chapters 2.2 and 2.3).

In order to gain more information on the relaxation pathway, an electron-electron coincidence technique based on a magnetic bottle spectrometer was used. The newly constructed spectrometer together with a vacuum set-up dedicated to experiments on clusters surpasses the possibilities of conventional electron energy analysers and is described in chapter 3.2. This chapter follows a short introduction on synchrotrons which served as light source (chapter 3.1) and is completed with a description of how the signals are treated and the data are processed (chapter 3.3).

In chapter 4, the results obtained for pure neon clusters as well as for the heterogeneous systems of neon-krypton clusters and argon-xenon clusters are presented. The interesting case of ICD in water and deuterated water clusters is discussed in chapter 5.

To complete the thesis, technical drawings of the new spectrometer and vacuum parts are enclosed in the appendix.

# Chapter 2

## basics

Without light not much would happen. At least not here. Light, or speaking more generally, electromagnetic radiation is the most important ‘ingredient’ of this thesis’ work which makes use of findings more than a hundred years old. Without the discovery of photons being the particles of light and the photoelectric effect by Hertz, Hallwachs and Lenard [1–3] and the final formulation as

$$E_{kin} = h\nu - \phi \tag{2.0.1}$$

by Albert Einstein [4] this work would not have been possible, not even existed in the world of imagination.

Irradiating matter with light causes an exchange of energy. Each photon carries an amount of energy  $h\nu$  proportional to the wavelength of the light  $\nu$ , with  $h$  being Planck’s constant. In the interaction process this energy is absorbed by the material and can cause an electron to be excited or emitted. In the latter case, the so-called photoionisation process, the electron will leave the material and can be analysed by means of photoelectron spectroscopy. It was found that the emitted electron carries a certain amount of kinetic energy,  $E_{kin}$ , which depends on the photon energy used. In order to release the electron from its binding orbital a characteristic work  $\phi$  has to be performed, the amount depending on the material and the orbit the electron originates from, and the environment surrounding the site of ionisation as we will see later. Koopmans found that the ionisation potentials determined via equation 2.0.1 correspond (with only minor corrections) directly to the negative energy eigenvalues of the electronic orbitals derived by the Fock equations [5]. This allows a direct mapping of the electronic orbitals with the help of photoelectron emission spectroscopy.

## 2.1 clusters

For the purpose of this thesis not simply atoms or molecules have been investigated by means of coincidence photoelectron spectroscopy but atomic and molecular clusters. So what are clusters? And what makes them unique?

Clusters are aggregates that consist of a finite number of atoms or molecules. Their limited size makes them bridge the gap between a single atom or molecule and the infinite solid or liquid. This means that clusters allow the studying of physical and chemical properties of matter as a function of size, i. e. the number of constituent particles. Compared to the solid, in a cluster a very large fraction of the constituting particles is part of the surface as can easily be seen by the following short estimation: A spherical cluster consisting of  $N$  atoms of radius  $r$  has a radius  $R$ , so that  $N \cong (\frac{R}{r})^3$ . If one relates the surface of the cluster  $S = 4\pi R^2$  to the surface of an atom  $s = \pi r^2$  then the number of atoms forming the cluster's surface can be estimated as

$$N_S \cong \frac{S}{s} \cong 4(\frac{R}{r})^2 \cong 4N^{\frac{2}{3}}.$$

This means that a fraction  $F_S = 4N^{-\frac{1}{3}}$  of the cluster's total atoms are involved in the surface. For example, for a small icosahedral cluster consisting of 13 atoms, only one atom represents the bulk (for 'bulk' see figure 2.1) whereas 12 atoms form the surface of the cluster, which corresponds to 92 %. This makes clear, that for clusters the surface plays a much more important role than for bulk matter, and that clusters are very well suited as model systems to study surface effects.

Clusters can be produced from almost any type of atom or molecule. They are commonly divided into different groups depending on their constituting parts and bonding types. To begin with, there is the large group of metal clusters. The atoms, e. g. of a  $\text{Na}_n$  cluster, are held together by metallic bonds where the bond-forming electrons are delocalised. Binding energies are in the range of 0.5 - 3 eV. Then there is the group of ionic clusters. Their atoms usually show very large differences in electronegativity and are held together by Coulomb interaction. Their structure is cubic, as we know e. g. from  $(\text{NaCl})_n$ , and binding energies lie in the range of 1.5 - 4 eV. Another group that became popular because of the fullerenes is the group of covalently bound clusters. Here, the bonds between atoms are directed and binding energies lie between 1 and 5 eV. One type investigated in this thesis are rare gas clusters. The van der Waals interaction, which binds the atoms to one another via induced dipole-dipole interaction, is very weak, wherefore binding energies are only of the order of 0.001 - 0.3 eV per atom. A second type of clusters that was studied here are water clusters. They belong to the group of clusters formed by hydrogen bonds. The dipole-dipole interaction between the molecules is weak (although stronger than the van der

Waals interaction), with binding energies being only about 0.15 - 0.5 eV. Each water molecule can contribute to  $\frac{1}{2}$ , 1 or 2 H-bonds which has an influence on the valence electrons. Water clusters, especially larger ones, are believed to be of a cage structure [6, 7]. There are other kinds of molecular clusters as well, formed by only one (as e. g.  $(\text{CO}_2)_n$  by van der Waals interaction) or a combination of different bonding types. Typical binding energies for molecular clusters are between 0.3 and 1 eV. Finally, in the case of mixed clusters, the interaction can be of nearly any type, depending on the constituting particles. For this thesis only mixed clusters from rare gases have been investigated, which keeps the interaction in the neutral aggregate of purely van der Waals nature.

The properties of larger clusters vary according to the so-called liquid drop model and can be described by a simple scaling law  $\chi(N) \propto N^{-\frac{1}{3}}$ . In contrast to that, the properties of smaller clusters change frequently, sometimes already if only one atom is added. This behaviour is often caused by quantum effects such as electronic or geometric shell closings [8]. Imagining a cluster as a sphere being formed of layers of atoms, then a geometric shell closing is observed when the outermost layer is complete and no single atoms are found attached to the surface of the cluster. These geometric shell closings produce particularly stable cluster structures of certain sizes, the so-called ‘magic numbers’, which were first observed in mass spectra of xenon clusters [9]. The binding energy of an atom is proportional to the number of its next neighbours; therefore it is maximal at shell closings, and a single atom on a closed surface is only very weakly bound. For icosahedral clusters, the magic numbers (total number of atoms of a cluster of  $k$  layers) can easily be calculated via the number of atoms of the  $i^{\text{th}}$  layer  $n_i$ :

$$N_k = 1 + \sum_{i=1}^k n_i = 1 + \sum_{i=1}^k (10i^2 + 2) = \frac{1}{3}(10k^3 + 15k^2 + 11k + 3),$$

giving 13, 55 and 147 as the first magical numbers. As for the icosahedron the number of next neighbours is maximal, this is the preferred structure of small clusters. With increasing size, though, tensions within the cluster increase and lead to a reduction of the binding energies. For larger clusters, the cuboctahedral form is more stable; it can already be found for  $N \approx 200$  since cuboctahedrons grow more easily.

Producing clusters from materials as different as rare gases, metals and water naturally requires different cluster sources. There are various methods to produce clusters [10]: *laser ablation* of a solid material produces neutral and charged clusters [11]; the neutral and charged clusters generated by *sputtering* are generally small and hot due to the bombardment with high energetic ions; in a *magnetron* a magnetic discharge causes the vaporisation of metals producing neutral and charged clusters with a large size distribution; and finally, by using *electrospray* highly charged metal clusters can be generated [12]. Yet another path of produ-



cing neutral clusters is the molecular beam expansion, which will be explained in the following in more detail.

To generate clusters via the molecular beam expansion method (supersonic expansion) [13, 14], only few things are necessary: a volume  $V$  of the sample gas at high pressure  $p$  which is expanded through a nozzle of diameter  $d$  into a vacuum recipient. The free expansion of gas into the vacuum is an isentropic process which means that no heat is exchanged with the environment. By choosing the ideal gas as sample, a simplified theoretical description of this expansion process shall be given. The stagnation enthalpy of the gas at rest (that means before the expansion) can be written as  $H_0 = c_p T_0$ , where  $c_p$  denotes the specific heat at constant pressure, equalling  $\frac{5}{2}kT$  for an atom (with  $k$  presenting Boltzmann's constant and  $T$  the temperature). During the expansion,  $H_0$  is directly transformed into kinetic energy  $\frac{1}{2}mu^2$  of the directed gas flow (with  $m$  being the particle mass and  $u$  the flow velocity) plus a rest enthalpy  $H$  [10]. Furthermore, the originally randomly distributed velocities of the particles are equalised rapidly, which causes a severe cooling of the beam. The temperature along the gas beam drops to  $T = T_0 - \frac{mu^2}{2c_p}$ . Bearing in mind that  $k = c_p - c_v$  and introducing  $\gamma = \frac{c_p}{c_v}$  this can be formulated as

$$T = T_0 \left(1 + \frac{(\gamma - 1)M^2}{2}\right)^{-1}.$$

The Mach number  $M$  is defined as the ratio of flow velocity and speed of sound,  $\frac{u}{s}$ , so now it is easy to imagine why a beam with  $M > 1$  is called 'supersonic'<sup>1</sup>. Its square is a measure for the ratio of the directed mass flow to the thermal energy remaining in the beam [10]. As the temperature cannot fall below zero, we obtain for  $T = 0$  the maximum possible kinetic energy

$$E_{kin,max} = \frac{mu_{max}^2}{2} = c_p T_0.$$

In other words, the maximum flow velocity is only dependent on the temperature of the gas and the mass of the atoms:

$$u_{max} = \sqrt{\frac{2c_p T_0}{m}} = \sqrt{\frac{5kT_0}{m}}.$$

Due to energy and momentum conservation, at least three particles are needed to collide with each other in order to form a dimer which requires a high collision rate between the particles or, in other words, a high density of particles in the beam. The dimer then acts as the condensation nucleus for the cluster which will grow through further collisions with other particles or small aggregates. Due to the fact that each addition of a new particle to the cluster leads to the release of an amount

---

<sup>1</sup>An alternative definition states that for the nozzle diameter being larger than the mean free path  $\lambda$  the beam is supersonic whereas for  $d < \lambda$  one speaks of an effusive beam.

of energy equal to the binding energy of the added particle, the inner energy of the aggregate increases. If the cluster cannot give off some of its energy by collisions (which is only possible at the beginning of the expansion process where the density is still high enough), it can only cool by evaporating atoms which implies a decrease of its size. Because of the accumulation of energy inherent in the formation process, clusters generated in a molecular beam expansion are generally considered to be hot. In order to reduce their vibrational and rotational energy and produce ultracold clusters, one could use the seeded beam technique. Here a carrier gas, e. g. helium, is added which removes the surplus energy, thus preventing atoms from being evaporated. This results in a stabilisation of the clusters. Moreover, it has the advantage that a lower partial pressure of the sample gas is needed.

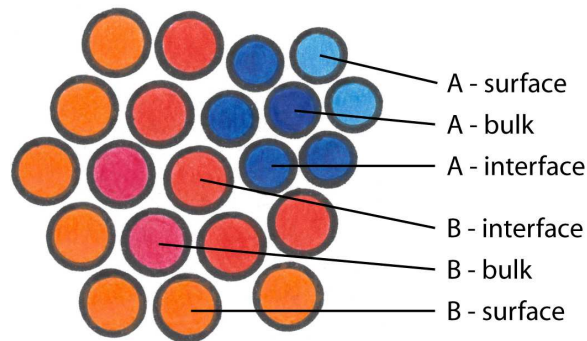


Figure 2.1: An example for a mixed cluster consisting of atoms of kind A and B. Bulk atoms are completely surrounded by next neighbours of their own kind, interface atoms have next neighbours of A and B, and surface atoms have less next neighbours than atoms from the interior of the cluster.

By supersonic expansion, one can produce homogeneous (pure) as well as heterogeneous (mixed) clusters. A two-dimensional schematic representation for a mixed cluster is given in figure 2.1. As *bulk* atoms of the inner part of a cluster are regarded, being completely surrounded by next neighbours of the same kind, whereas *surface* denotes the outer atoms of the cluster. Additionally to bulk and surface of a pure cluster, a mixed cluster exhibits *interface* components which are characterised by having next neighbours of both kinds of the cluster constituting atoms. There are two distinct paths one could follow for the production of mixed clusters: In the ‘coexpansion’ method, a gas mixture of the sample gases is prepared in an external reservoir and then expanded through the nozzle into the vacuum, similar to the generation of pure gas clusters. Experiments showed, that the species with the lower cohesive energy [15] tends to form the surface of the cluster in order to minimise the surface energy [16, 17]. The neon-krypton clusters, whose study is described in chapter 4.2, have been produced by coexpansion. Alternative to that, one can use the so-called ‘pick-up’ technique. This means

that a host cluster is generated via supersonic expansion. Then the clusters are exposed to a beam of the doping gas whose atoms will be adsorbed on the surface of the original aggregate, possibly in form of a surface layer or as small ‘guest clusters’ [17]. Furthermore, it is assumed that by the collisions with the doping gas a cooling effect of the cluster is established, meaning that ultracold neutral clusters can be produced via this method.

The size distribution of clusters generated by supersonic expansion is of the Boltzmann type and shows a very large width, proportional to the mean size  $\langle N \rangle$  itself. This mean size can not be calculated exactly, but there are empirically found scaling laws to estimate its value. Hagena [18] introduced a condensation scaling parameter  $\Gamma^*$  which is dependent on the cluster source conditions, namely the number density  $n_0$ , the nozzle diameter  $d$  in  $\mu\text{m}$  and the temperature  $T_0$  in K:

$$\Gamma^* = n_0 d^q T_0^{\frac{q}{4}-1.5}.$$

The parameter  $q$  has to be determined by experiments, e. g. by cluster beam measurements where  $d$  is varied at constant  $T_0$ , and in experiments on argon it was found as 0.85. Later, Buck and Krohne [19] performed scattering experiments with helium in order to find expressions to directly determine the mean size of the clusters. They advise to use different formulas for different ranges of cluster sizes, depending on the value of  $\Gamma^*$  which they define as

$$\Gamma^* = \frac{p_0 d_{eq}^{0.85} K_{ch}}{T_0^{2.2875}}.$$

Here,  $K_{ch}$  is a material dependent constant,  $p_0$  the expansion pressure in mbar and  $d_{eq}$  the equivalent nozzle diameter for conical nozzles of half opening angle  $\alpha$ , determined via  $\frac{0.74d}{\tan(\alpha)}$ . For large values of the scaling parameter,  $\Gamma^* > 1800$ , they use the original equation from Hagena,

$$\langle N \rangle = 33 \left( \frac{\Gamma^*}{1000} \right)^{2.35}. \quad (2.1.1)$$

For the intermediate size range ( $350 \leq \Gamma^* \leq 1800$ ) they slightly modified Hagena’s equation to

$$\langle N \rangle = 38.4 \left( \frac{\Gamma^*}{1000} \right)^{1.64}, \quad (2.1.2)$$

and for  $\Gamma^* < 350$  they recommend using a third order polynomial,

$$\langle N \rangle = \exp(2.23 + 7 \cdot 10^{-3} \Gamma^* + 8.3 \cdot 10^{-5} \Gamma^{*2} + 2.55 \cdot 10^{-7} \Gamma^{*3}). \quad (2.1.3)$$

In all cases, an increase in temperature as well as a decrease in expansion pressure will lead to a decrease of the cluster size.

The sizes of water clusters can be estimated by similar relations than the ones given above for rare gas clusters. For this purpose, Bobbert *et al.* modified the

scaling law from Hagena (see above) according to results they have obtained in mass spectroscopy experiments [20]. They found that the cluster mean size of a beam of water clusters can be calculated via

$$\langle N \rangle = D(d_{eq}^q \frac{p_0 T_0^{q-3}}{k T_0 (1000 (r_{ch}^{q-3} T_{ch}^\alpha)^{q-3})^a}). \quad (2.1.4)$$

Here,  $p_0$  is the stagnation pressure of the water vapour in Pa,  $T_0$  the temperature of the nozzle in K and  $k$  is Boltzmann's constant. In the experiment, the temperatures of reservoir and nozzle are measured by thermocouples. The stagnation pressure of the water vapour is then inferred from the temperature via a reference table [21]. The equivalent nozzle diameter can be determined via  $d_{eq} = \frac{0.933d}{\tan \alpha}$ , with  $d$  being the nozzle diameter in  $\mu\text{m}$ . For water, the characteristic length  $r_{ch}$  equals 3.19 Å, and the characteristic temperature  $T_{ch}$  is 5684 K. They determined the parameters  $q$ ,  $a$  and  $D$  by fitting their data as  $q = 0.634$ ,  $a = 1.886$  and  $D = 11.6$ .

## 2.2 photoionisation

### 2.2.1 single photoionisation

Let's follow the story from the introductory chapter but going into more detail this time. The smallest constituents of which a cluster can be formed are the atoms. According to Bohr's picture, the electrons of an atom are orbiting the nucleus on different discrete spheres. Depending on their distance to the nucleus these spheres, which we will call now electronic orbits, are named differently: The *core levels* (inner shells) are very close to the nucleus of the atom whereas the *valence levels* are the outer shells and are divided into *inner* and *outer* valence level. As the valence levels lie further away from the atomic core, the binding energies of the electrons occupying these levels are much lower than for the core level electrons. In order to set an electron in an atom free, one needs to provide energy to the system, sufficient for leveling the binding energy of the respective electron in the atom. A possible way of pumping energy into a system is to bring this system into a (preferably) monochromatised beam of photons. If the photon energy  $h\nu$  is larger than the binding energy of a specific bound electron, then this electron can be released from its orbit and be transferred into the continuum (emitted). The process of light absorption followed by electron emission is called *photoionisation*. As an illustrative example, ionisation of a core level electron by a single photon is depicted in figure 2.2. In the sketch, the energy is not to scale; the topmost line represents the vacuum level beyond which the continuum stretches, and the binding energy increases downwards. According to Koopmans [5], the

negative binding energy can be viewed as being equal to the ionisation potential of an electron, so that the photoionisation process can (similar to equation 2.0.1) be formulated as

$$E_{kin} = h\nu - IP. \quad (2.2.1)$$

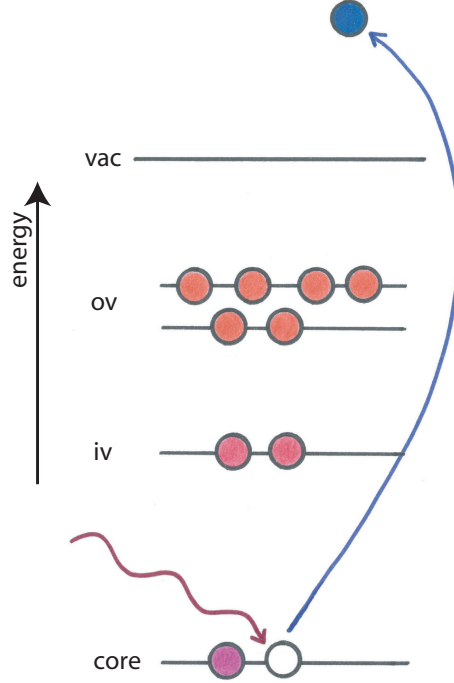


Figure 2.2: Schematic representation of single photon ionisation of a core level electron.

To simplify things, the non-relativistic dipole approximation will be used in the following. It states that

$$\mathbf{k} \cdot \mathbf{r} \sim 0 \quad \text{for} \quad h\nu \ll \frac{2}{\alpha Z_{eff}} IP \quad (2.2.2)$$

[22]. Here,  $\mathbf{k}$  is the wavenumber vector,  $\mathbf{r}$  the space coordinate of the ionised electron,  $\alpha$  the fine structure constant and  $IP = \frac{Z_{eff}^2}{2n^2}$  the ionisation energy of the bound active electron. With  $a_{nl} = \frac{n^2}{Z_{eff}}$ , the mean orbital radius of the bound active electron, equation 2.2.2 corresponds to  $2\pi a_{nl} \ll \lambda$ . This means that the wavelength of the incident electromagnetic wave is large compared to the size of the atomic orbit (or, in other words, that over this region the spatial variation of the field amplitude is small) which is valid for photon energies below 1 keV. As a consequence of the implementation of the dipole approximation, the operator

describing the time-dependent interaction between photon and atom simplifies to

$$H_{int} = \frac{\hbar e A_0}{2m} \mathbf{P} \sum_j \nabla_j,$$

with  $A_0$  representing the intensity and  $\mathbf{P}$  the polarisation of the vector potential describing the electromagnetic field. Furthermore, this allows also neglecting the recoil energy of the ion in equation 2.2.1 which is feasible as practically, due to the large mass ratio between the remaining ion and the photoelectron, the photoelectron carries away most of the excess energy of the ionisation process [22].

In general, the emission of photoelectrons is not isotropic but depends on the polarisation direction of the incident light. Since the emission of electrons is initiated by oscillations, which the electric field vector forces onto the atomic electrons, the emission process shows a directionality. Within the dipole approximation, the angular distribution of electrons emitted after photoionisation by linearly polarised light is described by the differential cross section

$$\frac{d\sigma}{d\Omega}(\Theta) = \frac{\sigma}{4\pi} \left[ 1 + \frac{\beta}{2} (3\cos^2\Theta - 1) \right]$$

[23, 24], a differentiation of the photoionisation cross section  $\sigma$  after the solid angle element  $d\Omega$  in the direction specified by the angle  $\Theta$  between the direction of electron emission and the electric field vector. The angular distribution or anisotropy parameter  $\beta$  describes the transfer of angular momentum from the photon to the photoelectrons. Since  $\sigma$  must be positive, the numerical value of  $\beta$  lies between 2 and  $-1$ . It determines the actual shape of the angular distribution pattern as indicated in figure 2.3. It can be seen that for the so-called ‘magic angle’  $\Theta_m = 54.7^\circ$  the influence of  $\beta$  vanishes. Therefore the differential cross section becomes directly related to the partial photoionisation cross section. The latter one is an expression for the strength of the photon-atom-interaction and can be accessed by collecting all emitted electrons of a specific ionisation process.

There are, however, single photoionisation processes which are not as straightforward as the direct photoionisation described above. It is possible, that one electron is excited to a higher lying bound orbital while another one is ionised. This process, which is due to electron-electron correlation, is called satellite photoionisation and is shown schematically in figure 2.4. Since a part of the photon energy is used for the excitation process, the emitted photoelectron, the so-called satellite electron, possesses less kinetic energy than the corresponding electron of the direct ionisation case (main electron). In a photoelectron spectrum, these satellite electrons are found under fixed energetic distances from the main line,

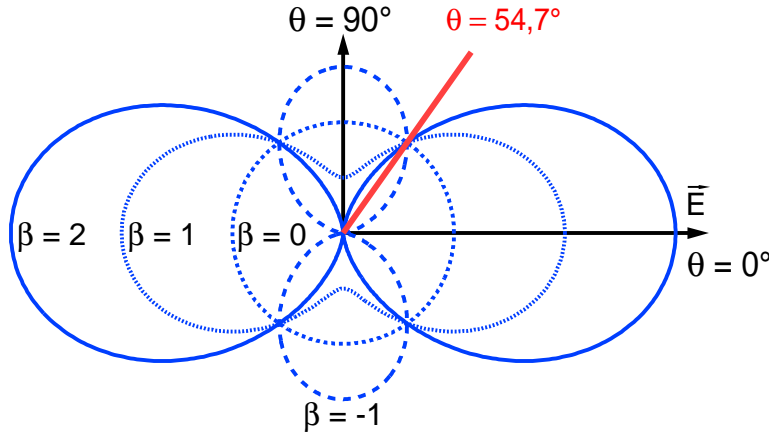


Figure 2.3: Angular distribution of photoelectrons for different values of the anisotropy parameter  $\beta$  in dependence of the polarisation direction of the light and the angle under which the electrons are emitted. The magic angle ( $\Theta = 54.7^\circ$ ) is marked by the red line. [25]

because the excited electron transits from a bound orbital to another, which corresponds to discrete energy differences. Satellites can appear in large quantities [26] and are closely connected to the orbital structure [27].

If the investigated system is not a single atom but a cluster of atoms, then even the simplest photoelectron spectrum, where one focuses on a specific photoline, will show multiple peaks. But how is it possible, that for one transition a whole range of photoelectron kinetic energies is covered? To understand this effect, one should bear in mind that a cluster is an assembly of atoms which can occupy different sites within the cluster (see figure 2.1). Depending on which atom will be photoionised, i. e. from which atom the photoelectron will be emitted, the photoelectron kinetic energy may vary. This is due to an effect called polarisation screening [28] which is shown schematically in figure 2.5 for (a) bulk and (b) surface ionisation. During the emission of an electron, the electron distributions in the surrounding atoms rearrange so that a negative charge is brought close to the ionised atom and a positive one away from it, which corresponds to a polarisation of the next neighbours. Because of the overlap of the wave functions of the ejected electron and the electrons of the cluster ion, the emitted electron is influenced by the induced screening, which results in an increase of its kinetic energy. In case an electron from a surface atom is ionised (see figure 2.5 (b)), the atom cannot be completely enclosed by screening charges, wherefore the increase in photoelectron kinetic energy is lower than for the case of bulk ionisation (figure 2.5 (a)). In a photoelectron spectrum of a cluster, the polarisation screening leads to the development of additional peaks for each atomic photoline: always a surface peak adds and, if the cluster is large enough, then an additional bulk peak

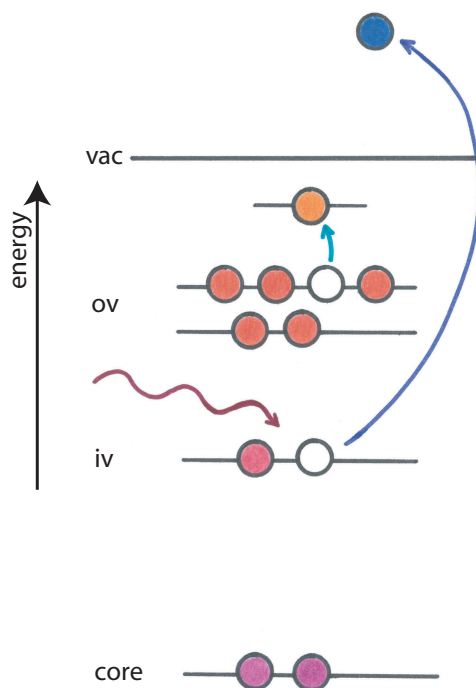


Figure 2.4: Schematic representation of satellite photoionisation. The photoelectron (blue) has less kinetic energy than the corresponding main line photoelectron since a part of the photon energy is used to excite another electron (orange) to a higher lying bound orbital.

is formed. For mixed clusters, electrons emerging from atoms forming the interface between the different atomic species accumulate in interface peaks. These lie energetically lower than the surface peak, due to the screening effect being stronger in the latter case. An example of a photoelectron spectrum of argon clusters, recorded at a photon energy of 90.1 eV, is given in figure 2.6. The complete energy distribution of the Ar 3s photoelectron is shown, together with a fit that deconvolutes the spectrum into its different contributions. The sharp peak on the right (red) is the atomic photoline, which is caused by photoionisation of Ar monomers that are still present in the cluster beam. Going to higher kinetic energies, the green peak receives intensity from the surface electrons whereas the bulk peak is depicted by the blue curve. The energetic distance between monomer peak and surface or bulk peak increases for larger clusters and can be used as an alternative measure for the cluster size.

## 2.2.2 photo double ionisation

In the photo double ionisation process, two photoelectrons are emitted after the absorption of a single photon of sufficient energy. For this purpose, the photon



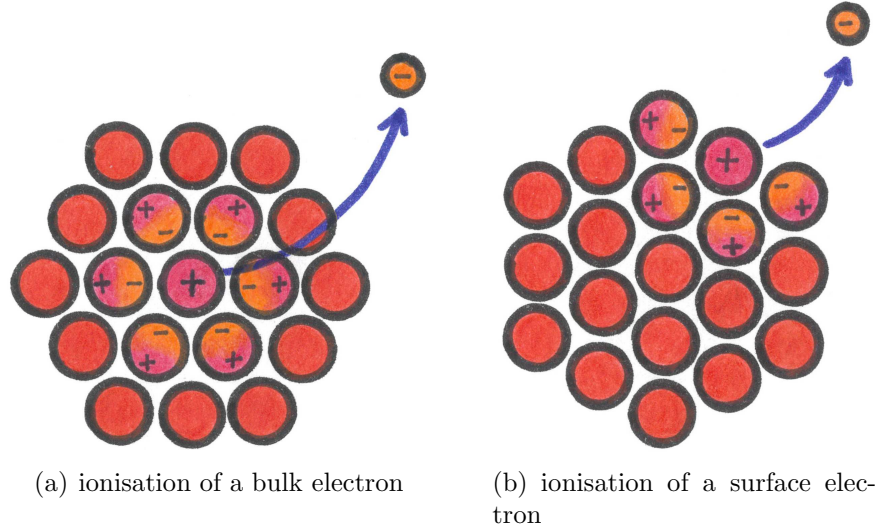


Figure 2.5: Polarisation screening in cluster photoionisation. Next neighbours of the electron emitting atom redistribute their charges in order to shield the site of ionisation. This leads to an increase of the electron's kinetic energy, for bulk emitted electrons more than for electrons emerging from surface atoms.

energy needs to exceed the double ionisation potential  $DIP$  of the atom which is higher than twice the single ionisation potential because of electrostatic forces (Coulomb forces) in the final state. Analogous to 2.2.1 the energy balance in the photo double ionisation process can be written as

$$E_{kin1} + E_{kin2} = h\nu - DIP. \quad (2.2.3)$$

To have an estimate, one could use the simple empirical rule that the lowest  $DIP$  equals 2.8 times the first ionisation energy ( $IP$ ) [30]; for clusters the  $DIP$  will be even lower. As an example for this process, the photo double ionisation of core level electrons is shown in figure 2.7.

There are different possibilities of removing two electrons from an atom with only one photon. So-called direct pathways, which could be processes such as ‘shake-off’ or ‘knock-out’, lead to a continuous sharing of the excess energy between the two photoelectrons. This results in a broad continuous energy distribution covering the kinetic energy range between zero and the whole available excess energy [22]. After a single ionisation took place, the eigenstates of the ionised system change. This might happen so fast that an electron which was previously correlated with the ionised electron cannot react immediately to the new state. Instead it might be liberated from the binding core potential for a short time and thus could be transferred to a continuum state with a certain probability as well, which means it is ‘shaken off’ [31]. One speaks of ‘knocking out’ an

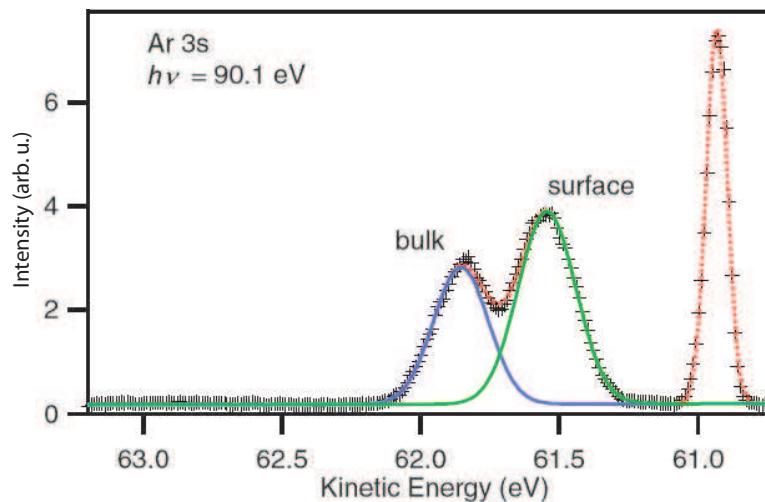


Figure 2.6: Example for a photoelectron spectrum of clusters. The different contributions to the Ar 3s spectrum from surface (green) and bulk (blue) photoelectrons are well resolved; the atomic line to the right stems from monomers still present in the beam. [29]

electron instead if the photon absorbing electron, which hence was transferred to an excited or ionised state, interacts via the Coulomb force with a second electron and hits it off the core potential. The two electrons are then correlated in the final state. It should be noted that, in the direct double ionisation, the double electron emission is formally a forbidden process within the (frozen) orbital model, but is generally considered to be mainly allowed because of electron correlation [32].

If the final state is accessed via a resonant intermediate state (of finite lifetime), then one speaks of sequential photo double ionisation. Here, the relaxation of the system after initial ionisation releases energy which then leads to the emission of a second electron. Since the energy of the intermediate state is restricted to certain values, the kinetic energy of the second electron is restricted as well. Therefore, the energy distribution among the two emitted electrons is not continuous. In this sense, some of the autoionisation processes that will be described in chapter 2.3 can be viewed as sequential photo double ionisation. If the energy difference between the two electrons is large, then effects due to the indistinguishability of electrons can be excluded [22]. Both, sequential photo double ionisation and direct photo double ionisation, lead to the same final states and thus are experimentally indistinguishable.

In clusters, it is possible that after single photoionisation the ejected electron inelastically collides with a second electron and transfers some of its kinetic energy to it. If the energy is sufficient, the second electron might be ionised as well. The result of this sequential process is a doubly charged final state with two continuum

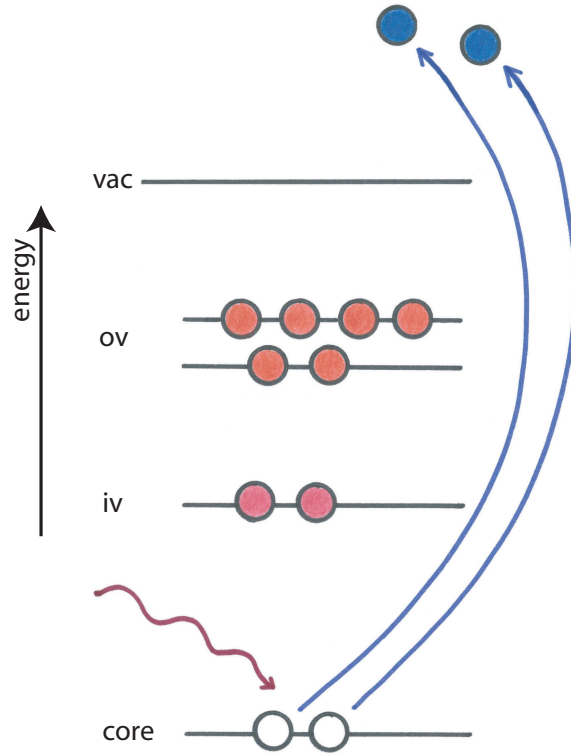


Figure 2.7: Schematic representation of photo double ionisation by a single photon, in this case of two core level electrons.

electrons. Due to the weak binding forces in the cluster, there is no correlation in the initial or final states, which in turn allows for an arbitrary energy distribution among the electrons under the condition that the sum of the kinetic energies is constant [33, 34].

In the past decades, the investigation of double and multi ionisation processes has gained lots of momentum. These kind of experiments were stimulated by the availability of very high photon intensities (above  $10^{14}$  W/cm<sup>2</sup>), e. g. from lasers. Although the energy provided by a single photon might not be sufficient, ionisation via nonlinear effects, i. e. simultaneous absorption of multiple photons, can take place [35]. While the ionisation initiated by infrared or visible radiation from conventional lasers develops via tunneling processes, direct multiionisation processes initiated by multiphoton absorption can nowadays be studied with the newly available free electron lasers [36, 37]. The main aim of these investigations is a better understanding of photoionisation and of electron-electron correlation.

## 2.3 autoionisation

This chapter will focus on the discussion of an important group of non-radiative decay channels, the autoionisation processes called Auger decay, interatomic / intermolecular Coulombic decay (ICD) and electron transfer mediated decay (ETMD).

If an atom or molecule autoionises, it spontaneously emits an electron and thus transits to a higher charge state. As the investigated species are all stable in their electronic ground state, the autoionisation process occurs only after initial ionisation or excitation. The size of the system and its electronic configuration determine which autoionisation processes are allowed or, if more than one, favoured.

### 2.3.1 Auger decay

The most commonly known autoionisation process to follow photoionisation is Auger decay. It is named after Pierre Auger who was the first scientist to observe and explain the effect [38]. The process competes with the emission of x-ray radiation, but especially for light atoms (up to atomic number  $Z = 30$ ) Auger decay will be the dominating process [38].

The Auger decay is initiated by ionisation of a core level electron as illustrated schematically in figure 2.8 (left hand side). This leads to the formation of an ion whose energy is well above the double ionisation threshold [39]. The remaining electrons of the atom will then rearrange in order to find a state of minimum energy. This will lead to an electron from a higher orbital filling the core hole vacancy (see figure 2.8 right hand side). The energy released by this relaxation can, in a simple picture, be regarded as an emitted x-ray quant. If a valence electron of the same atom then absorbs this energy, it can be ionised and be emitted as the so-called Auger electron, leaving behind an atomic dication. But because the filling of the vacancy and the simultaneous emission of the Auger electron only occur due to the Coulombic force, the process is nevertheless considered as non-radiative. Furthermore, Auger decay is a local autoionisation process since the whole process can take place in an isolated atom.

Often the Auger decay can be considered as a two-step process, photoionisation followed by autoionisation. Then the energy of the photoelectron created in the first step is directly proportional to the photon energy:

$$E_{\text{kin, photoel.}} = h\nu - IP.$$

The Auger electron instead results from a secondary process, thus its kinetic energy is independent of the photon energy. Its energy is, instead, element-specific as it can be determined by the potential difference between the core and

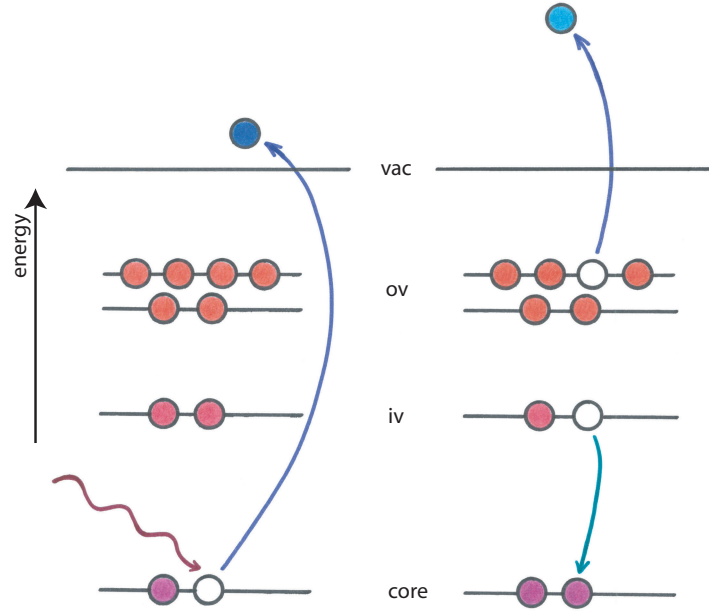


Figure 2.8: Schematic representation of the Auger process. After photoionisation of a core-level electron (left, blue), the vacancy can be filled by relaxation of a valence electron. The released energy is sufficient to ionise another valence electron, the so-called Auger electron (right, light blue).

valence levels:

$$E_{\text{kin, Auger el.}} = IP_{\text{core level}} - IP_{\text{valence level}_1} - IP_{\text{valence level}_2}$$

or, equivalently, as the energy difference of the ion states before and after the Auger decay [22]:

$$E_{\text{kin, Auger el.}} = E_{\text{initial}}(\text{one hole state}) - E_{\text{final}}(\text{two hole state}).$$

With the Auger kinetic energies being characteristic for each atom, Auger spectra represent a fingerprint of the atom [40]. This, together with the fact that a specific transition can easily be selected for analysis by focussing on the corresponding range of kinetic energies, has made Auger spectroscopy a versatile tool in materials research and surface analysis.

Similar to satellite photoelectrons, a part of the kinetic energy of an Auger electron can be used to excite another electron to a higher lying orbital, thus making the Auger electron an Auger satellite electron.

As mentioned above, the kinetic energy of an Auger electron is independent of the photon energy. There is an exemption to this, namely the effect of post collision interaction (PCI): If the photon energy is very low, so that the photoelectron

is slow, then the photoelectron and the Auger electron will influence each other in a retroactive way (via collision). As the second step of the Auger decay, the fast Auger electron leaves a singly positively charged atom. The potential of the atomic ion can be described as a screened Coulomb potential, where the strength of the screening is approximately given by the distance of the photoelectron to the ion. Since the Auger electron is much faster than the slow photoelectron it will eventually ‘overtake’ it. The Auger electron starts out seeing a doubly charged system, and after overtaking the photoelectron it sees a singly charged system due to screening. This causes an increase of the Auger kinetic energy and a broadening of the Auger line [41]. At the same time, the charge that the slow photoelectron sees left behind is singly positive at the beginning and changes to doubly positive as soon as the Auger electron has passed the photoelectron. This in turn causes a lowering in the photoelectron’s kinetic energy due to the increased attraction by the doubly charged ion and leads to the appearance of a tail on the low kinetic energy side in the photoelectron spectrum. The effect of post collision interaction has been studied extensively, especially on the rare gases and their clusters [41–48].

### 2.3.2 intermolecular Coulombic decay

Let us extend the system under investigation from a simple atom to an atomic cluster. Now, a new relaxation channel additional to Auger decay after core level ionisation opens: interatomic (or intermolecular) Coulombic decay (ICD). This autoionisation process is possible even when the photon energy is lowered below the ionisation potential of a core level electron or even below the double ionisation potential of the monomer. It has been predicted by theoreticians more than a decade ago [49] but only several years later the first experiments, performed on neon clusters, were successful in recording data that showed clear evidence for its actual existence [50]. By now, there are a number of experiments that have investigated ICD, in various systems and with different spectroscopic set-ups; a comprehensive overview can be found in [51].

A schematic illustration of the ICD process is given in figure 2.9. As a first step, an inner valence electron of one of the atoms forming the cluster is photoionised, leaving the cluster in an excited state (left hand side of figure 2.9). This vacancy can be filled by relaxation of an outer valence electron from the same atom which leads to the release of energy. This energy is not sufficient to ionise another electron at the same site because it is lower than the required second ionisation energy. This means that no Auger-like process leading to the creation of an isolated atomic dication is possible. But now the fact that an atom *in a cluster* was ionised comes into effect: In a cluster, a doubly charged final state can be created by placing the two positive charges on two different atoms within the same

cluster. In this way, the repulsive Coulomb potential between the two positive charges is reduced, and would even approach zero eV in the solid state limit [52]. This causes a significant drop of the double ionisation threshold compared to the isolated monomer [53]. Therefore, the released energy will be transferred via Coulomb forces to a neighbouring atom within the cluster where it is sufficient to ionise an outer valence electron, the so-called ICD electron (see right hand side of figure 2.9). Left behind is a doubly charged cluster with the charges located at two different atoms. Due to the fact that more than one atom participates in the process, ICD is called a non-local autoionisation process.

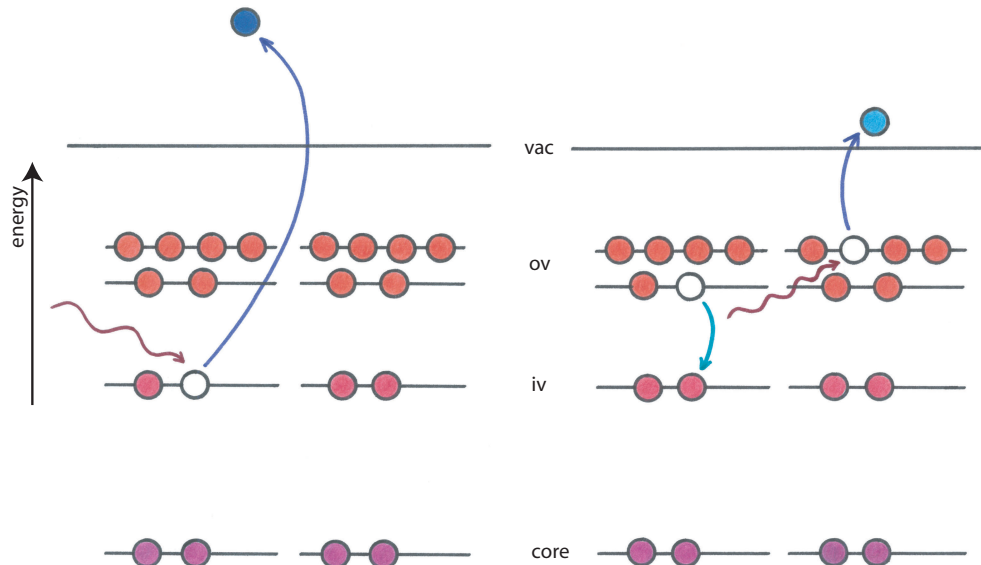


Figure 2.9: Schematic representation of the ICD process. The vacancy created by photoionisation of an inner valence electron (left, blue) can be filled by relaxation of an outer valence electron. The released energy can be sufficient to ionise an outer valence electron of a neighbouring monomer, the so-called ICD electron (right, light blue). The two positive charges created in the process can lead to Coulomb explosion of the cluster.

Similar to the case of Auger decay, the energy of an ICD electron does not depend on the photon energy used for initial ionisation but is only dependent on the energy gap between the inner and outer valence levels of the participating atoms. This means that ICD electrons are element specific which offers the possible application of employing ICD spectroscopy in materials research. An accurate calculation of the ICD energy is difficult and has been topic of a number of theoretical works (e. g. [54–56]). Nevertheless, it can be estimated in a simple way by subtracting from the energy gap between the inner and outer valence levels the binding energy of the outer valence electron to be emitted as well as

the Coulomb repulsion energy between the two charges:

$$E_{\text{kin, ICD el.}} = IP_{\text{inner valence}} - 2 \cdot IP_{\text{outer valence}} - E_{\text{Coulomb}}. \quad (2.3.1)$$

The latter one can be approximated by

$$E_{\text{Coulomb}} = \frac{1}{4\pi\epsilon_0} \cdot \frac{e^2}{r}, \quad (2.3.2)$$

where  $\epsilon_0$  is the permittivity of the vacuum,  $e$  the unit charge and  $r$  the internuclear distance. For the neon dimer example, schematically depicted in figure 2.9, the binding energies of the inner and outer valence levels are 48.475 eV (Ne  $2s$  [57, 58]) and 21.59 eV (Ne  $2p$ , statistical mean value of 21.56 and 21.66 [57]). With an equilibrium internuclear distance of  $r = 3.1$  Å [59] the Coulomb repulsion amounts to 4.64 eV. Using equation 2.3.1, a kinetic energy of approximately 0.66 eV of the ICD electron can be determined. This value is in accordance with theoretical calculations [56]. Due to Coulomb repulsion the dimer will explode after IC Decay, leaving two singly positively charged fragments behind. Larger clusters may not necessarily explode, but if so, then additional to the two charged fragments probably a number of neutral fragments will be created in the dissociation process.

The energy transfer in the ICD process can be viewed as an exchange of a virtual photon [39, 60] wherefore its probability to occur is proportional to  $r^{-6}$  for the limiting case of infinitely distant monomers [61]. It can take place even without a significant overlap of the electronic orbitals but it will be much faster if there is some overlap which makes the transition dipole allowed [61]. In general, ICD is assumed to take place on a fs timescale [53, 62], implying it is orders of magnitude faster than the competing radiative decay (as fluorescence) which happens on the ns timescale. Therefore, whenever energy conservation allows ICD to take place, the process is expected to be the dominant relaxation channel of inner valence holes [53] since the final state with distributed charges is energetically more favourable than the dicationic one resulting from Auger decay.

There have been numerous investigations on ICD in homogeneous and heterogeneous rare gas clusters (see e. g. [62–66]). According to theory, the orbital overlap plays a crucial factor even in these loosely bound van der Waals clusters [61], making ICD a process that is highly sensitive to the cluster size. If the cluster is large, then the overlap decreases due to a reduced interaction between the holes and the outer valence electrons. This results in a weaker coupling and thus the probability for ICD is lowered. At the same time, ICD becomes faster for larger cluster sizes [67]. This is due to the fact that for a larger cluster the energy criterion is easier to fulfill since the two charges may be spread more widely corresponding to a larger decrease of the Coulomb repulsion. From these two competing contributions follows that there is a saturation effect of the ICD efficiency when the cluster size is increased [52].



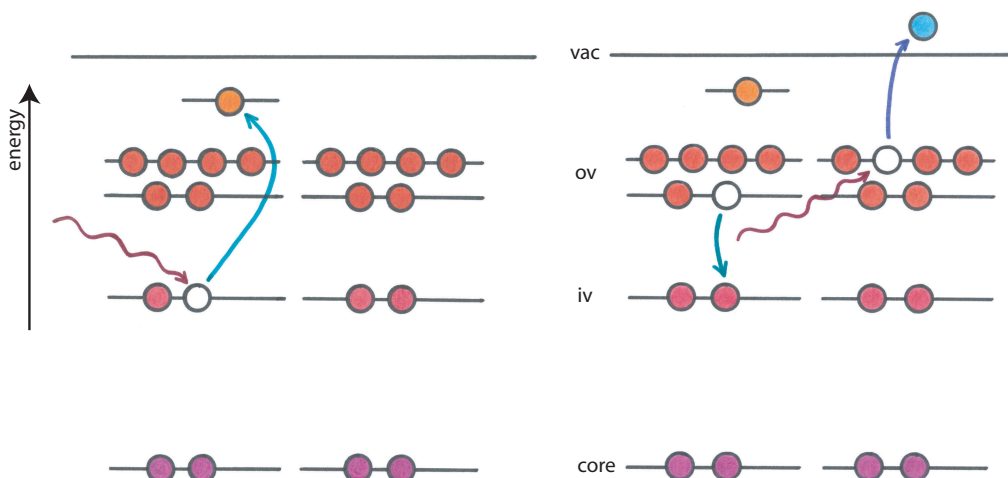


Figure 2.10: In the case of resonant ICD, the incoming photon does not ionise but excite an inner valence electron to a higher lying bound orbital (left, orange). Subsequent relaxation of an outer valence electron releases energy which is sufficient to ionise an outer valence electron of a neighbouring monomer (right, light blue). Since the originally excited electron only ‘watches’ the autoionisation, this process is called *spectator resonant ICD*.

Analogous to resonant Auger [68, 69] there exists *resonant ICD* [70], which has first been discovered in large neon clusters [71] and neon dimers [72]. It is shown schematically in figures 2.10 (case a) and 2.11 (case b). In contrast to ‘normal’ ICD the process is not initiated by ionisation of an inner valence electron, but instead by the resonant excitation of an electron to a higher lying unoccupied bound orbital (see left hand side of figure 2.10). There are two possible scenarios that can take place: The first (a) continues as normal. The inner valence vacancy is filled by an outer valence electron from the same atom, the nascent energy is transferred to a neighbouring atom and ionises an outer valence electron there (see right hand side of figure 2.10). The result is a cluster which is energetically excited and carries a single positive charge at another site than that of the initial ionisation. In case (b) the originally excited electron itself fills the vacancy. Then the released energy is transferred to the neighbouring atom and causes the emission of the ICD electron (see right hand side of figure 2.11). In this case, the resulting cluster is singly positively charged as well, but not excited. Furthermore, the ICD electron is of higher kinetic energy than in case (a) or in ‘normal’ ICD as described above. Since in case (b) the excited electron takes part in the relaxation process, it is termed *participator ICD* whereas case (a) is called *spectator ICD*. It should be noted that resonant ICD is initiated by an excitation process, implying that a photon energy below the ionisation potential is already

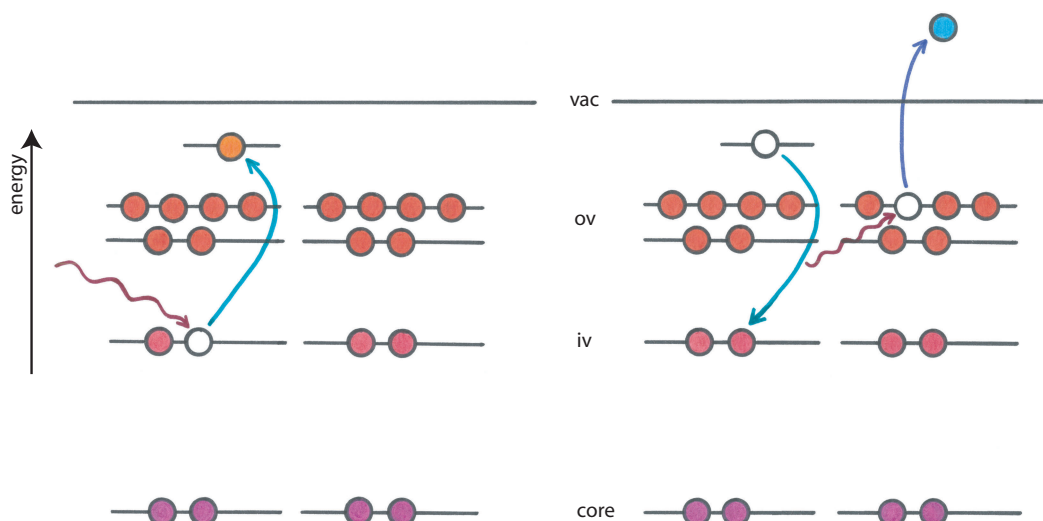


Figure 2.11: If instead the originally excited electron (orange) relaxes and thus initiates the autoionisation, then the process is called participator resonant ICD. In this case, the released energy is slightly larger, leading to a higher kinetic energy of the emitted electron (light blue) that is emitted from a neighbouring monomer.

sufficient. Furthermore, resonant ICD does not lead to a Coulomb explosion of the cluster due to the absence of the second positive charge. Nevertheless, usually the structure of the cluster will change because of the presence of the cation, which may result in a fragmentation of the weakly bound cluster.

Only a short time after the discovery of resonant ICD, another ICD-related relaxation pathway emerged: It was found that if an Auger decay resulted in an excited state it could be followed by an IC Decay, thus leading to a triply charged cationic cluster. The theoretical prediction [73, 74] could soon be confirmed by first experiments on argon dimers [75]. Later, the occurrence of this combined relaxation in argon trimers [76] as well as in mixed clusters was reported [77]. It was even found that ICD can take place after atomic non-sequential and sequential double Auger decay, resulting in  $A^{3+}-B^+$  ion pair formation [78–81]. Also, the inner valence hole necessary for ICD to take place can be created in a collision process. Only recently, ICD initiated by collision with an ion has been observed for the first time [82].

### 2.3.3 electron transfer mediated decay

Besides from ICD, another autoionisation process can take place in heterogeneous systems: the so-called Electron Transfer Mediated Decay (ETMD). It is constituted by the differing character of the monomers and represents a com-

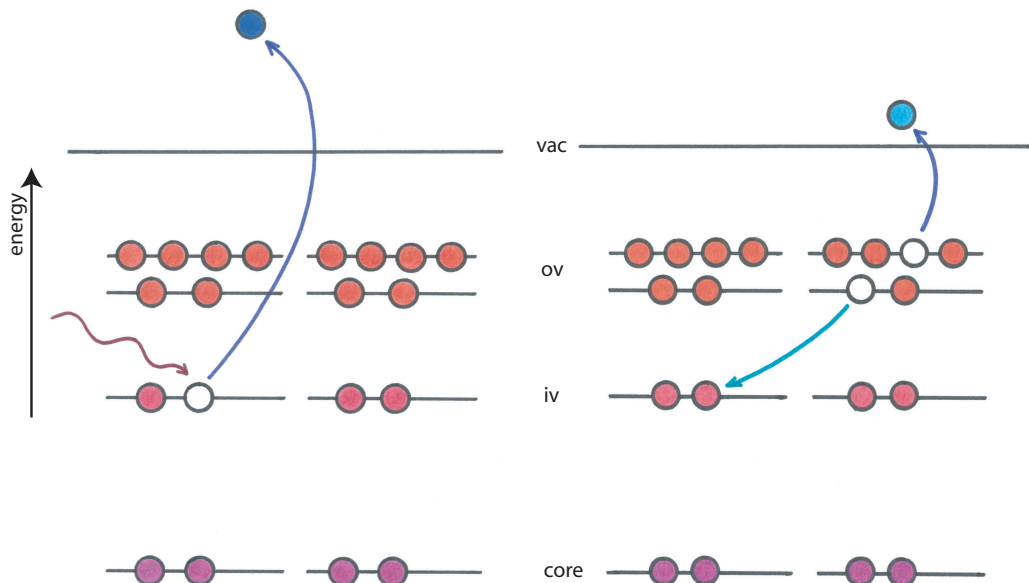


Figure 2.12: Schematic representation of the ETMD(2) process. The inner valence vacancy created by photoionisation (left) is filled by an electron transferred from another monomer of the cluster (red), where the released energy is sufficient to ionise another outer valence electron (right, light blue). In contrast to ICD, both positive charges of the final state are located at the same monomer, therefore no Coulomb explosion occurs.

peting process to ICD [52]. Depending on the number of atoms involved in the relaxation process, one distinguishes between ETMD(2) for two atoms, which is shown schematically in figure 2.12, and ETMD(3), shown in figure 2.13, when three atoms participate in the decay. Similar to ICD, ETMD is generally initiated by inner valence ionisation of one of the cluster constituting atoms (see left hand side of figure 2.12). But, instead of the intra-atomic electronic relaxation (like in ICD), an electron from a neighbouring atom is transferred to fill the inner valence vacancy (see right hand side of figure 2.12) which means that the initially ionised monomer is neutral again. In the case of ETMD(2), the energy released by the electron transfer is then used to ionise an outer valence electron of the electron donating monomer. This results in a cluster where both positive charges are located on the same monomer, much like a dication embedded in a neutral environment. By contrast, in the case of ETMD(3), the energy released by the electron transfer is transferred to a third involved monomer where it ionises an outer valence electron. This means that the two positive charges are located at two different monomers, much as in ICD, which can lead to a Coulomb explosion of the cluster.

Similar to ICD, ETMD has been theoretically predicted to take place if two

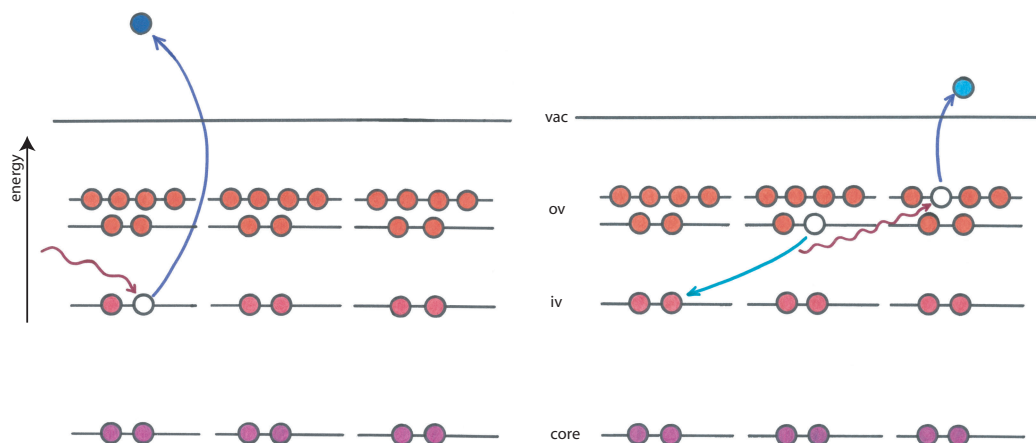


Figure 2.13: In the case of ETMD(3) three monomers participate in the autoionisation process. The inner valence vacancy is filled by an electron (red) transferred from a neighbouring monomer, with the released energy being transferred to a third monomer where it ionises an outer valence electron (right, light blue). The process results in the two charges distributed over different monomers of the cluster, similar to the ICD process.

criteria are fulfilled: the energy criterion and the coupling criterion [52]. The energy criterion states that ETMD can occur as soon as the double ionisation potential (which equals twice the single ionisation potential plus the Coulomb repulsion) of a (neighbouring) monomer is lower in energy than the ionisation potential of the initially created inner valence vacancy. The coupling criterion is even stricter than for ICD. A significant interaction of the electron distributions of these monomers can only be expected at very short internuclear distances between the participating monomers. This relies on the rate for ETMD falling exponentially with increasing intermolecular distance [83]. This implies that, due to the fact that ETMD involves the transfer of a particle, i. e. an electron, its probability is much lower than for a process relying purely on energy transfer as ICD (theoretical estimations speak of at least one order of magnitude for neon-argon dimers [52, 83]), and ETMD(3) being even less efficient than ETMD(2). Thus, ETMD is only observable with a measurable intensity when ICD is not possible or when the internuclear distances are so short that ETMD could be favoured. The existence of ETMD could be proven only recently, where Förstel *et al.* succeeded to show ETMD(3) to take place in mixed argon-krypton clusters [84].



# Chapter 3

## experimental

As discussed in the previous chapter, when non-local decay processes such as ICD and ETMD take place in a cluster, various charged and neutral particles are created. In the case of ‘normal’ ICD these are two electrons, the photon energy dependent photoelectron and the ICD electron of fixed kinetic energy, as well as the fragments resulting from the Coulomb explosion of the cluster ion. These are two singly positively charged and possibly some neutral fragments. In the case of ‘resonant’ ICD, there are only the ICD electron, of slightly higher kinetic energy than in the ‘normal’ case, and a singly positively charged and possibly excited cluster which might undergo fragmentation. These signatures are well suited for studying ICD and ETMD in experiments based on time-of-flight spectroscopy. In a classical electron time-of-flight experiment electrons over the whole kinetic energy range are recorded simultaneously. With the help of calibration measurements or simulations, the flight times can be transformed into kinetic energies. Due to different characteristics of ICD electron and photoelectron kinetic energies, it is possible to distinguish between them.

The first experimental evidence for ICD in large neon clusters was found by Marburger *et al.* [50], and later on many more investigations on ICD in different pure and mixed rare gas clusters followed (e. g. [62, 64, 65]). All these experiments have used hemispherical electron energy analysers which allow for recording of high resolution energy spectra. But in order to be able to assign spectral features to their origin, series of varying photon energies have to be recorded. Furthermore, due to scattering, photoemission from clusters generally leads to a broad, unstructured background in the spectra, in particular in the low kinetic energy range. Additionally, a broad continuous energy distribution generated from direct photo double ionisation (if energetically possible) may be superimposed. Since the ICD electrons will usually be found in this energy range, a careful estimation of the background contribution has to be done. Even though, it could turn out to be impossible to clearly separate them.

Some of the above mentioned disadvantages can be overcome by using a coincidence technique. This allows to group the recorded electrons into processes involving a fixed number of electrons, i. e. two in the case of ICD or ETMD. By analysing the correlation between the two electrons of each pair and between all the pairs recorded during a measurement, it is possible to conclude on the process by which they were generated, as will be described in chapter 3.3.2. Since the ionising photon energy is generally known, a specific photoprocess, such as ICD after inner valence ionisation, can be identified and selected via the kinetic energy of the photoelectron. It is important to perform comparative measurements on the isolated monomers from which the clusters are formed: Since ICD and ETMD are non-local autoionisation processes, they do not take place in isolated systems. Therefore no feature should be observed in this case at the energy corresponding to inner valence ionisation, which serves as a validating criterion. By using the coincidence method, it was possible for the first time to undoubtedly prove the occurrence of ICD in water clusters [85], as will be discussed in detail in chapter 5. Due to its success, the coincidence technique was employed for further studies on water and rare gas clusters as will be shown in the following chapters of this thesis. For all experiments presented here, electron spectrometers of the so-called magnetic bottle type were employed. These will be described in detail in chapter 3.2, embedded in a description of the whole experimental set-up.

A prerequisite for performing such investigations is the availability of an ionisation source, e. g. an electron source or a photon source. For the experiments presented here, ionisation by photon interaction was chosen. On the one hand, photon energies above the inner valence ionisation potentials of the species to be investigated are needed. On the other hand, the light source has to be pulsed to enable time-of-flight measurements. Furthermore, it is vital to be able to change the photon energy. These requirements point to the use of a synchrotron facility, which is, at the moment, the ideal source for intense and monochromatic radiation in the VUV and X-ray range. Chapter 3.1 gives a brief insight into the history and the working principle of these remarkable light sources.

## 3.1 light source

Synchrotron radiation made a career par excellence: It developed from a parasitic effect in particle accelerators to a powerful light source used by a large community of researchers in basic and applied sciences such as physical chemistry and materials science.

Based on the fact that accelerated charges emit electromagnetic radiation, synchrotron radiation is generated in spherical particle accelerators, where it has first been discovered in 1945 [86]. Since its emission led to an energy loss of

the accelerated particles, it was regarded as an unwanted side effect. However, researchers realised soon that it represented a valuable research tool: a powerful x-ray light source with unprecedented properties. This led to the so-called first generation synchrotrons, circular particle accelerators which were fitted ex post with ports to allow the synchrotron radiation to be used in external experiments. Later, electron storage rings solely designed for the generation of synchrotron radiation and its experimental application were built, consisting essentially of bending magnets which deflect the electron beam and thus produce the radiation. To further increase the intensity of the radiation and improve the brilliance (intensity per solid angle element, source size and energy interval) special magnetic devices were inserted into the straight parts of the storage rings. This is characteristic for synchrotrons of the third generation to which most of the ones in operation nowadays belong.

All experiments presented in this thesis were performed at BESSY II in Berlin, Germany, which is one of the third generation sources. In this facility (see overview given in figure 3.1), electrons are generated in a thermionic cathode and are accelerated to 70 keV (electron current of 300 mA). Then, in a high frequency linear accelerator of a microtron, they are boosted to 50 MeV (6 mA) before entering a small acceleration ring of 96 m circumference. Here, they are accelerated to 1.7 GeV, which corresponds to 99.999995% of the speed of light, or 299792.44 km/s (4.5 mA). Via a special magnet the electrons are then ‘injected’ into the storage ring which has a circumference of 240 m. In the ring they circulate for up to 10 hours, thus their current accumulates to approximately 100 mA. To keep the electrons on a circular path, their trajectories are bend in 32 dipole magnets, which are backed up by a number of quadrupole and sextupole magnets that serve for transversal and chromatic focussing as well as dispersion correction. Between the bending magnets, there are 16 straight segments which contain different insertion devices such as so-called wigglers and undulators. In the simplest case, insertion devices consist of  $2N$  pairs of dipole magnets which are arranged in alternating polarisation. The created periodic magnetic field thus causes the electrons passing through to be deflected periodically and move along sinusoidal trajectories which corresponds to a periodic acceleration. The radiation emitted by one electron at different periods of an undulator can interfere constructively, resulting in quasi monochromatic radiation. The wavelength of this radiation is determined by the period length of the undulator,  $\lambda_U$ . Due to the relativistic Lorentz contraction it is reduced by a factor of  $\gamma = \frac{E}{m_0 c^2}$ . When performing the transformation from the rest frame of the electron to the laboratory frame, the Doppler shift causes a further reduction by a factor of  $\gamma$ , resulting in a blue-shift of the radiation. The wavelength of the  $i^{th}$  order emitted from an undulator can thus be described in the laboratory frame by

$$\lambda_\gamma = \frac{\lambda_U (1 + \frac{(0.934 B \lambda_U)^2}{2})}{2i\gamma^2},$$



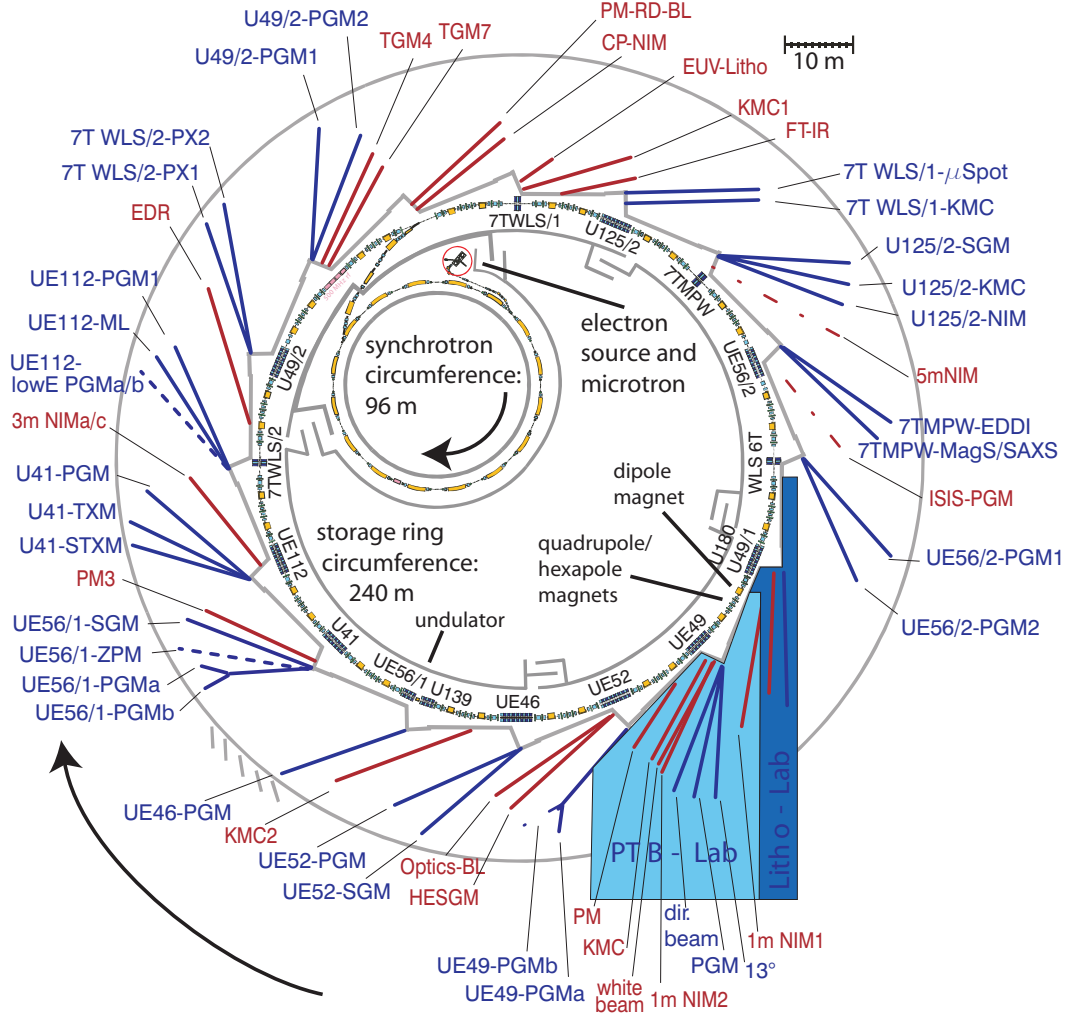


Figure 3.1: Overview of the synchrotron radiation source BESSY II. [87]

with  $B$  in T and  $\lambda_U$  in cm, and can obviously be shifted by changing the magnetic field [88]. Another effect of the Lorentz force on the relativistic electrons is that the pattern under which radiation is emitted by the electrons changes from a  $\sin^2$  function when being at rest to a narrow cone of  $\frac{2}{\gamma\sqrt{N}}$  opening angle, focussed in the forward direction. This implies that the spectral resolution is proportional to the number of undulator periods  $N$ , whereas the intensity scales with  $N^2$ . In a wiggler, the increased magnetic field strength leads to a distortion of the pure sinusoidal transverse motion of the electrons due to relativistic effects. This in turn leads to the generation of higher harmonics, causing the line spectrum to evolve into a continuous spectrum ranging from IR to hard x-rays. The radiation generated in wigglers is well collimated, the emission cone of  $\frac{2(0.934B\lambda_U)}{\gamma}$  being only in the mrad-range. The intensity, which scales with  $N$ , varies only little

with respect to energy and drops off exponentially at a critical photon energy  $\varepsilon_{crit} = B\gamma^2$  which can be adapted to the needs by adjusting the magnetic field strength. The spectrum of the radiation emitted from a bending magnet due to the transverse acceleration is similar to that from a wiggler. But since bending magnets are used in the first instance for defining the circular path of the electrons, one cannot change the magnetic field strength freely which means that the critical energy is fixed. The polarisation vector of synchrotron radiation lies within the plane of acceleration, which in general is horizontal, but new undulators of the apple-type [89, 90] now allow to move the magnet rows with respect to each other, making it possible to choose the polarisation direction freely, even circularly polarised.

To compensate for the permanent energy loss that is caused by the circulation, the electrons are additionally accelerated in four cavities in the storage ring. Passing this high frequency electric field of 500 MHz causes the electrons to be squeezed into bunches since the slower ones are more sped up than the faster ones. This implies that the synchrotron radiation is generated by bunches of electrons. It is emitted in form of approximately 30 ps long pulses wherefore BESSY belongs to the group of pulsed light sources. BESSY offers three different operation modes: single bunch, multi bunch and low alpha. In single bunch mode only one electron bunch circulates in the storage ring, representing a current of 10-20 mA. The electron bunch has a width of 50-200 ps and needs 800 ns for one revolution, which corresponds to a repetition rate of 1.25 MHz. This operation mode has been chosen for the experiments presented in this thesis since it allows to use the full 800 ns window for a time-of-flight measurement. Most of the time, BESSY operates in multi bunch mode which has been optimised for brilliance, photon flux and minimal loss of electron current over time. Electron bunches succeed every 2 ns, which would ideally make 400 bunches circulating in the ring but due to technical reasons there are only 320 plus one large gap which is filled by the so-called hybrid bunch. In this mode, typically a current of 200-300 mA is constituted by the  $10^{11-12}$  electrons that are circulating. The low alpha mode is of the same timing structure as the multi bunch mode, but exhibiting only about a tenth of the intensity in exchange for a reduced pulse width (1-2 ps).

Behind the insertion devices and bending magnets, tangential to the storage ring, the beamlines are mounted. While the electrons are kept circulating in the ring, the generated synchrotron radiation is guided in these straight vacuum tubes to the experimental endstations. The main component of a beamline is a monochromator for selecting the wavelength by choosing a harmonic of the light and monochromatising it. There are different types of monochromators, depending on the kind of grating (plane, spherical, toroidal, etc.) or crystal that is mounted. The monochromators are fitted with entrance and exit slits which allow a further narrowing of the bandwidth, thus increasing the achievable resolution, but on the expense of intensity. The synchrotron beam is focussed

at a point behind the exit window of the beamline; the size and position of the focus can be influenced by more optical elements in the beamlines. Generally, the experimental set-ups are placed such that the focus of the synchrotron light coincides with the interaction region of the spectrometer used (see chapter 3.2). At the moment, BESSY II operates about 50 beamlines, offering the user photon energies from nearly zero to about 40 keV with energy resolutions  $E/\Delta E$  between 2000 and 100000 and photon fluxes in the range of  $10^9 - 10^{13} s^{-1}$ , depending on the bandwidth.

## 3.2 vacuum set-up

Throughout the PhD, two different set-ups based on magnetic bottle electron spectrometers have been used for recording electron-electron coincidences. Beforehand, investigations were focused on Auger electron-photoelectron coincidences, where the two electrons are generally of highly different kinetic energies. This allowed to use a set-up consisting of a hemispherical electron energy analyser, optimised for detection of Auger electrons, and several time-of-flight tubes, which offer sufficient resolution for the slower photoelectrons. Since in the case of ICD, the two involved electrons are both of relatively low and even similar energy, a new way had to be found. Electron spectrometers of the magnetic bottle type offer a good transmission function even for low energetic electrons and are characterised by a detection solid angle of up to  $4\pi$  sr. Therefore, they present an ideal tool for our anticipated experiments on ICD and ETMD. Since this type of electron spectrometer proved suitable in first use, it was decided to build an own one, dedicated to our specific needs.

### 3.2.1 magnetic bottle spectrometer

Before describing the two different set-ups in more detail, the functionality of a magnetic bottle electron spectrometer shall be delineated roughly first. The magnetic bottle spectrometer got its name from the shape formed by the magnetic field lines, which resembles a bottle. This is created by the use of two magnetic fields, a strong and inhomogeneous one and a weak and homogeneous one. In the first bottles [91, 92], the strong field has been generated by a large electromagnet that has two tips opposing each other. The small volume between the tips is used as interaction region of the experiment, where the ionisation events take place. Some centimeters away from that point, a so-called drifttube connects. This tube is encircled by a coil that creates a homogeneous magnetic field upon applying a current. Electrons that are generated in an ionisation event are emitted in all directions. They are captured by the field lines of the strong, inhomogeneous

magnetic field and forced to follow them towards the low magnetic field region while being parallelised. In this low field, they are guided on spirals towards a detector at the end of the drifttube.

The idea of this type of electron spectrometer originated in electron microscopy. It was then adapted to electron time-of-flight spectroscopy by Kruit and Read [91]. Whereas in their design an electric coil generates the strong and inhomogeneous magnetic field at the interaction region, later set-ups mainly use permanent magnets for this purpose [93–98]. The design of the two magnetic bottles used for the experiments presented here is an adaption of the version by Eland *et al.* [99]. Both spectrometers shall be described in chronological order, but since they are in several aspects similar to each other, details will be explained for the newly constructed spectrometer only.

### 3.2.2 ‘old’ bottle

The set-up used in the first two beamtimes on investigation of low-energetic electron-electron coincidences has been developed in a collaboration with AG Becker from the Fritz-Haber-Institute in Berlin. They provided us with a magnetic bottle electron spectrometer complete with MCP detector and a vacuum recipient that was used as interaction chamber. To be able to perform experiments on clusters, an expansion chamber had to be added (see drawing A.1). This chamber needed to match the already existing cluster sources as well as to fit appropriately to the existing spectrometer chamber. In order to attach the experimental set-up to the beamline, a frame to hold the vacuum chamber had to be constructed, which had to allow alignment of the whole set-up with respect to the synchrotron radiation.

In this set-up, the cluster beam enters the interaction region from below. The cluster source is connected to the expansion chamber, which is pumped by two small turbomolecular pumps<sup>1</sup>. The clusters have to pass a conical skimmer of 1 mm opening which is mounted on a pot-like construction that separates the expansion from the interaction chamber. In the center of the main chamber, the cluster beam is crossed with the synchrotron radiation. This point is chosen as the focus of the magnetic bottle spectrometer which is mounted horizontally in this set-up. At the top of the main chamber, a large turbomolecular pump<sup>2</sup> was connected. In the horizontal plane, opposite to the flange connecting to the beamline, a small tube and a cross are mounted which house a beam dump.

The magnetic bottle spectrometer consists of a permanent magnet (25 mm diameter) to create the strong and inhomogeneous magnetic field around the interaction

---

<sup>1</sup>Pfeiffer TPU262 and TPU240, Pfeiffer Vacuum GmbH, Berliner Strasse 43, 35614 Asslar, Germany

<sup>2</sup>Leybold T1000, Oerlikon Vacuum Germany, Industriestr. 10b, 12099 Berlin, Germany

region, and a solenoid generating a low and homogeneous magnetic field. The magnet has a soft iron cone atop which concentrates the magnetic field in its tip. In front of the cone, a small aluminium plate with a hole at the position of the cone's tip is fixed. The function of this aluminium plate is to close off the magnet with a plane surface. To this, an electric potential can be applied in order to be able to create a homogeneous electric field across the interaction region. The aluminium plate, the cone and the magnet are held in place by a peek cylinder. The cylinder is fixed onto a bottom part made of peek for insulating purposes, which in turn is fixed onto a long steel stick mounted on the magnet holding flange. The magnet set-up is attached to the interaction chamber via a small xyz-manipulator allowing for alignment of the magnet's position with respect to the entrance aperture of the drifttube and change of the distance between magnet and interaction region. The drifttube is an 'all-in-vacuum' construction. This means, that not only the drifttube itself, an aluminium tube which can be laid onto a potential, is inside the vacuum, but also the kapton wire wound around it to form the solenoid, and a  $\mu$ -metal. The drifttube is fixed into the vacuum tube with two peek rings, which at the same time serve as electrical isolators. Towards the interaction region, the drifttube is closed off with an aperture of 10 mm diameter in order to reduce background signal. At the other end, directly behind the drifttube, the detector<sup>3</sup> is placed. To ensure a good vacuum along the spectrometer, an additional turbopump<sup>4</sup> is connected next to the detector. The detector consists of two MCP plates plus a phosphor screen which can be viewed through a window in the flange. The signal is coupled out from the high voltage line of either the back MCP or the phosphor screen (anode) and is processed as described in chapter 3.3.1.

### 3.2.3 new magnetic bottle spectrometer

#### design of the spectrometer

As the above described electron time-of-flight spectrometer of the magnetic bottle type has proven suitable for investigating low-energetic electron coincidences, we decided to follow this path with our own one. The basic design is similar to the one used in the collaboration but has been changed in many details considering our experiences of the first measurements as well as plans for upcoming experiments.

The most obvious change has been done by taking the solenoid out of the vacuum. This offers numerous advantages. First of all, it is possible to remove or change the wire without breaking the vacuum. This was a major factor why the design was changed as it was anticipated (and has recently been done) to use the bottle at

<sup>3</sup>QS14953-1, Photonis USA, Inc., PO Box 1159, Sturbridge, MA 01566, USA

<sup>4</sup>Leybold TMP361, Oerlikon Vacuum Germany, Industriestr. 10b, 12099 Berlin, Germany

the free electron laser facility FLASH in Hamburg, where baking of the chamber will be needed in order to meet UHV conditions. Having no solenoid inside the vacuum anymore means less material inside the spectrometer that could outgas which also improves the vacuum. Furthermore, as space was not as limited as before inside the vacuum, a thicker wire could be used. A larger cross section reduces losses of the current flowing through and thus minimizes heat generation. An economical plus adds to this: the construction is cheaper this way since it is not necessary, or not even advisable, to use kapton insulated wire at air side. The wire chosen to wind the coil is a copper wire of 2 mm diameter with a thin lacquer layer for electrical insulation<sup>5</sup>. It is grade 2 and specified to withstand temperatures up to 200°C which even allows moderate heating of the chamber without taking off the coil at all. To implement the out-of-vacuum coil while still having the front end of the solenoid close to the interaction region, the design is such that the magnetic bottle tube protrudes into the main chamber (see figures 3.5 and 3.7 and drawing A.6). In order to fit into the other experimental set-up at FLASH, where no expansion chamber and no skimmer is close to the interaction region, an additional flange has been inserted between main chamber and bottle chamber. This results in a distance of 45 mm between interaction region and entrance of the drifttube. The field generating coil is covered by two layers of  $\mu$ -metal foil along the full length of the drifttube so that the weak magnetic field inside is shielded from the magnetic field of the earth and other stray fields.

As for most of the magnetic bottle spectrometers, there is not only the weak homogeneous magnetic field along the drifttube, but the design is such that a retarding or accelerating potential can be applied. This is achieved by having an extra tube within the vacuum tube, which is electrically isolated by peek rings (see drawings A.9 and A.12) that, at the same time, hold the inner tube in place. The in-vacuum construction of the drifttube is shown in drawing A.7. One can see that the drifttube (drawing A.11) is closed off towards the interaction region with an aperture of either 10 or 25 mm diameter (see drawing A.8). This can be laid on a potential different from the tube. For experiments presented in this thesis, the 25 mm version was used. In cases where the bottle is mounted without the spacing flange and background signal is critical, the 10 mm version should be used. Equally, the smaller aperture is the right choice when the electron spread accepted by the analyser shall be reduced, to increase the resolution on the expense of intensity, which is of advantage for non-coincident measurements, but not for coincidence experiments. At the other end, the drifttube is terminated with a copper mesh<sup>6</sup> that is fixed with a copper ring onto the drifttube (drawing A.14) and thus lying on the same potential. The mesh prevents that the high electric field of the detector intervenes into the low magnetic field region of the drifttube.

---

<sup>5</sup>W210, SYNPLEX Elektro GmbH, Auf den Kreuzen 24, 32825 Blomberg, Germany

<sup>6</sup>117.6 lines per inch, Precision Eforming, 839 NYS Route 13, Cortland, NY 13045, USA

The drifttube itself has many small holes drilled into it which are necessary in order to pump the volume between drifttube and vacuum tube. Analogous to the bottle of the first set-up, the drifttube is of 60 cm length. Although longer drifttubes would increase the resolution achievable with the spectrometer, this short length has been chosen deliberately, so that electrons of low kinetic energies (down to approx. 1.6 eV) will reach the detector within the 800 ns BESSY bunch period without additional acceleration. Applying a positive potential onto the drifttube attracts electrons and thus improves the collection angle of the spectrometer whereas a retardation caused by applying a negative potential will increase the resolution.

The detector is located directly behind the mesh that terminates the drifttube. Since we pursue coincidence measurements, where detection of as many electrons as possible is desired while imaging properties are not necessary, we have chosen a detector optimised for counting. It consists of a Chevron-type [100] MCP double stack plus a phosphor screen (P43)<sup>7</sup>. The effective area of the detector is 42 mm, the open area ratio is 60% and the gain is specified to be at least  $1 \cdot 10^6$ . The pre-assembled stack is mounted onto a specially designed ‘detector flange’ (see drawing A.15). This does not only hold the detector itself, but all electrical feedthroughs necessary for its operation as well as a window flange in the centre through which the phosphor screen can be viewed. Having the detector complete with feedthroughs on one flange offers the advantage that no additional flange is needed and mounting is facilitated. Furthermore, between beamtimes, it easily stores away in a small vacuum recipient to keep it permanently under vacuum in order to increase the MCPs’ lifetime.

To ensure a pressure better than  $1 \cdot 10^{-5}$  mbar in the vicinity of the detector, the spectrometer is equipped with an additional turbomolecular pump<sup>8</sup> close to the detector. Therefore, a small four-way-cross has been introduced at this side of the spectrometer, which is also used to connect the flange that holds the electrical feedthroughs necessary for the drifttube’s potentials. Since the extra cross and the pump present a heavy load for the welded seams of the spectrometer, threaded rods are inserted between the two flanges of the spectrometer vacuum tube as weight support. Often a crane is used to lift the spectrometer to facilitate mounting the spectrometer on top of the interaction chamber.

The strong and inhomogeneous magnetic field around the interaction region is created by permanent magnets, made of  $\text{Sm}_2\text{Co}_{17}$ <sup>9</sup>. To achieve a better defined volume of high magnetic field strength, the magnets are topped with a cone of soft iron<sup>10</sup>. The magnet mounting is designed as a modular construction and

---

<sup>7</sup>F2225-21P, Hamamatsu Photonics Deutschland GmbH, Arzbergerstraße 10, 82211 Herrsching, Germany

<sup>8</sup>TMU262, Pfeiffer Vacuum GmbH, Berliner Strasse 43, 35614 Asslar, Germany

<sup>9</sup>IBS Magnet, Kurfürstenstraße 92, 12105 Berlin, Germany

<sup>10</sup>Vacoflux50, Vacuumschmelze GmbH, Grüner Weg 37, 63450 Hanau, Germany

shown in drawing A.18. It is possible to use magnets of different sizes, together with the corresponding cone. The cones have a  $45^\circ$  geometry, and the tip is cut away to prevent magnetic saturation within the material. Depending on the base diameter of each cone, the thickness and top diameter changes. This allows to vary the strength of the inhomogeneous magnetic field as well as the size of the volume from which electrons are accepted by the spectrometer. Similar to the magnet construction of the first set-up, there exists an aluminium cap with a plane surface which sits on the cone. Additionally, there is a mesh<sup>11</sup> in front of the aluminium cap. Cone and mesh can be laid on separate potentials. This construction allows to create an electric field across the interaction region by applying a potential to the mesh, and to hinder secondary electrons, which might be emitted from the magnet's surface, from leaving the magnet and possibly entering the drifttube. The magnets, an aluminium support cylinder for the smaller magnets, the soft iron cone and the aluminium cap are held together by a peek cylinder. The mesh is fixed onto a fragile aluminium cylinder which is put over the peek cylinder. The magnets are sitting on a soft iron base which is mounted onto a peek spacer for insulating purposes. The whole construction is screwed onto a steel rod which itself is screwed onto the base flange, that also holds all necessary electrical feedthroughs. In order to align the magnet with respect to the central axis of the drifttube, the magnet holding flange is connected to the interaction chamber via an xyz-manipulator<sup>12</sup>. Care should be taken when changing the distance between the magnet and the interaction region since this influences the magnetic field towards the drifttube and thus determines the transmission properties of the spectrometer.

The solenoid is realised by winding a copper wire around the vacuum tube of the magnetic bottle as close as possible. Over the available length of 600 mm this makes theoretically about 285 windings, but practically rather 270. With typical currents of 1 A (October 2009) or 0.5 A (April 2010) applied to the coil, this generates a homogeneous magnetic field  $B_w$  of approx. 0.57 mT or 0.28 mT, respectively. The inhomogeneous magnetic field is much stronger: Measurements at the surface of the 10 mm diameter magnets, which were used in both beamtimes with the new set-up, showed a field strength  $B_s$  of about 450 mT. During the experiments, the interaction region is a few millimeters away from the magnet's surface; here, the field strength was at least 200 mT. The ratio between weak and strong magnetic field  $B_w/B_s$  is known as the intrinsic limitation of energy resolution  $\Delta E/E$  [91]. In our case it is approx.  $1.5 \cdot 10^{-3}$ .

---

<sup>11</sup>117.6 lines per inch, Precision Eforming, 839 NYS Route 13, Cortland, NY 13045, USA

<sup>12</sup>KPM12-100, VAb Vakuum-Anlagenbau GmbH, Marie-Curie-Str. 11, 25337 Elmshorn, Germany



## commissioning of the spectrometer

The energy resolution  $\Delta E_{kin}/E_{kin}$  depends linearly on the kinetic energy; the slower the electrons are, the better the resolution. In experiments on argon performed in the first beamtime with this new spectrometer, at the TGM4 in October 2009, the energy resolution has been determined as  $\Delta E_{kin}/E_{kin} \approx 1/20$ . This rather high value is due to the short flight tube and the relatively large focus spot at the TGM4.

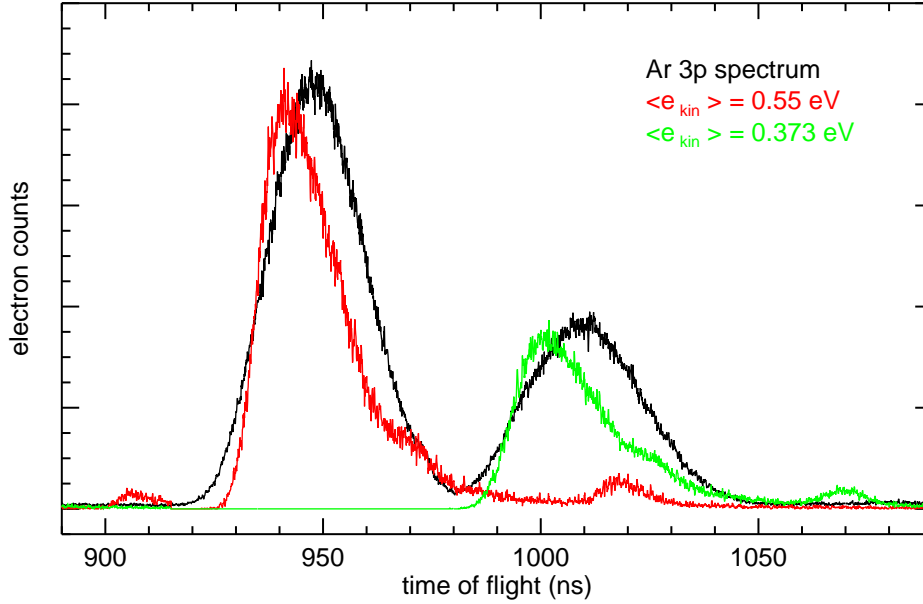


Figure 3.2: Time-of-flight spectrum of Ar 3p electrons obtained from photoionisation with 16.5 eV: experimental data are given by the black curve whereas simulated data are plotted green and red, Ar  $3p_{\frac{1}{2}}$  and Ar  $3p_{\frac{3}{2}}$ , respectively.

To validate the functioning of the spectrometer, a non-coincident argon spectrum was simulated and compared to a measured one; the result is shown in figure 3.2. The simulation was performed by the PhD-student analysing the argon spectra, by employing the software Simion<sup>13</sup>. The time-of-flight spectrum of argon was recorded at a photon energy of 16.5 eV. Potentials of +1.1 eV were applied onto aperture and drifttube of the spectrometer and of +10 eV onto the magnet while the mesh was kept grounded. For the simulation, a field strength of 250 mT was assumed for the strong magnetic field. Under the assumption of having Gaussian distributions, the size of the interaction volume was estimated as 2 mm (FWHM of gas beam) x 1 mm x 1 mm (FWHM of synchrotron radiation). Additionally, a  $\beta$  parameter of 0.16 was used for the ionisation process of Ar 3p electrons at 16.5 eV. The contributions of the Ar  $3p_{\frac{1}{2}}$  and the Ar  $3p_{\frac{3}{2}}$  electrons were simulated

<sup>13</sup>Scientific Instrument Services, 1027 Old York Road, Ringoes, NJ 08551-1054, USA

separately and are presented by the green and the red curve in the figure. Bearing in mind that the absolute position of the simulated peaks could be shifted slightly due to uncertainty regarding the time zero-position, the two spectra agree very well with each other. Nevertheless, it is interesting to observe that the peaks of the measured spectrum are more symmetric than the simulated ones.

Measurements on xenon were used to estimate the detection efficiency of the spectrometer. Gaseous xenon was ionised with 110 eV, and the resulting coincidences between Xe  $4d$  photoelectrons and Auger electrons were recorded. By comparing the number of coincidence events to the intensity of the Auger lines in the non-coincident spectra, a detection efficiency of 0.31 was found. This value includes the efficiency of the MCP detector as well as the transmission of the spectrometer at the corresponding kinetic energies.

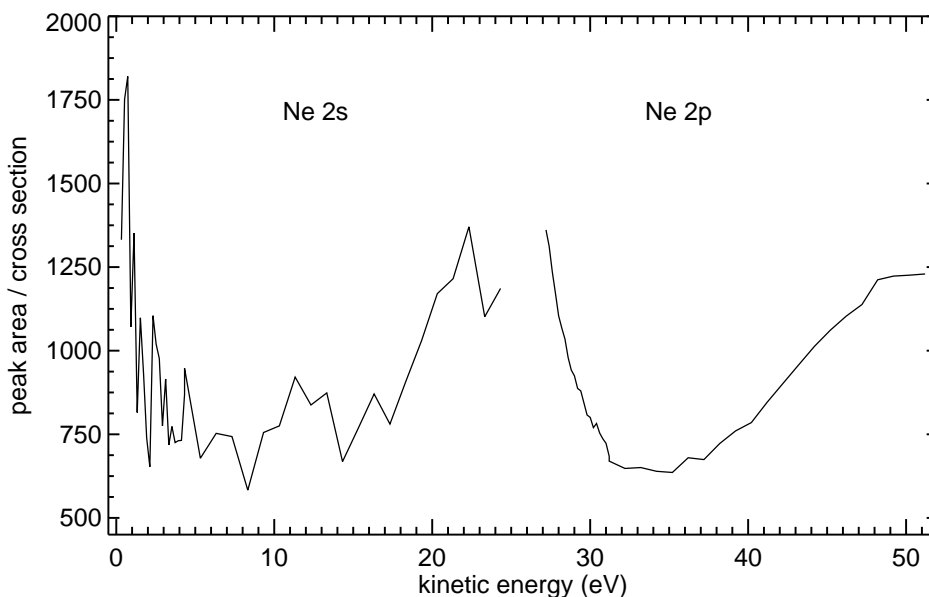


Figure 3.3: The plotted areas of Ne  $2s$  and Ne  $2p$  peaks normalised to photoionisation cross section equal the transmission function of the spectrometer conjunct with the beamline flux curve.

To experimentally determine the transmission function of the spectrometer, different attempts have been made. One of them consisted in determining the peak areas of the Ne  $2s$  and Ne  $2p$  lines from a series where the photon energy was varied systematically. In figure 3.3, these areas divided by the corresponding photoionisation cross section are plotted vs. the kinetic energy. The graph shown represents the transmission function of the spectrometer multiplied by the flux curve of the beamline. A similar graph has been found by analysing Auger peaks of xenon together with corresponding photoelectron lines (Xe  $4d$ ). Unfortunately, both attempts suffer from the lack of an exactly known beamline flux curve. Therefore, another attempt has been made by a colleague. By combining

results from a scan of Ar  $3p$  with the above mentioned xenon transmission curve, the flux curve of the beamline could be determined for a short energy range. This was then used, to extend the transmission curve by analysing a scan of He  $1s$  photoelectrons. The transmission function obtained such is given in figure 3.4. Obviously, the transmission of the spectrometer is not constant, but shows strong oscillations, especially in the lower kinetic energy range (below 20 eV). The transmission determined from analysing the neon scan matches well with this one from argon, where +1 V was applied to aperture and drifttube of the spectrometer, +10 V to the magnet and the mesh was kept grounded. Therefore, the form of the transmission function is assumed to be of this shape, but probably not being constant for different settings of the magnetic bottle spectrometer.

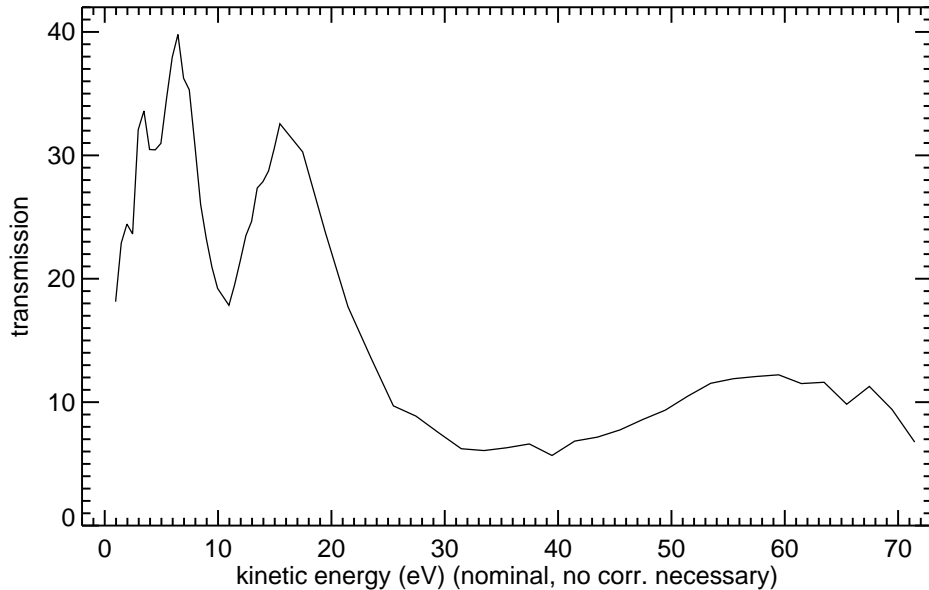


Figure 3.4: Transmission function of the magnetic bottle spectrometer obtained from scanning different rare gas photoelectron lines (see text for details).

### 3.2.4 vacuum chamber

To match all demands as being able to use the existent gas cluster source, to house the new magnetic bottle spectrometer, and to improve the conditions for experimenting with clusters, it proved necessary to design a new vacuum recipient. Since the experiments should be performed at a synchrotron, and meanwhile the whole set-up needs to be stored in the laboratory, a compact and mobile design was anticipated. In figure 3.5 a sectional view of the set-up is shown, with the apparatus being cut along the upright standing plane in the focus of and perpendicular to the synchrotron radiation.

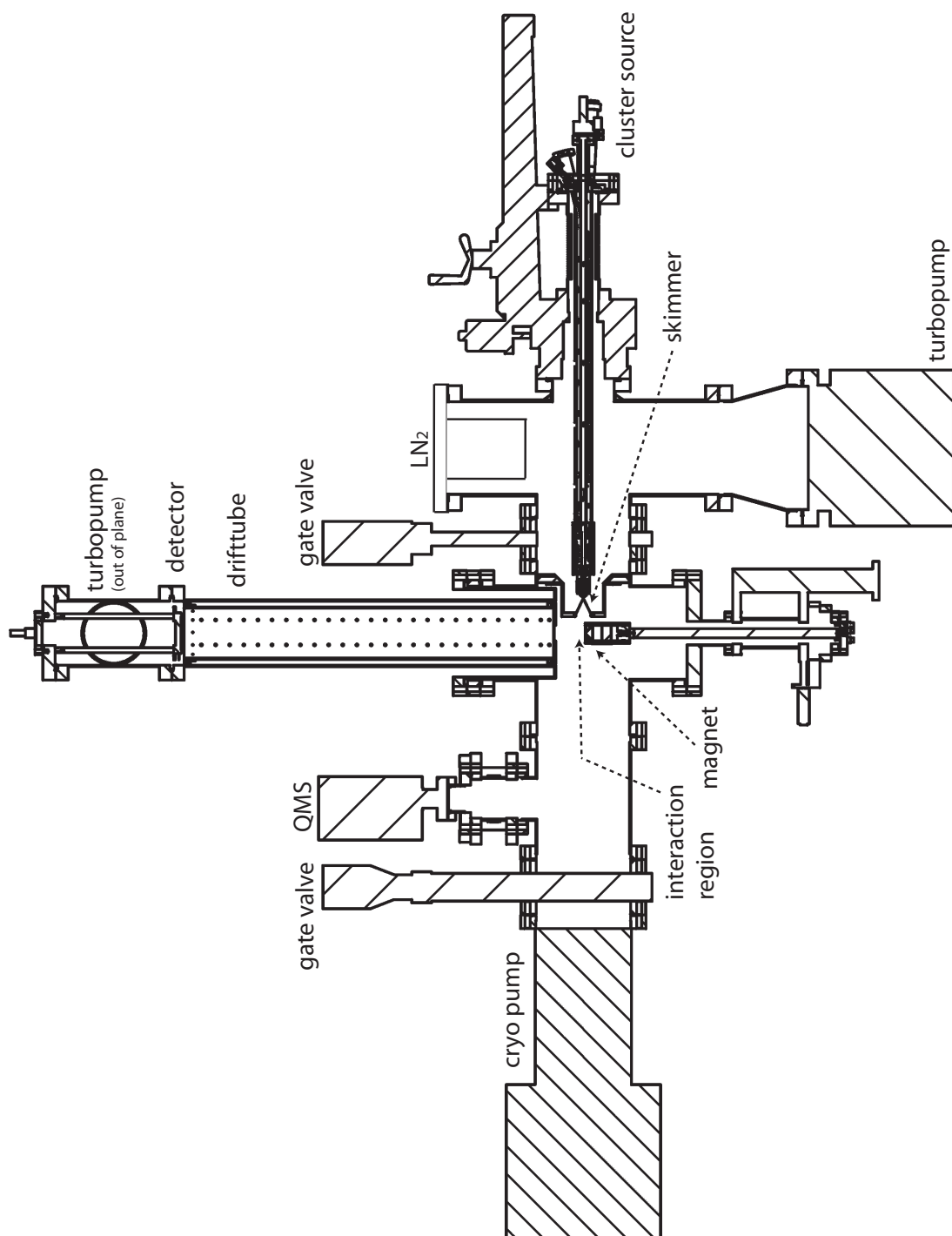


Figure 3.5: Simplified sketch of the complete new vacuum set-up presented as a cut through the interaction centre and perpendicular to the light propagation axis.

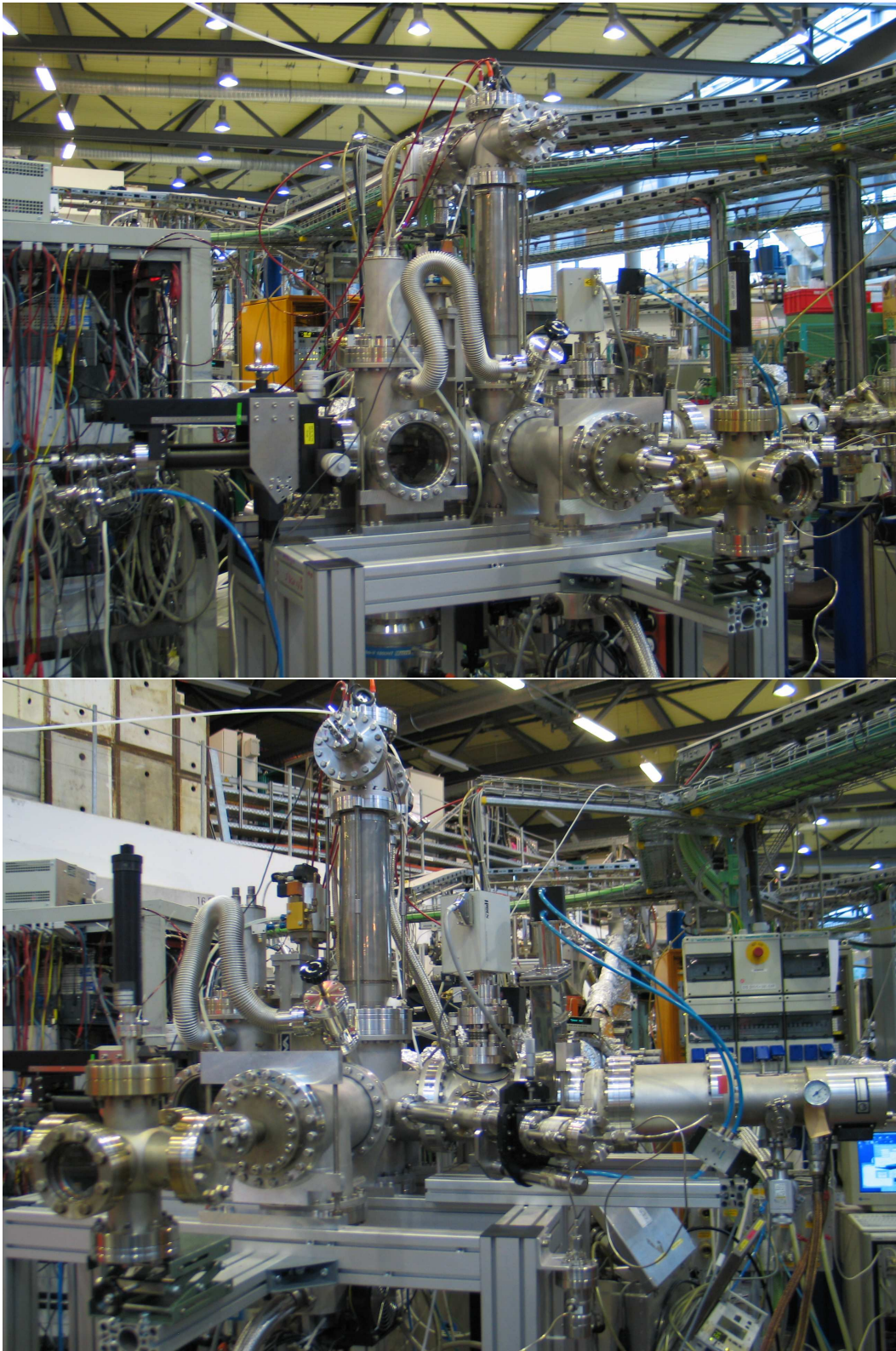


Figure 3.6: The new spectrometer and the new set-up in operation during a beamtime at BESSY II in October 2009.

In order to be consistent with already existing vacuum chambers and necessary parts, as well as being able to operate the spectrometer under ultra-high vacuum, it was decided to use conflat flanges (CF) that seal with copper gaskets. Whenever possible, stainless steel of the type 316L or, even better, 316LN was chosen for the vacuum chamber parts to prevent any influence from remaining magnetizability of the material onto the trajectories of low energetic electrons. Likewise, for all in-vacuum parts non-magnetic materials such as aluminium or copper were used, while PEEK was used for insulating parts. To reduce the amount of electrons emerging from any solid material and causing a low-energy background, parts being close to the synchrotron radiation beam were graphite coated. The spectrometer (excluding the magnet set-up) with its detachable copper wire was designed to withstand bake-out at temperatures of 250-300 °C. As recent experiments showed, it is even possible to bake the complete set-up for some days at 150° C without any impact on the spectrometer, thus reaching a pressure in the  $10^{-11}$  mbar range.

Essentially, the set-up consists of two six-way-crosses. One is used as expansion chamber for the cluster generation (drawing A.2), the other as main or interaction chamber (drawing A.3), where the interaction between the sample (species to be investigated) and the synchrotron radiation takes place and to which the spectrometer is mounted. These two chambers are connected with each other via a conical skimmer. The pot-like construction that holds the skimmer (see drawing in appendix: A.29) allows for maximum flexibility: The mounting plate can be fixed at any point within the arm of the main chamber, which corresponds to a variable distance between skimmer and interaction region. The position of the skimmer holding pot at the mounting plate is adjustable for alignment purposes. Finally, the skimmer is held in place with an o-ring and screws, instead of being glued into the pot, so that it can be exchanged to another one easily. For all experiments presented here, skimmers of 1 mm opening diameter were used; in the first set-up one manufactured from aluminium in a workshop, and in the new set-up a commercial one made of copper<sup>14</sup>. To prevent damage to the skimmer when venting or evacuating the whole apparatus, expansion and main chamber share a second connection with each other via a bellow, which is closed during normal operation.

The cluster source is mounted horizontally in the new set-up and is connected via an xyz-manipulator to the expansion chamber. This is necessary, since clusters of different type or different sizes populate other parts of the cluster beam, and, therefore, the source has to be moved with respect to the skimmer. Apart from a large turbomolecular pump<sup>15</sup>, a container for liquid nitrogen is mounted on the expansion chamber. Water and other condensable gases adsorb at its surface

<sup>14</sup>Beam Dynamics, Inc., 13749 Shelter Cove Drive, Jacksonville, FL 32225-5428, USA

<sup>15</sup>Varian V1000 HT, Agilent Technologies, Alsfelder Strasse 6, Postfach 111435, 64289 Darmstadt, Germany



and thus the background pressure is reduced. The expansion chamber can be completely isolated from the main chamber by closing a gate valve<sup>16</sup>. This allows to change the cluster source and to take the LN<sub>2</sub> container off for regeneration without venting the interaction chamber and the spectrometer. Especially when performing experiments under pressure of time, as is the usual case during a beamtime, this is a big advantage since the spectrometer will be kept clean and the microchannel plates of the detector do not need to be ramped up again.

After passing the skimmer, the cluster beam is crossed perpendicularly with the synchrotron radiation in the centre of the interaction chamber, which lies on the central axis of the magnetic bottle spectrometer. A zoom into the 3-dimensional model of the set-up around the interaction region is shown in figure 3.7. The photo in figure 3.8, which has been recorded when setting up the experiment for the first beamtime, gives a view into the interaction region from the top.

In the new set-up, the spectrometer is mounted vertically with the magnet

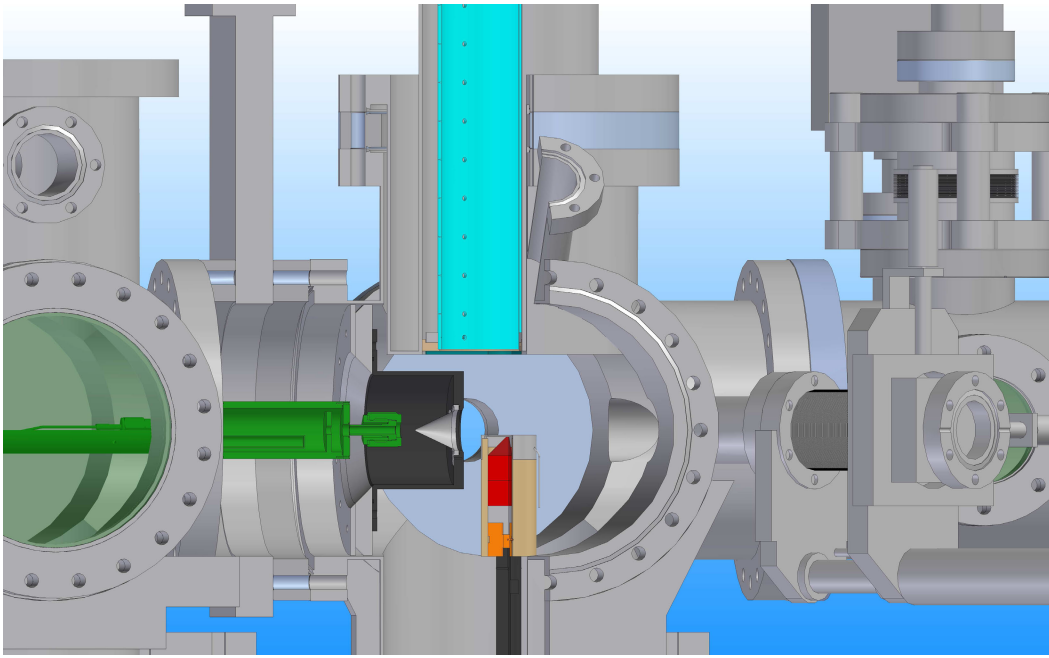


Figure 3.7: 3-dimensional presentation of the central part of the new set-up showing the water cluster source (green, left), the skimmer (grey), the magnet (red, bottom) and the drifttube (cyan, top).

approaching the interaction region from the bottom and the drifttube pointing upwards. (For experiments at FLASH it is mounted the other way round.) This means that the spectrometer axis is perpendicular to the cluster beam as well

<sup>16</sup>10844-CE01-0004, VAT Deutschland GmbH, Am Hochacker 4, 85630 Grasbrunn bei München, Germany

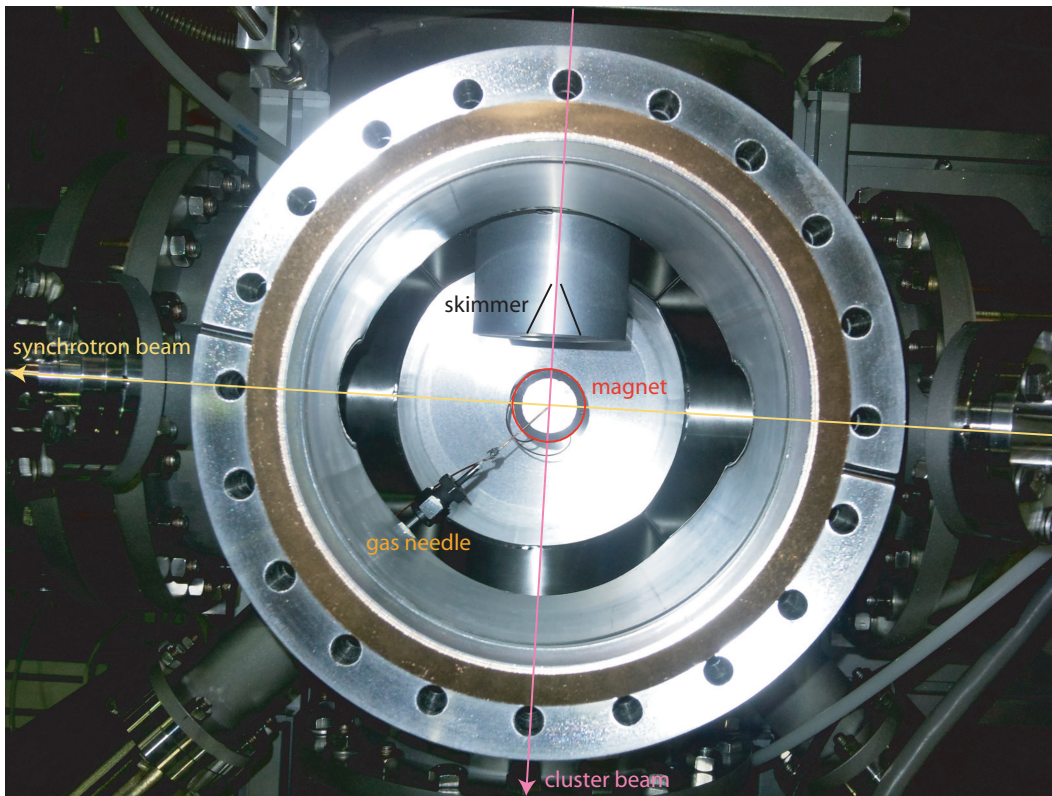


Figure 3.8: View from top into the interaction region. In the middle, the magnet (red circle) can be seen. At top in the picture is the skimmed jet (black lines) in its mounting pot through which the cluster jet (pink) enters the interaction chamber. The gas needle (orange) is mounted at the lower left. The synchrotron radiation (yellow) crosses from right to left. The drifttube of the spectrometer (not shown) it is vertically mounted, out of the picture plane.

as to the light propagation direction. After passing the main chamber the clusters fly through another small vacuum chamber (see drawing A.4). This houses a small quadrupole mass spectrometer (QMS)<sup>17</sup> which is capable to analyse neutral species in a cross-beam geometry. In the QMS we aim at detecting the unfragmented clusters, which have not interacted with the synchrotron radiation, to gain information on the size distribution in the cluster jet. Since the alignment of the cluster beam is given by the interaction with the synchrotron radiation, the mounting of the QMS needs to be moveable, which is achieved by employing a bellows with alignment studs. Behind this chamber, a cryogenic pump<sup>18</sup> is mounted, and the cluster beam is directed straight into it. In order to allow regeneration of

<sup>17</sup>Hidden Analytical, Vacua GmbH, Niedmannweg 13, 82431 Kochel am See, Germany

<sup>18</sup>Leybold RPK 900 Kryo, Oerlikon Vacuum Germany, Industriestr. 10b, 12099 Berlin, Germany



the cryogenic pump without venting the spectrometer, the main chamber can be closed off here by another gate valve. Along the direction of the light propagation, a large T-shape recipient is attached to the main chamber. It serves to connect a large turbomolecular pump<sup>19</sup> and, in the horizontal plane, a beam-dump. This is like a small cone made of copper into which the synchrotron radiation is directed in order to prevent any light reflection as well as possible electron emission that could generate a background in the spectra. The beam-dump is mounted on a linear stage so that it can be aligned to the synchrotron radiation, or moved out of the light beam, which is necessary to observe the white light for alignment purposes. Next to the cone is a conductive plate; plate and beam-dump allow to measure the current of the synchrotron radiation. In the plane formed by the cluster beam and the synchrotron radiation, the chamber has additionally been equipped with two smaller flanges. One of them has a gas needle attached via a small manipulator and a bellow with alignment studs. This needle is used as gas-inlet for recording reference spectra that are free of clusters. Another advantage of not using the cluster source for this purpose is the lower consumption of gas. The other small flange is a window flange through which the interaction region can be observed, which is especially useful when moving the magnet or the gas needle. Since there is only little space behind this flange, a small camera has been attached to it, offering the advantages of digital images and on-line monitoring. The last of the main chamber's six large flanges is needed for the connection to the beamline. Since the working pressures in the main chamber can be much higher than the  $10^{-9}$  mbar that BESSY requires to allow the beamshutter to be opened, a differential pumping section is interconnected between chamber and beamline. This section consists of two small volumes, each pumped by its own small turbomolecular pump<sup>20</sup>. They are connected via a capillary through which the synchrotron beam has to pass. Capillaries help separating volumes of different pressures by reducing the open cross section between them. For this reason, another capillary has been inserted between the differential pumping section and the main chamber. In the connection tube to the beamline, a copper plate with a hole of 25 mm diameter was used as gasket directly behind the last beamline valve. It was observed, however, that inserting the copper plate makes pumping more difficult due to enclosed volumes. Therefore, an additional small turbo-pump was inserted into the tube connecting the beamline and our set-up during the last beamtime.

The whole vacuum apparatus is mounted onto an aluminium frame<sup>21</sup> and is fixed

---

<sup>19</sup>October 2009: Leybold TurboVac 360, Oerlikon Vacuum Germany, Industriestr. 10b, 12099 Berlin, Germany; April 2010: Pfeiffer TMU521YP, Pfeiffer Vacuum GmbH, Berliner Strasse 43, 35614 Asslar, Germany

<sup>20</sup>Varian V300HT, Agilent Technologies, Alsfelder Strasse 6, Postfach 111435, 64289 Darmstadt, Germany

<sup>21</sup>minitec, W&P Geat GmbH, Vollmerstr. 13, 12489 Berlin, Germany

to it by adapting plates. The frame has wheels<sup>22</sup> underneath, so that the set-up can easily be moved between laboratory and beamline. To connect the vacuum chamber to the beamline, it has to be lifted up. This is possible with special feet<sup>23</sup> adapted to it. The feet themselves stand on glass plates. To align the set-up with respect to the synchrotron radiation is easy: leading pressured air through the feet lifts them slightly and they can be shifted on the glass plates with the help of micrometer screws<sup>24</sup>. When the chamber is found to be at the right position, the pressured air is turned off and the set-up is fixed in its position.

In the schematic representation of the set-up given in figure 3.9, the valves, pumps and pressure gauges are shown. The pressures in the expansion and main chambers are monitored by wide range pressure gauges<sup>25</sup>, and to the differential pumping section an ionisation gauge<sup>26</sup> is connected. The turbomolecular pumps of the different parts, expansion chamber, main chamber plus spectrometer, and differential pumping section, are each backed by dry scroll pumps<sup>27</sup>. Without baking, a background pressure in the low  $10^{-7}$  mbar range can be reached. During operation, the pressure in the main chamber can increase up to  $1 \cdot 10^{-5}$  mbar and in the expansion chamber even up to  $1 \cdot 10^{-3}$  mbar, due to the large amount of gas needed for the cluster generation. If the pressure exceeds pre-set values (around  $5 \cdot 10^{-5}$  mbar in the main chamber or  $1 \cdot 10^{-7}$  mbar in the differential pumping section), then an interlock system will come into action causing the valves in the beamline and the beamshutter to close. Furthermore, the high voltage of the detector will be switched off to prevent any damage due to over-currents.

### 3.2.5 cluster generation

As can already be inferred from the table of contents of this thesis, two different types of clusters were investigated: rare gas clusters and water clusters. Whereas the gases have to be cooled down in order to form clusters, the liquid water has to be heated up. Therefore, two different types of cluster sources were used. All sources are designed such that a laser beam can be lead through the whole source and the nozzle for alignment purposes.

---

<sup>22</sup>L-RD 182R-FI-VLI, Blickle Räder+Rollen GmbH u. Co.KG, Heinrich-Blickle-Str. 1, 72348 Rosenfeld, Germany

<sup>23</sup>lifting spindle: MULI3-V, Danaher Motion GmbH, Postfach 340161, 40440 Düsseldorf, Germany; foot: norelem Normelemente KG, Postfach 1163, 71706 Markgröningen, Germany

<sup>24</sup>BM25.63, Newport Spectra-Physics GmbH, Guerickeweg 7, 64291 Darmstadt, Germany

<sup>25</sup>atmion (=pirani+ion gauge), Vacom GmbH, Gabelsberger Str. 9, 07749 Jena, Germany

<sup>26</sup>Varian, Agilent Technologies, Alsfelder Strasse 6, Postfach 111435, 64289 Darmstadt, Germany

<sup>27</sup>Edwards Xds35i and Xds10i, EDWARDS GmbH, Ammerthalstrasse 36, 85551 Kirchheim, Germany; Leybold Scrollvac SC15d and SC5d, Oerlikon Vacuum Germany, Industriestr. 10b, 12099 Berlin, Germany

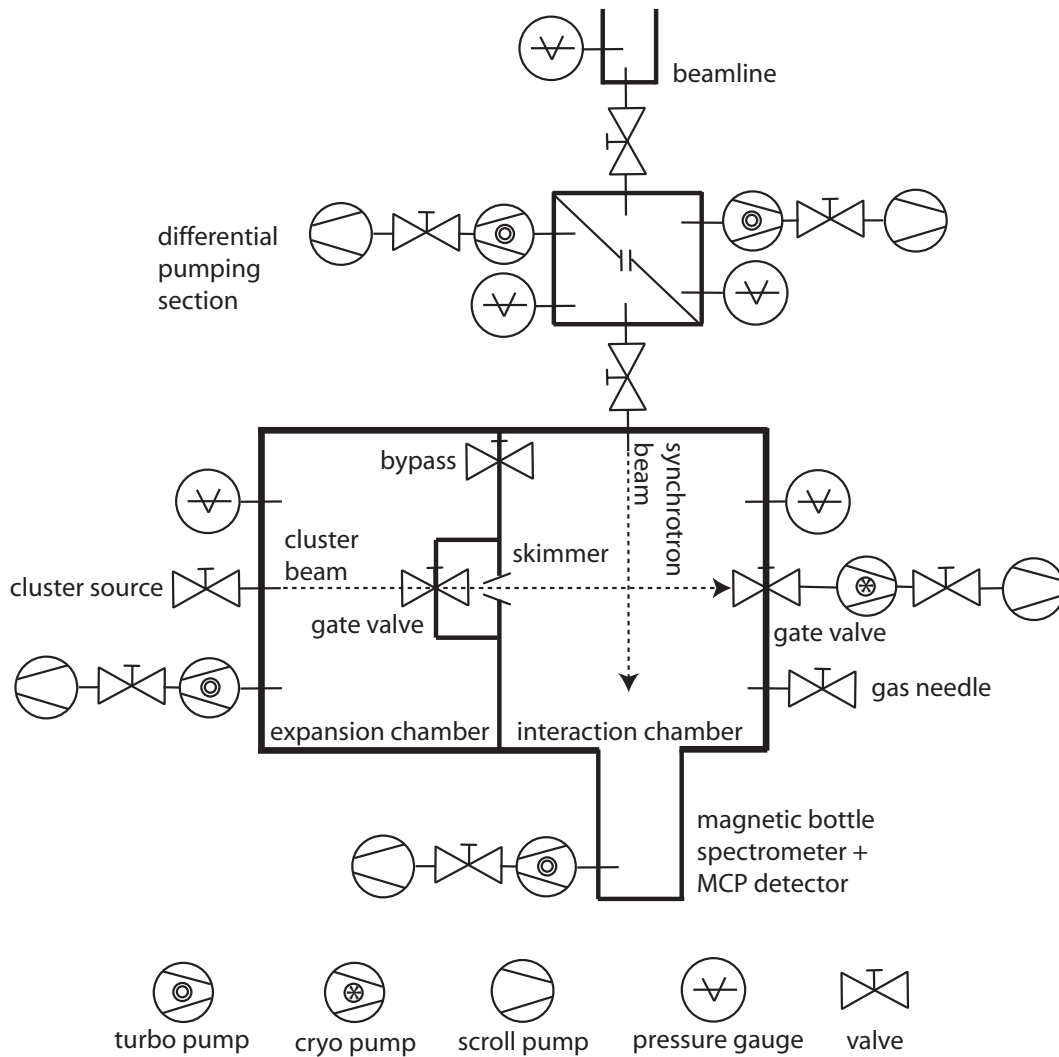


Figure 3.9: Schematic representation of the set-up showing valves, pressure gauges and pumps.

The gas cluster source has been designed by a former PhD student of our group. Since it is described in detail in his thesis [101] it shall be delineated only briefly. Simplified, the source consists of a mounting flange (DN63CF) that holds all necessary feedthroughs, and a tube that houses the different supply tubules and cables. The nozzle is screwed onto the other end of the tube, which means it can easily be exchanged to one of a different open diameter. All nozzles are conical and have a half opening angle of  $15^\circ$ . The nozzles are made of copper for good thermal conductivity and can be cooled down to the desired working temperature with liquid nitrogen or liquid helium. An electronically controlled heater helps running the source at stable temperatures. Additionally to the temperature reader, a pressure gauge determines the stagnation pressure of the gas behind the nozzle.

For the generation of gas clusters, nozzles of 50 and 100  $\mu\text{m}$  diameter were used. Depending on the sample gas and the desired cluster size, stagnation pressures were varied between 0.5 and 2.5 bars, and nozzle temperatures were in the range of 40 to 180 K. When cooling down to such temperatures, care has to be taken that water does neither get into the cooling line nor into the gas tubule, because it will freeze out and thus prevent cooling of the nozzle or hinder the gas flow, respectively. Mixed rare gas clusters can be produced with this source via the coexpansion method (see chapter 2.1). For this purpose the gases were mixed with the desired composition beforehand in an external reservoir. To produce mixed clusters via the pick-up technique, an additional gas needle is needed to deliver the doping gas.

The water cluster source that has been used in the first set-up was designed by another former PhD student of our group, and is described in his thesis [25]. Since it was not suitable for horizontal operation as demanded by the new set-up, a new water cluster source had to be constructed. The water cluster sources are characterised by an in-vacuum reservoir that is equipped with a powerful heater<sup>28</sup>. The reservoirs can be filled with liquid water without opening the vacuum chamber. Heating up the water generates vapour, which is then expanded into the vacuum through the same type of nozzles as used for the rare gas clusters. In contrast to the gas cluster source, the nozzles of the water cluster sources are covered with a heating jacket<sup>29</sup>. They are heated up to temperatures above the reservoir temperature in order to prevent condensation. For all experiments with water clusters, a nozzle of 80  $\mu\text{m}$  diameter was attached to either source. To control the functioning of the sources and to be able to estimate the cluster sizes, thermocouples<sup>30</sup> are attached to the reservoir and the nozzle. Compared to the former water cluster source, our teamwork approach allowed to improve the new design (see drawings A.20 to A.28) in multiple ways. The volume of the in-vacuum water reservoir was increased to about 30 ml which allows for a longer uninterrupted operation time ( $\approx 6$  hours). To achieve this under consideration of maximum dimensions given mainly by the manipulator, a wall with a small opening was introduced into the reservoir, just behind the nozzle. To give a visual impression, a cut view of the 3-dimensional model is shown in figure 3.10. Hence, the larger volume can be filled nearly ‘to the rim’, but only the water vapour will fill the small volume right behind the nozzle. This small extra volume can later be used to store solid samples that are picked up by the water vapour prior to the expansion process, thus producing doped water clusters. The water supply lines within the reservoir are now arranged in a way that allows horizontal as well as vertical (pointing upwards) operation. Furthermore, all necessary electrical feedthroughs and water lines are now contained on a single flange. This flange

<sup>28</sup>20 W firerod, Watlow GmbH, Lauchwasenstr. 1, 76709 Kronau, Germany

<sup>29</sup>10 W silicon heating element, Watlow GmbH, Lauchwasenstr. 1, 76709 Kronau, Germany

<sup>30</sup>NiCr-Ni (= type K), Roessel Messtechnik GmbH, Spenerstraße 1, 01309 Dresden, Germany

also holds a small window flange in its center, and the wall within the reservoir a small window<sup>31</sup>, to keep up the possibility of using the alignment laser.

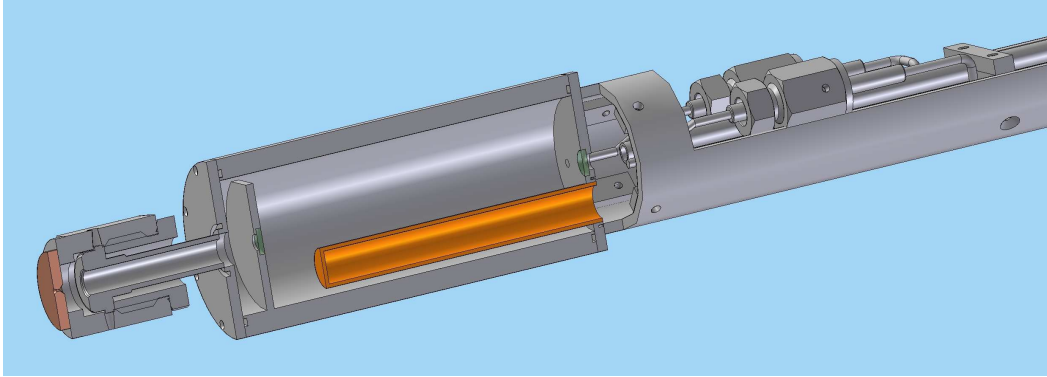


Figure 3.10: Inside view of the new water cluster source. Within the large reservoir a heating patron is held (orange). To the right the mounting half tube can be seen; to the left the detachable nozzle construction (here without heating jacket).

### 3.3 from experiment to spectrum

#### 3.3.1 electronics

Due to the large collection efficiency of the spectrometer ( $4\pi$  sR), almost all electrons generated in an ionisation event are captured and guided efficiently towards the MCP detector by the homogeneous magnetic field. To operate the detector, high voltages of, typically, up to 2.3 kV across the MCP stack and 3 kV for the phosphor screen are needed. These are provided separately by precision high voltage power supplies<sup>32</sup>. The MCP high voltage is split by resistors, so that the front MCP receives a fraction proportional to the total input voltage (about 200 V). This voltage serves to accelerate the electrons from the mesh that terminates the drift tube towards the MCPs, which increases the sensitivity of the detector. Electrons hitting the front MCP generate secondary electrons which are then accelerated onto the second MCP due to the high voltage applied along the MCP stack. In total, a whole cascade of electrons is generated for each electron arriving at the detector [100]. The current flowing thus leads to a short breakdown of the high voltage, which can be coupled out from the high voltage

<sup>31</sup>sapphire window, 43365, Edmund Optics GmbH, Zur Gießerei 19-27, 76227 Karlsruhe, Germany

<sup>32</sup>NHQ 235M, iseg Spezialelektronik GmbH, Bautzner Landstr. 23, 01454 Radeberg, Germany

line by introducing a capacitor. The signal obtained this way from the back MCP typically is in the 10 mV range.

In order to be able to process the signal in the subsequent electronics, it has to be amplified. For this purpose, three inverting broad band amplifiers<sup>33</sup> are used in series. They work in a frequency range from 50 to 1000 MHz and are characterised by an amplification of approx. 10 dB. The amplified signal is then fed into a constant fraction discriminator (CFD)<sup>34</sup>. The CFD threshold defines above which voltage events are counted as such, and the width determines the minimum separation between two events (dead time). If both are set appropriately, the CFD allows to determine the arrival times of the electrons independently of the signal height, which varies from pulse to pulse.

The flight times are then transferred to a multi-hit capable time-to-digital converter (TDC)<sup>35</sup> with 60 ps bin width. The TDC is able to record multiple events on one channel within the same measuring cycle and thus allows an event based data acquisition.

To measure flight times, a reference signal is needed. For this, the so-called bunch marker signal (TTL type) provided by BESSY II is used. This signal is generated in a high frequency cavity in the storage ring and thus has the same period as the revolution time of the electrons, 800 ns. The bunch marker is not only used as a start signal for the measuring cycle but also to generate a counter signal which is necessary to discriminate between signals from different bunches (time-signature). The combination of bunch marker and counter allows for a user-defined data acquisition time. In a measurement, the bunch marker starts the two chips of the TDC alternatingly with each new cycle, thus avoiding dead times while reading out the signals. The signals that arrive from the CFD at the channels of the TDC are used as separate stop pulses, each presenting a flight time relative to the bunch marker. The TDC records the time at which the channels received stop signals and writes it into the status information together with the channel number. These data (four bytes of bunch marker information, two bytes of time information, and two bytes of status information) are then transferred to a PC.

The physical time zero position can be determined by recording the small signal recorded on the detector, which is generated by synchrotron radiation that was reflected at the clusters. This so-called prompt signal is electronically shifted by inserting delay cables until it appears only a few channels after starting time counting. This serves to make the available time-window for the time-of-flight measurement as long as possible. Nevertheless, an accelerating potential applied

---

<sup>33</sup>ZHL-1010+, Mini-Circuits, P.O. Box 350 166, Brooklyn, NY 11235-0003, USA

<sup>34</sup>CF4000 quad, EG&G Ortec: AMETEK GmbH, Rudolf-Diesel-Strasse 16, 40670 Meerbusch, Germany

<sup>35</sup>GPTA mbH, Dölmener Pfad 5, 13507 Berlin, Germany

to the drifttube of the magnetic bottle might be necessary to ensure that even the slowest electrons (down to zero eV) arrive at the detector before the next ionisation event takes place. Preventing an overlap between slow electrons from one ionisation event and fast electrons from the next ionisation event proved necessary for our data analysis. In order to determine the background signal (random coincidences) correctly, always two following time frames are analysed.

The data acquisition program, `elecion 1.82` <sup>36</sup>, counts the number of electrons that arrive within the measuring range of the TDC, which can be set to one or several periods. In our experiments, two frames of each 800 ns were recorded (see above). It allows on-line monitoring of the integrated spectra and coincidence plots and saves the data in so-called event lists for off-line analysis.

### 3.3.2 coincidence technique

The co-occurrence of two or more events within a certain time interval is called a coincidence. The use of a coincidence technique allows an unambiguous assignment of electrons to processes involving a fixed number of electrons [80]. For the investigations on ICD presented in this thesis solely coincidences of exactly two electrons were considered. In the off-line analysis, using the software IDL 6.0 <sup>37</sup>, the number of electrons and their corresponding flight times written in the event lists are read into a buffer. Histograms are created by sorting the events according to their flight time information. Moreover, routines have been programmed in IDL that allow to create two-dimensional coincidence maps. For this purpose, coincident electron pairs from two measuring intervals directly following each other are considered. Since the two electrons are indistinguishable except for their times-of-flight, each pair consists of a slow and a fast electron. The pairs are plotted into a diagram whose axes correspond to the times-of-flight; the vertical one represents the faster electron (named  $e_1$ ) and the horizontal one the slower electron ( $e_2$ ). An example for a time-of-flight coincidence plot is given in figure 3.11.

A recorded electron pair can represent either a true or a random coincidence. True coincidences are generated in processes based on the absorption of a single photon, such as ICD, Auger decay, direct double ionisation and even scattering; or in other words, they originate from the same ionisation event. Random coincidences instead result from electrons generated in different ionisation events but being accidentally recorded within the same time window.

In gas phase experiments with synchrotron radiation the parameters are usually chosen such that the event rate per measuring interval is generally much smaller

---

<sup>36</sup>Wieliczek, Kornel

<sup>37</sup>ITT Visual Information Solutions, Talhofstrasse 32 S, 82205 Gilching, Germany

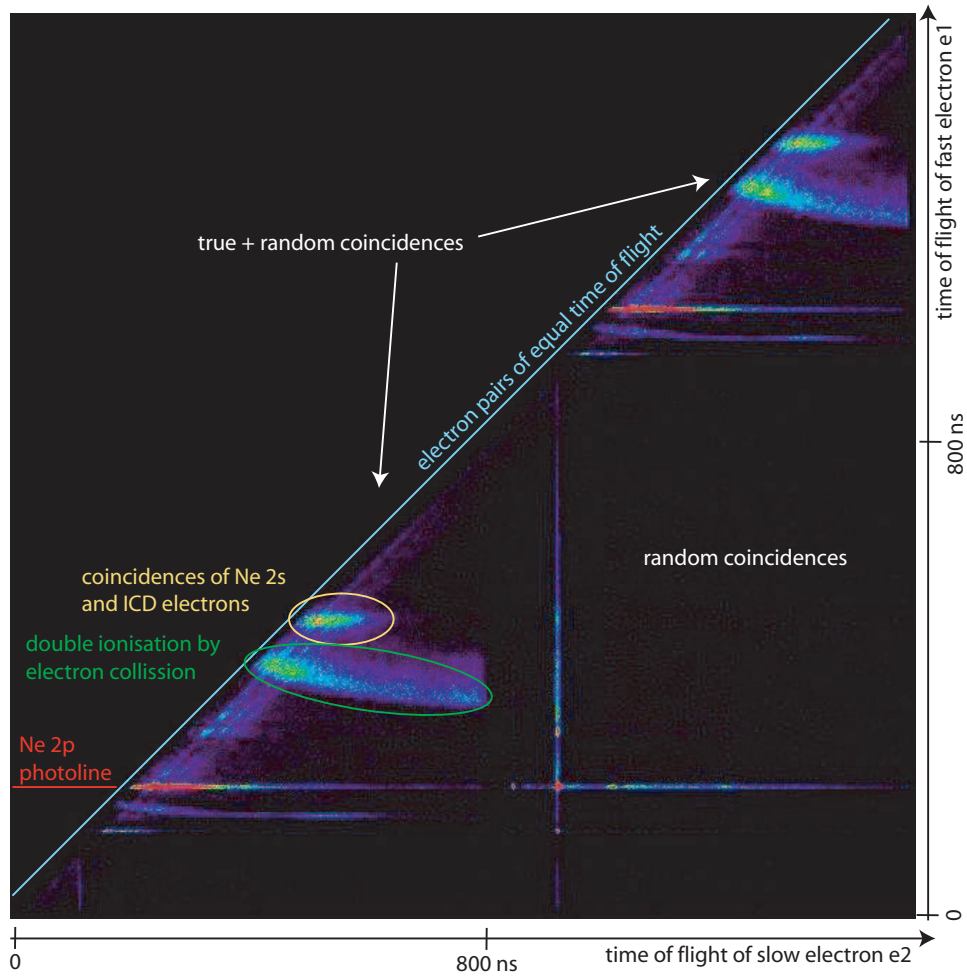


Figure 3.11: Time-of-flight map of coincidence events from neon clusters recorded in two subsequent measuring intervals.

than one. Since the electrons from random coincidences are emitted independently from each other, the probability of a random coincidence evolving from different measuring intervals is the same as for one formed in the same interval. Electron pairs created by two different synchrotron pulses occur only in the lower right square of the coincidence map shown in figure 3.11. Since these are all random coincidences, this part of the map can be used to estimate the background contribution. In the lower left triangle of the time-of-flight coincidence map, on the other hand, the true plus random coincidences of the first measuring window are plotted, and analogous the coincidences of the second window in the upper right triangle. It should be noted, that in an ideal experiment these two triangles are expected to be identical. From figure 3.11, it can be seen that the number of coincidences from the same measuring interval (triangle) is much larger than



of coincidences from different measuring intervals (square). Calculating this difference for each pair of electron flight times yields the map of true coincidences where only electron pairs that are created by double ionisation events are plotted. To improve the statistics, the two triangles are summed up point by point and then twice the ‘random coincidences square’ is subtracted. If an electron group (e. g. the photoelectrons) possesses a non-continuous spectral distribution, then for some flight time coordinates more coincidences will show up than in other ranges.

In the time-of-flight coincidence map (see figure 3.11), one can distinguish between three different types of features: round or oval islands, hyperbolae and straight lines. True coincidences show up as islands or hyperbolae. Depending on the initiating ionisation process, the islands represent coincidences of Auger electron plus photoelectron or the sought after ICD electron plus photoelectron-pair. The hyperbolae instead are created by two electrons sharing the available kinetic energy continuously as is the case for direct double ionisation processes. The straight lines are generated by accidentally recording photoelectrons or Auger electrons together with another electron.

In order to obtain coincidence plots that are comparable with each other, the flight times have to be transformed into kinetic energies. For this energy calibration, a reference measurement has to be performed. Typically, a noble gas (atomic) with a photoline of exactly known binding energy is used. A series of photoelectron spectra is recorded, where the photon energy is varied in small steps so that the kinetic energy of the photoelectron covers the whole range from threshold (zero) to the highest value needed for the plot. The correctness of the photon energy, i. e. the precision of the monochromater, has also to be checked. For this, the actual energetic position of the photoline, determined by scanning the photon energy and recording the total electron yield, is compared to reference values from literature.

In the analysis, the channel number where the photoline appears is determined for each spectrum; a single channel corresponding to 60 ps flight time. A conversion table is compiled, containing the channel numbers and the kinetic energies known from the photon energies used in the scan and equation 2.2.1. The table data are then interpolated (spline) and reformed to an equally spaced energy scale. Knowing the matching kinetic energy for each channel number, the coincidence spectra can now be converted. In order to obtain the correct spectral intensity, the spectrum itself has to be transformed after conversion of the axes. The intensity distribution vs. energy  $I_E$  is obtained from the spectrum over time  $I_t$  via  $I_E = -I_t \frac{dt}{dE}$ .

The result of this time-to-energy conversion is a two-dimensional plot of coincidence events per energy interval<sup>2</sup>, where each point in the map represents an event where two electrons have been recorded as a true coincidence. Since the

fast electrons ( $e_1$ ) are plotted along the vertical axis and the slow ones ( $e_2$ ) along the horizontal axis, only the upper left triangle is covered. Along the main diagonal, the two electrons of a pair have the same time-of-flight and thus the same kinetic energy. Due to electronic reasons it is not possible to detect these pairs. Depending on the width set on the CFD and thus the induced dead time before another signal can be processed, the gap between the coincidence triangle and this diagonal might even increase.

The features of the time-of-flight coincidence map can, of course, still be found in the energy map. Random coincidences with photoelectrons or Auger electrons still turn up as straight lines at the corresponding kinetic energy. When a photoelectron is measured as true coincidence with a second electron, a round or oval feature can be found, the exact shape depending on the energy range of the second electron. A characteristic for direct double ionisation is the continuous energy sharing of the available excess energy between the two emitted electrons (see equation 2.2.3), which results in a sharp diagonal feature (top left to bottom right, constant total energy). If instead a broad diagonal feature is underlying the map, then this points to intra-cluster scattering. The available energy is distributed randomly between the two electrons involved in the collision process. Since the photoelectron emerges from a cluster and not an atomic species the possible energy range is broader. In some of the maps, intensity at very low kinetic energies of both electrons appears. Its origin is not yet 100 % clear, it probably stems from inter-cluster scattering, some apparatus-induced background and probably more, so far undesigned, physical processes. Maps obtained from experiments with the new magnetic bottle set-up do sometimes show striations, starting at the main diagonal and becoming weaker the further away from it. These were found to be an electronic artifact. They were corrected for by performing a diagonal summation and then finding a correction function that pulls/ lifts values to the main curve when multiplied.

Since in most cases the ICD electron is generally expected to be slow (below 2 eV), the photon energy is chosen such that the photoelectron is of higher kinetic energy so that both electrons can be clearly separated from each other. This means, that usually the photoelectron is the faster electron which is plotted along the vertical axis, and the slow ICD electron is plotted along the horizontal axis. In the coincidence maps, this region of interest is framed by two lines (in most cases horizontal and red) throughout this thesis. To obtain the energy spectrum of the ICD electron, coincidence counts within this region of interest are summed up vertically. The resulting spectrum is plotted in the top panel. In order to obtain the spectrum of photoelectrons for which a second electron was recorded in coincidence, a summation in horizontal direction over the whole map is performed. The spectrum is then plotted to the left or right of the map. This spectrum is not equal to a photoelectron spectrum recorded by not using a coincidence technique, since no events of single electron emission are accounted for. Another type of

spectrum that can be gained from the map is the representation of coincidence events vs. final state binding energy. For this spectrum, coincidence events are summed up where the total kinetic energy of the two electrons of each pair is constant, as represented by green arrows in the maps.

Due to the large acceptance angle and good transmission of the spectrometer, the accumulation times for coincidence plots are relatively short ( $< 30$  min). The exact time depends very much on the cross section of the initial ionisation process, the intensity of the synchrotron radiation and the signal processing parameters. For example, for the time-of-flight map obtained from irradiating neon clusters with 51.8 eV photons, which is shown in figure 3.11, a total number of ca. 208200 coincidences was recorded within 300 s. The true coincidences of the Ne 2s electron-ICD electron pair amount to 6950.

### 3.3.3 beamtime

Experiments that need synchrotron radiation are not of the laboratory type but equal a measurement campaign. The beginning is nevertheless the same: deciding for the physical effect to be investigated, choosing the best suitable method and selecting appropriate sample species. The experimental technique determines whether single or multi bunch mode has to be used and the ionisation potentials that have to be reached dictate the necessary photon energy range. With these parameters in mind, a beamtime application can be submitted, in the case of BESSY this is possible twice a year and about half a year in advance. A beamtime is typically two weeks and is carried out as group work due to the fact that shifts are either 12 (undulator beamline) or even 24 hours per day (dipole beamline).

In order to save the valuable beamtime exclusively for activities that demand synchrotron radiation, the experimental set-up is assembled beforehand as far as possible. It is then transferred to the beamline and connected to the end of it. Now, the pre-alignment takes place: A laser beam is shot through the cluster source which is fixed in its central position. The vacuum chamber is then moved until the laser beam crosses the focus of the white light (zero order of the synchrotron radiation) in the central point of the interaction chamber. Finally, the skimmer is fixed between expansion and main chamber such that the laser beam can pass through. Once the set-up is pre-aligned, the last parts are installed and the chamber is closed. After the peripheral instruments such as pumps, cooling water, pressured air and electronics are connected, the vacuum recipient is pumped down. To improve the pressure toward the beamline, the differential pumping section is baked out at moderate heat for about 12 hours. The high voltage supplies for the detector are not ramped up before pumping about half a day in order to avoid electrical sparkover or destruction of the MCPs. When the experiment is ready for operation, the alignment of the chamber is fine-adjusted

by monitoring the count rate and the signal to noise ratio of a photoionisation signal from a reference gas. Furthermore, suitable parameters for the potentials applied on the drifttube and magnet, for the monochromator and apertures in the beamline as well as for the electronics have to be found and set in order to be able to record coincidences of significant number and with sufficient resolution. These preparatory procedures usually take two to three days. Additionally, for all measurements of interest, calibration scans for the time to energy conversion have to be recorded. The effective beamtime can unfortunately be further reduced if anything is not working properly and needs to be repaired or exchanged. When a beamtime is over, the experimental set-up is disassembled to clear the beamline for the next user, and is stored in the laboratory.

Table 3.1 summarises the beamtimes I participated in during the course of my PhD. Data presented in this thesis were exclusively recorded in the single bunch (SB) beamtimes using magnetic bottle spectrometers, and are marked in bold.

date	beamline operation mode	method topic	collaborators
13/08-26/08/2007	UE112 low E MB	SES gas clusters	UU
25/02-09/03/2008	UE52 SGM MB	MS, ion-TOF water clusters	-
14/04-27/04/2008	UE112 low E <b>SB</b>	<b>magn. bottle</b> gas & water clusters	FHI
20/10-02/11/2008	UE52 SGM MB	SES + e-TOF small molecules	FU
24/11-07/12/2008	UE112 low E <b>SB</b>	<b>magn. bottle</b> gas & water clusters	FHI
31/08-20/09/2009	UE52 SGM MB	SES + e-TOF small molecules	FU
19/10-01/11/2009	TGM4 <b>SB</b>	<b>magn. bottle</b> gas clusters	-
01/02-21/02/2010	UE112 MB	SES gas clusters	UU
12/04-02/05/2010	TGM4 <b>SB</b>	<b>magn. bottle</b> gas & water clusters	MBI + UH

Table 3.1: Overview of beamtimes at BESSY II. MB - multi bunch, SB - single bunch operation mode; SES - Scienta hemispherical electron analyser, MS - mass spectrometer, TOF - time-of-flight spectrometer ; UU - group of O. Björneholm (University of Uppsala, Sweden), FHI - group of U. Becker (Fritz-Haber-Institut, Berlin, Germany), FU - group of R. Püttner (Freie Universität Berlin, Germany), MBI - group of C. P. Schulz (Max-Born-Institut, Berlin, Germany), UH - group of L. S. Cederbaum (University of Heidelberg, Germany).

# Chapter 4

## rare gas clusters

Clusters generated from pure rare gases or mixtures thereof constitute ideal model systems to investigate the process of interatomic Coulombic decay. They are relatively easy to handle which allows to alter parameters of the system, such as cluster size or composition, and observe the change in behaviour of the decay process. Once we have understood this, we can continue to more complex systems such as water and further to biologically relevant species, e. g. DNA base pairs dissolved in water.

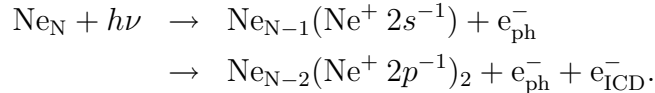
In the next chapter, the results obtained from coincidence experiments on pure neon clusters will be presented. They will be followed by the new findings on the heterogeneous systems of neon-krypton and argon-xenon. All of the coincidence data discussed here were recorded at the TGM4 beamline of the BESSY II synchrotron radiation source by using the new magnetic bottle spectrometer and vacuum set-up that is described in chapter 3.2.3.

### 4.1 neon clusters

Interatomic Coulombic decay has been observed for the first time in experiments on neon clusters [50]. Since then, neon clusters and their dynamics after valence photoionisation have been investigated extensively [62, 102, 103]. In particular for neon dimers, comprehensive experimental and theoretical studies exist, discussing the different relaxation channels and electron configurations during intermolecular Coulombic decay [56, 63, 72, 104–106]. However, so far, experiments on ICD in larger neon clusters were mainly performed with conventional photoelectron spectrometers [50, 62, 107]. As discussed in chapter 3, they suffer from a reduced transmission in the low kinetic energy range, and the identification of spectral features due to secondary processes, such as ICD, is only possible in an indirect

manner. Therefore, we have decided to use the magnetic bottle spectrometer to perform first coincidence experiments on large neon clusters. The IC decay rate of excited neon clusters, being in the range of 10 fs, is predicted to depend on the size of the clusters [53], which motivated us to focus on the size dependence of ICD.

By using the gas cluster source described in chapter 3.2.5, neon clusters were generated in a supersonic expansion of neon gas into the vacuum of the expansion chamber. The conical nozzle (opening diameter 50  $\mu\text{m}$ ) was cooled with liquid helium to temperatures between 48 and 54 K. In combination with stagnation pressures of the gas behind the nozzle of 0.85 and 2.1 bar, respectively, jets of different cluster size distributions could be produced. The mean cluster size  $\langle N \rangle$  was determined from the expansion parameters by using the empirical relation (‘scaling law’) for large clusters by Hagena [18] as given in equation 2.1.1 and the corresponding version for medium-sized clusters (equation 2.1.2) as modified by Buck and Krohne [19]. In the measurements presented here, clusters of three different mean sizes  $\langle N \rangle$  were investigated: 630, 61 and 45 atoms. To proceed from the expansion chamber to the main chamber, the clusters had to pass the skimmer (1 mm open diameter). In the interaction region of the spectrometer, they were irradiated with synchrotron light of 51.8 eV photon energy. This allowed for ionisation of the inner and outer valence levels of neon,  $2s$  and  $2p$ . The corresponding atomic ionisation potentials are 48.475 eV [57, 58] and 21.59 eV (statistical mean value of 21.56 and 21.66 eV [57]). The lowest double ionisation potential for an isolated neon atom is 61 eV [53], which means that an inner valence excited neon atom cannot decay by electron emission. If, however, other neon atoms are in the vicinity, as is the case in a cluster, electronic decay to additionally existing two-site holes can take place. The ICD relaxation pathway is known to be



From this we expect to observe coincidences between photoelectrons and ICD electrons as well as from ionisation by electron collision in our measurements. In a cluster, the ionisation potentials are lowered compared to the atomic values due to polarisation screening. For neon clusters of  $\langle N \rangle = 100$  the  $2s$  ionisation potential has been determined as approx. 48.1 eV [62]. Therefore, the ICD electrons will not possess kinetic energies of 0.66 eV as mentioned in chapter 2.3, but rather of 1 eV or above. This was confirmed in earlier studies performed in our group, where a value of 1.2 eV was obtained from high resolution photoelectron spectroscopy experiments [50] and 1.3 eV from coincidence experiments using another set-up [87]. In order to increase the possibility for these slow electrons to enter the spectrometer, an attracting potential was applied to aperture and drifttube of the spectrometer. A potential of +10 V was applied to the magnet while the mesh

in front of it was kept grounded to prevent electrons emitted from the magnet penetrating into the interaction region. The electron signals were recorded and the data processed as described in chapter 3.3. For the time-to-energy conversion a scan of neon inner and outer valence photoionisation spectra was recorded and the peak positions were analysed.

Figure 3.11 shows a time-of-flight plot of the two-electron-events which were recorded for large neon clusters in two subsequent measuring cycles. The coincidence map obtained after transformation from flight time to kinetic energy is shown in figure 4.1. In the two-dimensional plot at the lower right, the number of coincident electron pairs for each combination of kinetic energies ( $e_1, e_2$ ) is shown in a colour coded format (see corresponding intensity scale at top left). The main feature, a high intensity peak at an  $e_1$  energy of 3.1 eV and an  $e_2$  energy between 1.0 and 1.8 eV, is highlighted by the two red bars. This feature represents electron pairs, of which one electron ( $e_1$ ) is a photoelectron emitted from the Ne 2s energy level and the other one ( $e_2$ ) is a low kinetic energy electron. Due to the configuration of the acquisition electronics in our experimental setup it was not possible to record electrons with a time-of-flight difference lower than 86 ns. Therefore, the colour coded maps of the figures 4.1 and 4.3 end slightly before the main diagonal. This means that the ICD peak actually could extend further towards larger kinetic energies, without being detectable for us. Even though, measurements performed at a slightly different excitation energy (51.2 eV) do not suggest a shift of the kinetic energy of the slow electron  $e_2$ . In agreement with earlier experiments [50, 104, 107] and theory [56], these electron pairs are therefore identified as photoionisation of a neon cluster into a  $2s^{-1}$  vacancy state that decays further by ICD. To obtain the energy spectrum of the ICD electron, the intensity of coincident electron pairs with an  $e_1$  electron in the kinetic energy range of the 2s photoline (marked by the two red bars) was summed up along the  $e_1$  axis. The resulting spectrum is shown in the top right panel. What becomes obvious, both here and in the two dimensional plot, is that the energy distribution of the ICD electrons does not extend down to zero eV. Information about the intermediate state can be gathered by performing the summation of electron pairs along the  $e_2$  axis for each  $e_1$  energy. This results in the red trace given in the left bottom panel, referring to the  $e_1$  kinetic energy axis on the right hand side of the map. In this diagram, the cluster related 2s photoline can be seen at about 3.7 eV of kinetic energy. Unfortunately, the bulk-to-surface splitting of the photoline of approx. 200 meV [62] could not be resolved by our spectrometer. An atomic 2s feature resulting from uncondensed sample gas is seen in non-coincident spectra from the same experiment (not shown here), but does not show up in the figure since it does not lead to emission of a second electron. Apart from the ICD peak the map contains another prominent feature, namely a relatively broad line along a diagonal that corresponds to a sum of electron kinetic energies ( $e_1 + e_2$ ) of about 8.5 eV. This can be understood as a process in which an initially emit-



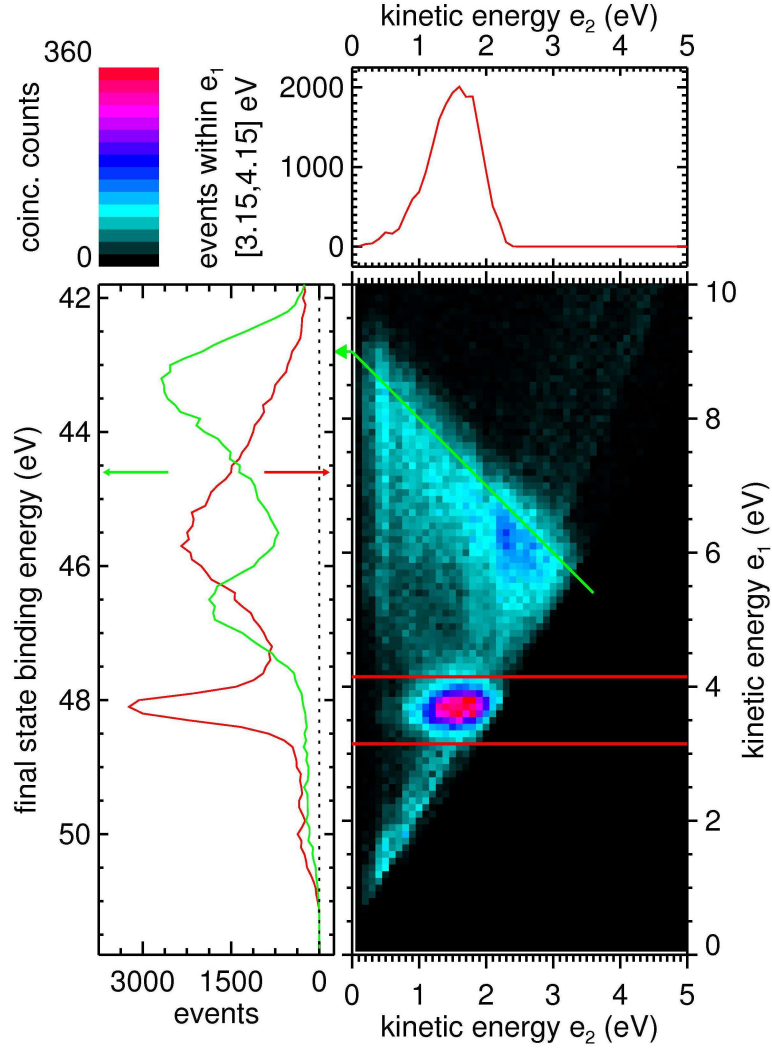


Figure 4.1: Plot of coincident electrons generated in neon clusters of mean size  $\langle N \rangle = 630$ , recorded at a photon energy of 51.8 eV. The ICD feature is highlighted by the two red lines, its energy spectrum is shown in the top panel. The diagonal feature is attributed to elastic scattering within the cluster. The red spectrum on the left hand side reflects the intermediate states whereas the green one presents the number of coincident events versus final state binding energy (see text for details).

ted  $2p$  photoelectron ionises a  $2p$  electron from another monomer of the same cluster by electron collision. In this so-called intra-cluster inelastic scattering, the two electrons share the available excess energy in a continuous way, which leads to the appearance of a relatively homogeneous diagonal line as seen in the spectrum. We can obtain additional insight on both processes by summing up the coincident intensity along the lines of constant total electron kinetic energy, as indicated by the green arrow. The resulting spectrum is given by the green

curve in the left bottom panel. It represents the number of coincident electron pairs versus (two-hole) final state binding energy. Analogous to a non-coincident electron spectrum, the energy of the final state results from the photon energy reduced by the sum of electron kinetic energies.

A zoom into the coincidence plot of figure 4.1 is given in figure 4.2. Though much weaker, a feature similar to the main ICD peak can be found at slightly lower  $e_1$  energies (1.8 eV) and at  $e_2$  energies of around 0.8 eV. In this case, the  $e_1$  energy corresponds to a Ne  $2p$  satellite state ( $(^3P)3s(^2P_{3/2} \& \frac{1}{2})$ ) with a binding energy of approx. 49.4 eV [26, 108]. One could speculate to see another small peak between the  $2s$  photoline and the first satellite, being another satellite-ICD peak. The photoelectron energy of ca. 2.3 eV matches roughly with the satellite energy of 48.8 eV ( $(^3P)3s(^4P_{3/2} \& \frac{1}{2})$ ); the corresponding ICD energy is around 0.9 eV. A spectrum representative for the intermediate state, obtained by integrating over all slow electrons  $e_2$ , is shown in the left panel. The spectrum exhibits local maxima at 1.8 and 2.3 eV. Their difference to neighbouring data points is larger than the statistical error of the measured number of coincident electron pairs would allow.

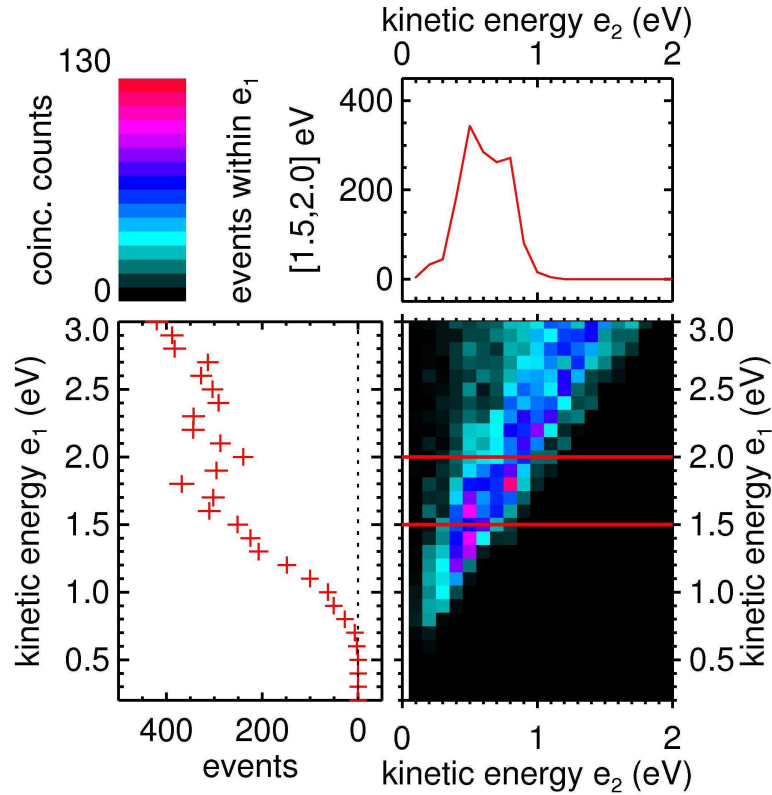


Figure 4.2: Detail of the coincidence plot given in figure 4.1.

The results obtained from investigating the smaller cluster sizes,  $\langle N \rangle = 61$  and

45, are shown in figure 4.3. Analogous to the plot for the larger cluster size, the ICD peak is the prominent feature in the maps. It is highlighted by the two red bars and the ICD energy spectrum obtained from a summation of the marked regions of interest is given in the top panels. For these two spectra as well, one could argue to see small islands of increased intensity at  $e_1$  kinetic energies of 1.8 and 2.3 eV, similar to those in figure 4.2. The analysis showed that also here, statistical errors of the intensity of the intermediate state spectra (red curves) are less than the differences between neighbouring data points.

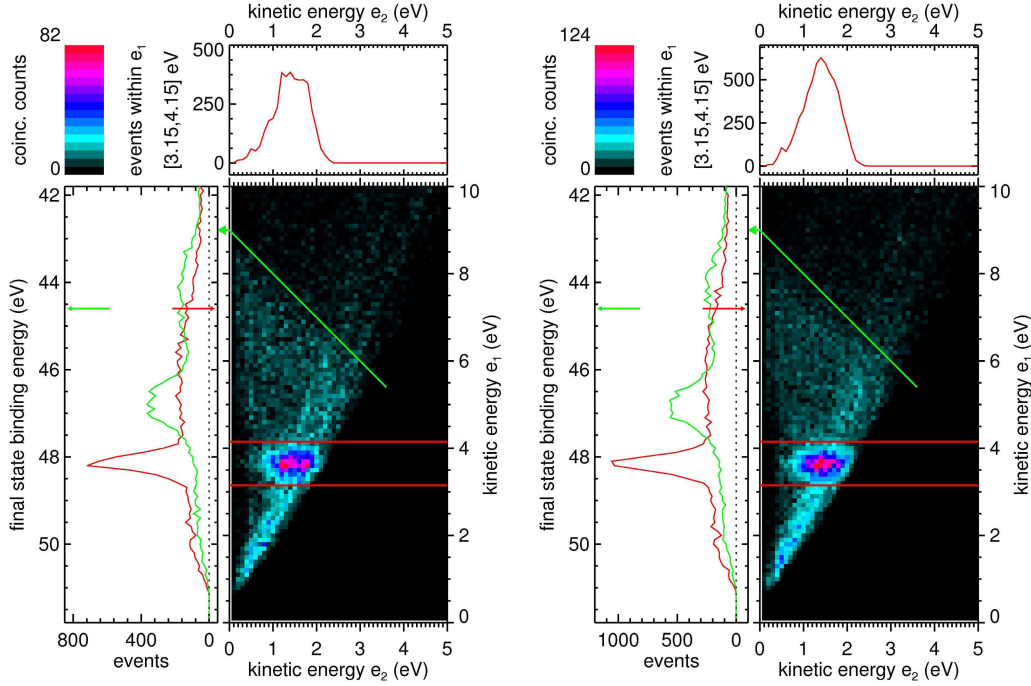


Figure 4.3: Plots of coincident electrons from neon clusters of mean size  $\langle N \rangle = 61$  (left) and 45 (right), recorded at a photon energy of 51.8 eV. For more details see figure 4.1 and text.

Throughout all spectra, we observe that photoelectrons emerging from clusters possess kinetic energies slightly higher than those being emitted from a monomer. The larger the cluster, the more efficiently the site of ionisation is shielded by surrounding atoms. This means the photoelectron has to overcome a lowered Coulombic field which results in a higher electron kinetic energy. Interestingly, this is true even for ICD electrons as can be inferred from figure 4.4. Here, the energy spectra of ICD from the above figures (4.1 and 4.3) are shown in one plot. For easier comparison, they are normalized to the same peak intensity. The two vertical lines in figure 4.4 mark the position of the centers of gravity of the peaks. One observes a slight energy shift of 0.1 eV to lower energies on decreasing the cluster size. It should be noted that the shift could actually be slightly larger since

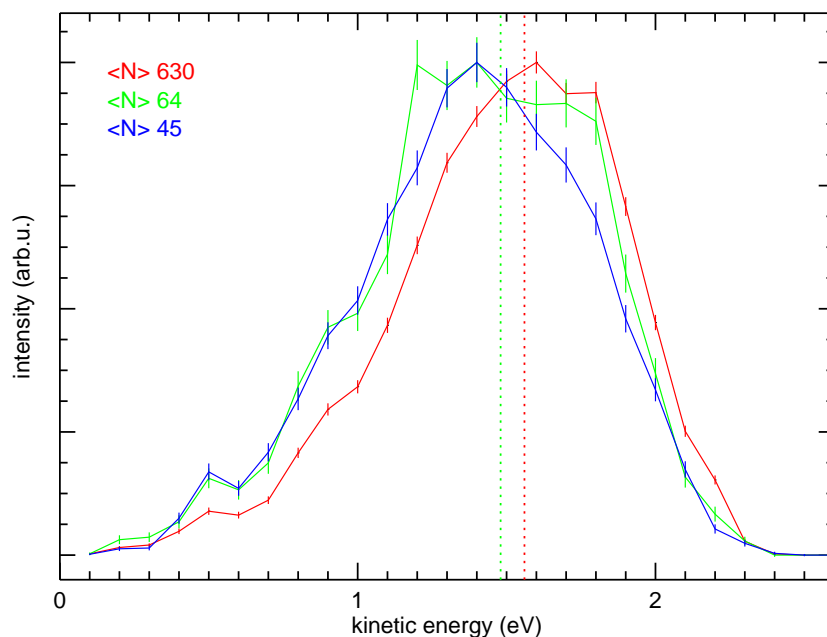


Figure 4.4: ICD energy spectra of neon clusters of different sizes as given in figures 4.1 and 4.3.

the ICD of larger clusters is assumed to extend further towards higher energies, as discussed above. But clearly, even for the smallest cluster size investigated, the peak does not extend until zero eV. This is a remarkable difference to the results obtained for neon dimers in a previous experiment (compare figure 4.4 to figure 3b of [63]).

In experiments performed earlier in our group, the efficiency of IC decay in neon clusters was determined to be 100 % [107]. For the studies using the new spectrometer, though, a quantitative statement regarding the efficiency cannot be made since the transmission function is not known for the settings used in these measurements. Nevertheless, since the same photon energy was used for all three measurements, and since the kinetic energies of the photoelectrons and ICD electrons vary only slightly, the transmission should not change within these ranges. This allowed for a qualitative analysis, and a nearly constant efficiency for all cluster sizes investigated was found (slightly falling for smaller clusters).

When comparing the coincidence plot given in figure 4.1 to the ones in figure 4.3, it becomes obvious that the size of the clusters influences not only the electron kinetic energies but also to which extent competing processes, such as scattering, take place. For the larger clusters (figure 4.1) the diagonal is very prominent and, as mentioned above, is centred around a sum of electron kinetic energies of 8.5 eV. For the smaller clusters (figure 4.3) the feature becomes much weaker. Although the values are not transmission-corrected, the ratio of electron pairs

that experienced scattering to the ones that participated in an ICD process seems to decrease significantly when going from large to small clusters. This could be explained by imagining that in a smaller cluster the photoelectrons emitted towards the centre of the cluster do not have to pass as many layers of atoms as in the case of a larger cluster, which reduces the possibility of scattering enormously. Furthermore, the scattering feature shifts to slightly lower energies (8.15 eV) for the smaller clusters. A possible reason is the lower average distance between the two vacancies created by photoionisation followed by intracluster scattering in smaller clusters. This leads to a higher Coulomb repulsion energy in the final state. The fact that we see an energy shift of the scattering diagonal between larger and smaller clusters also allows to discard inter-cluster inelastic scattering as an alternative explanation for the diagonal feature [109]. If the two electrons were produced from different clusters, the final state spectrum would be independent of cluster size. In addition, scattering processes which involved more than two electrons might have taken place as well. Our analysis procedure is sensitive only to two-electron processes. Therefore, we will either not recognise them or, in cases where only two of the three participating electrons were detected, they do not accumulate to a feature as, for example, a diagonal, but will distribute over a larger area which lies below the two-electron diagonal.

Summarising, the use of the electron-electron coincidence technique for investigating ICD in neon clusters proved valuable. It allowed to distinguish between different competing processes subsequent to the initial photoionisation, such as ICD and ionisation by electron collision. In the studies presented here on neon clusters of different mean size, it could be confirmed that the maximum of the ICD kinetic energy distribution shifts towards higher kinetic energies for larger clusters. This is consistent with theoretical expectations [110] and the experimental observation that the energy of an ICD electron emitted from a neon dimer is close to zero eV [63]. The probability of ICD to take place once the Ne  $2s$  level is ionised seems rather insensitive to the cluster size. In contrast to that, the scattering contribution, where the outgoing photoelectron ionises another electron by collision, increases significantly for increasing cluster sizes. This is in accordance with earlier coincidence experiments on neon clusters performed in our group by using a different set-up [87]. Finally, evidence for the occurrence of ICD from Ne  $2p$  satellite states has been found, but needs to be corroborated by further investigations.

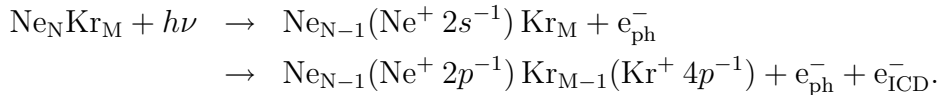
## 4.2 neon-krypton clusters

As an example system to study mixed rare gas clusters, the combination of neon and krypton was chosen. Neon-krypton clusters present an interesting system due to the fact that the ICD electron is expected to be of unusual high energy. The

dependence of ICD on the cluster size, the cluster composition, and the photon energy was investigated.

The mixed clusters were produced by coexpanding a pre-mixed gas mixture, containing mainly neon and a variable amount (2-5 %) of krypton, through a conical and cooled nozzle (opening diameter 100  $\mu\text{m}$ , half opening angle  $15^\circ$ ) into the vacuum. The cluster beam had to pass a conical skimmer (opening diameter 1 mm) before being crossed with the synchrotron radiation. Along the interaction region an electric field was generated by applying -2.5 V at the aperture and drifttube of the magnetic bottle spectrometer, and +2.5 V at the mesh in front of the magnet. This slows down the electrons before entering the drifttube, thus increasing the energy resolution. The magnet itself was kept at +10.0 V to prevent secondary electrons emerging from its surface to penetrate into the interaction region.

The clusters were irradiated with photon energies of 55, 105 and 110 eV for the photon energy dependent study. This leads to the emission of a Ne 2s electron ( $E_{\text{bind,atom}}(\text{Ne } 2s) = 48.475 \text{ eV}$ , [57, 58]), which leaves the cluster in an excited state. The relaxation of an outer-valence electron from the same neon atom ( $E_{\text{bind,atom}}(\text{Ne } 2p_{1/2}^1) = 21.66 \text{ eV}$ ,  $E_{\text{bind,atom}}(\text{Ne } 2p_{3/2}^3) = 21.56 \text{ eV}$ , [57]) releases enough energy to ionise another outer-valence electron. The latter one will preferably be a Kr 4p electron ( $E_{\text{bind,atom}}(\text{Kr } 4p_{1/2}^1) = 14.66 \text{ eV}$ ,  $E_{\text{bind,atom}}(\text{Kr } 4p_{3/2}^3) = 14.00 \text{ eV}$ , [22]) due to the higher cross section compared to Ne 2p. The relaxation pathway could be identified as



Bearing in mind that the actual binding energies vary from the given atomic values due to cluster formation and considering the Coulomb repulsion of approximately 4 eV, one can expect the ICD electron to possess a kinetic energy between 8 and 12 eV. This is larger than for most systems studied so far.

Although the initial gas mixture from which the clusters are produced is prepared with a certain mixing ratio, the final krypton contents in the generated clusters could be different. This is due to the unequal van der Waals interaction between the different atoms, which is reflected, for instance, in the dimer binding energies of the three possible combinations of bonds, Ne-Ne: 3.6 meV, Ne-Kr: 6.1 meV and Kr-Kr: 17.3 meV [111–113]. From this, it is clear that krypton atoms will condense far more easily and already at higher nozzle temperatures than neon atoms. Therefore, neon-krypton clusters generated by coexpansion could be much richer in krypton than the initial gas mixture while neon clustering is disfavoured. Neon-krypton mixed clusters are thus suspected to consist of a krypton core surrounded by neon layer(s), with the size of the core depending mainly on the krypton contents of the gas mixture. This is in accordance with a quantitative

study on the equivalent case of neon-argon clusters that has been performed by Lundwall *et al.* [65].

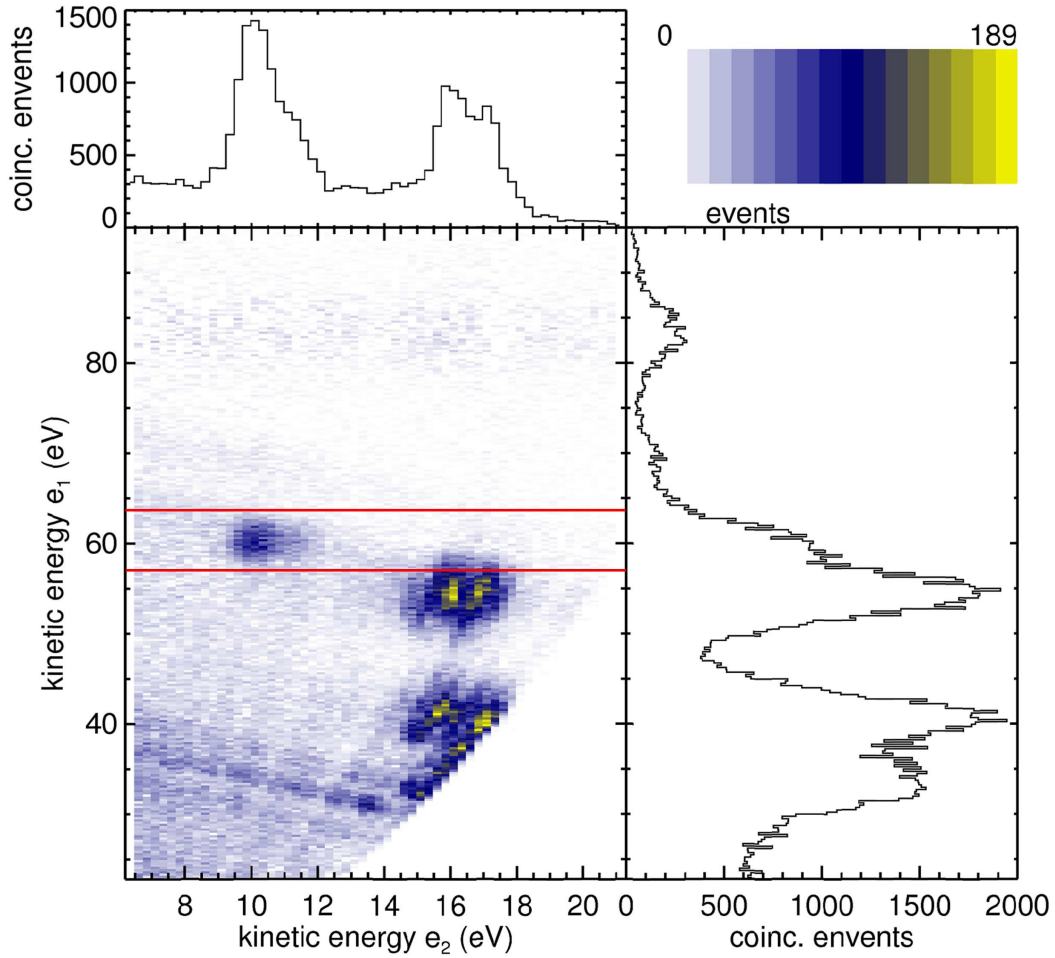


Figure 4.5: Plot of coincident electron pairs emerging from NeKr mixed clusters (5 % Kr) as recorded after photoionisation with 110 eV. The spectrum on the right hand side, showing Auger and photoelectron lines, is obtained by integration over the slow electron  $e_2$ . Summation of the marked region of interest results in the spectrum shown in the top panel. For more details see text.

Coincidence spectra of neon-krypton clusters containing 5 % krypton, recorded at a photon energy  $h\nu=110$  eV, are displayed in the central panel of figure 4.5. Each point in the plot represents an event where two electrons are recorded in coincidence. Of each of these pairs, the fast electron is plotted along the vertical energy axis  $e_1$  and the slow one along the horizontal energy axis  $e_2$ . Depending on the binding energy of the initially produced vacancy this corresponds to either the photoelectron or the electron that is produced by an autoionisation process.

Summing up the intensity for each  $e_1$  energy value along the  $e_2$  axis results in

the spectrum given in the panel on the right hand side. The feature in the  $e_1$  energy range between 30 and 60 eV fits well with the three groups of lines of the Kr  $M_{4,5}NN$  Auger decay [114, 115]. Since the photon energy used was 110 eV, the Ne 2s photoelectron line shows up as a shoulder of the Auger peak at a kinetic energy  $e_1$  of approx. 61.5 eV. In the coincidence map, at this energy, a singular peak can clearly be seen at  $e_2$  kinetic energies between 9 and 12 eV. This peak is identified as the ICD signature of neon-krypton mixed clusters. To determine its spectral shape, the events appearing within the  $e_1$  energy range marked by the two horizontal bars (57 to 64 eV) were integrated. The spectrum obtained such is drawn in the top panel. The maximum of the peak attributed to the ICD electron is at about 10 eV, with a less steep slope on the high kinetic energy side. Due to the electric field applied along the interaction region, only electrons above a certain threshold are able to enter the drifttube and reach the detector. As a consequence, the coincidence map does not show pure neon ICD, which would be energetically possible, but whose feature would be visible at about 1-2 eV (see chapter 4.1), which is below the kinetic energy range displayed. Another prominent feature to be seen in the coincidence map is the falling diagonal that begins at an  $e_1$  energy of 37 eV. This line can be attributed to direct photo double ionisation of neon leading to Ne ( $2p^4$ ) final states with binding energies between 62.5 and 69.4 eV [116]. A characteristic for direct double ionisation is the continuous energy sharing of the available excess energy between the two emitted electrons (see equation 2.2.3), therefore a diagonal of constant total electron kinetic energy arises.

In order to prove the energetic conditions of the ICD feature, the same measurement has been repeated at lower photon energies. Figure 4.6 shows the result for neon-krypton clusters containing 3 % krypton, irradiated with 55 eV photons. For this photon energy the kinetic energy of the Ne 2s peak is only ca. 6.5 eV and hence lower than the 10 eV expected kinetic energy of the ICD electrons. As a consequence, the Ne 2s photoline shows up at the horizontal  $e_2$  energy axis. Therefore, the photoelectron spectrum is obtained by integrating over all  $e_1$  energies and is displayed in the top panel. No krypton Auger peaks are observed as the photon energy was too low for ionisation of the corresponding core level electron. The spectrum of the ICD electron was determined by summing up all coincidence events appearing between 6.8 and 15.4 eV of  $e_2$  kinetic energy. It is drawn in the panel on the right hand side. As seen, its maximum is at about 10 eV and the peak stretches essentially from 9 to 12 eV. In the coincidence map, underlying the intense ICD peak, a broad diagonal feature can be seen. In contrast to the sharp diagonal line in figure 4.5, here the accumulation of coincidence events is caused by inelastic collision: The outgoing photoelectron collides with another monomer of the cluster and ionises one of its electrons. In this case, we suspect a Kr 4s electron ( $E_{bind,atom}(Kr\ 4s) = 27.51$  eV, [22]) to be ionised by the 55 eV photon and to ionise a Kr 4p electron by collision on its way out of the



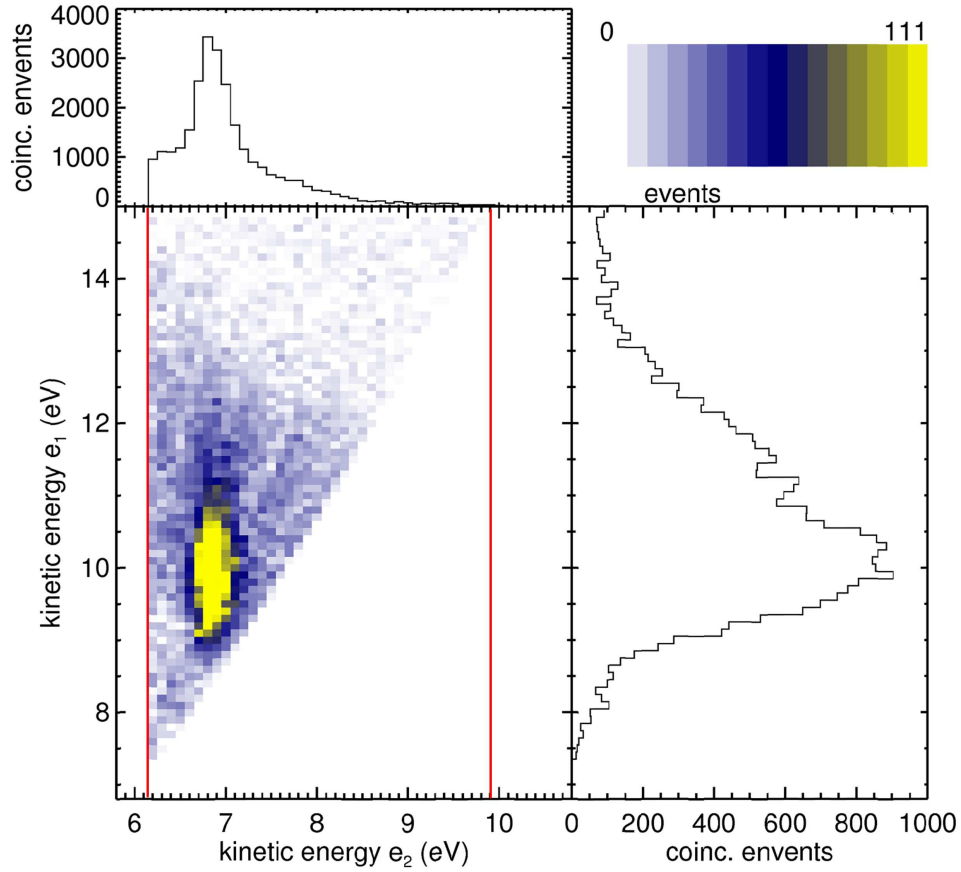


Figure 4.6: Coincidence plot of NeKr clusters (mixing ratio Ne:Kr 97:3) determined at a photon energy of 55 eV. Since now the photoelectrons are slow, their spectrum is obtained by integrating the fast electrons  $e_1$ . It is shown in the top panel. Summation of the marked region of interest, between 6.15 and 9.9 eV, results in the spectrum shown on the right hand side. For more details see text.

cluster. The excess energy of approx. 13 eV can be shared arbitrarily between the two emitted electrons, thus leading to the diagonal.

The same measurement has been repeated at a third photon energy, at 105 eV. In this case the Kr 3*d* photoline overlaps with the ICD electron peak (at about 10 eV) and additionally the Ne 2*s* photoline with the krypton Auger peak (at about 56.5 eV), making it impossible to clearly separate the two coincidence events, (Ne 2*s*, ICD electron) and (Kr 3*d*, Auger electron), from each other. Nevertheless, the peak in question for ICD behaves exactly as expected: On the one hand, the kinetic energy of the responsible photoelectron (Ne 2*s*) shifts according to an increase in photon energy, and on the other hand, the kinetic energy of the second electron stays constant at about 10 eV. This strongly supports the interpretation

that this peak is caused by ICD of neon-krypton mixed clusters.

To find out more about mixed cluster ICD, further experiments with varying cluster size and composition were performed and are discussed in the following.

One part of the experiments focussed on the effects on ICD caused by an increased krypton contents in the gas mixture. To the neon base gas 2, 3 and 5 % of krypton gas were added. Coincident spectra for all three mixing ratios and 2 photon energies, 55 and 110 eV, were recorded. The resulting two sets of ICD spectra are shown in figure 4.7, the spectra for 55 eV on the left (a), for 110 eV on the right (b), and for increasing krypton contents from bottom to top (red triangles: 2 %, blue circles: 3 %, and black squares: 5 %). All traces have been normalised to the same peak intensity. In both sets of plots, an increased krypton content

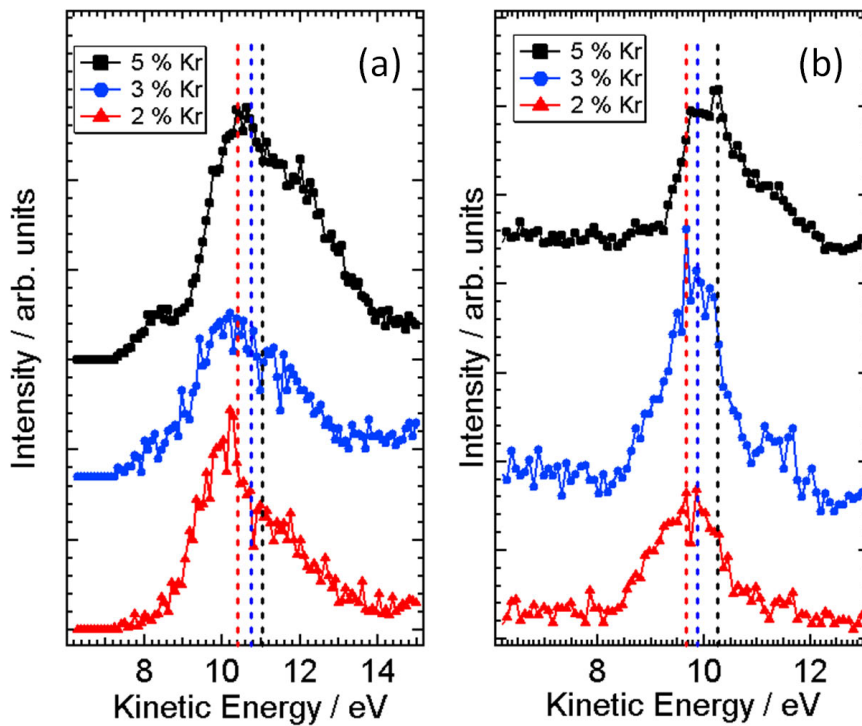


Figure 4.7: ICD spectra for mixed NeKr clusters of variable mixing ratio recorded at photon energies of 55 (a) and 110 eV (b).

leads to a shift of the ICD spectra toward higher kinetic energies. The energy of the center of gravity increases from 10.4 to 10.7 and 11.1 eV for the case of 55 eV photon energy and from 9.7 to 9.8 and 10.2 eV for the 110 eV spectra and is indicated by the vertical lines in the figure to guide the eye. An explanation for this behaviour can be offered by an increase of the cluster size for higher krypton concentrations in the mixture. It is known that with increasing size the cluster

becomes more polarisable [117]. Therefore, the effect of polarisation screening ([118] and chapter 2.2), which causes a lowering of the initial and final state binding energies relative to the atomic position, is more prominent the larger the cluster is. Since the polarisation screening contributes twice for the doubly charged final state, its effect on lowering the state's binding energy is even larger here. This means that the ICD electron will possess a higher kinetic energy if it is generated in a larger cluster [110]. Examining the spectra more carefully, it can be recognised that the ICD peak develops a shoulder at the high kinetic energy side when enriching the gas mixtures with krypton. This gives a hint that there are different contributions of the mixed clusters to the obtained ICD peak. Sticking to the picture of a krypton core surrounded by neon layers, as suggested in a similar study on argon-krypton clusters performed by Lundwall *et al.* [117], two cases are possible: Mixtures that are poor in krypton will develop into clusters that are characterised by a small krypton core which is surrounded by closed layers of neon. Or, resulting from an increased krypton concentration in the gas mixture, the krypton core is large and the covering neon layer is thinner. In the first case, the neon atoms will have mainly neon as next neighbours and only some of them will have krypton atoms close by. Only the latter ones will be able, out of energetic reasons, to undergo ICD. In the case of a large krypton core, neon atoms of the interface will show an increased number of next neighbours that are krypton. Since krypton is more polarisable than neon, this leads to a lowering of the final state energy, thus to an increased transition energy and finally to a higher kinetic energy of the ICD electron. As can be seen in the spectra, the 'main peak' appears to be independent of the krypton concentration, wherefore it is concluded that it arises from ICD involving neon atoms that form a rather compact layer around a krypton core [66].

Spectra recorded at different expansion conditions are shown in figure 4.8. On the left hand side, spectra recorded for clusters containing 3 % krypton are shown, on the right hand side for 5 %; the two panels at the top were measured at a photon energy of 55 eV, and the two bottom panels at 110 eV. The size of the clusters was increased systematically by increasing the stagnation pressure behind the nozzle or decreasing the nozzle temperature. The corresponding spectra are plotted from bottom to top, ordered by increasing cluster size. All spectra show the ICD peak at a kinetic energy of approx. 10 eV. Additionally, spectra recorded for the clusters containing 5 % krypton exhibit a stronger shoulder than the ones for 3 %. One could expect that for increasing cluster size, the size of the krypton core increases. Even if more neon is available, it has to cover a larger krypton core, so that the thickness of the neon layer would not necessarily grow. Due to the increased polarisation screening, one would expect to see the ICD peak shift to higher kinetic energies for larger clusters. At the same time, since the krypton core grows and thus its surface, the shoulder might develop from small to large clusters although the mixing ratio is kept constant. Nevertheless, the changes in

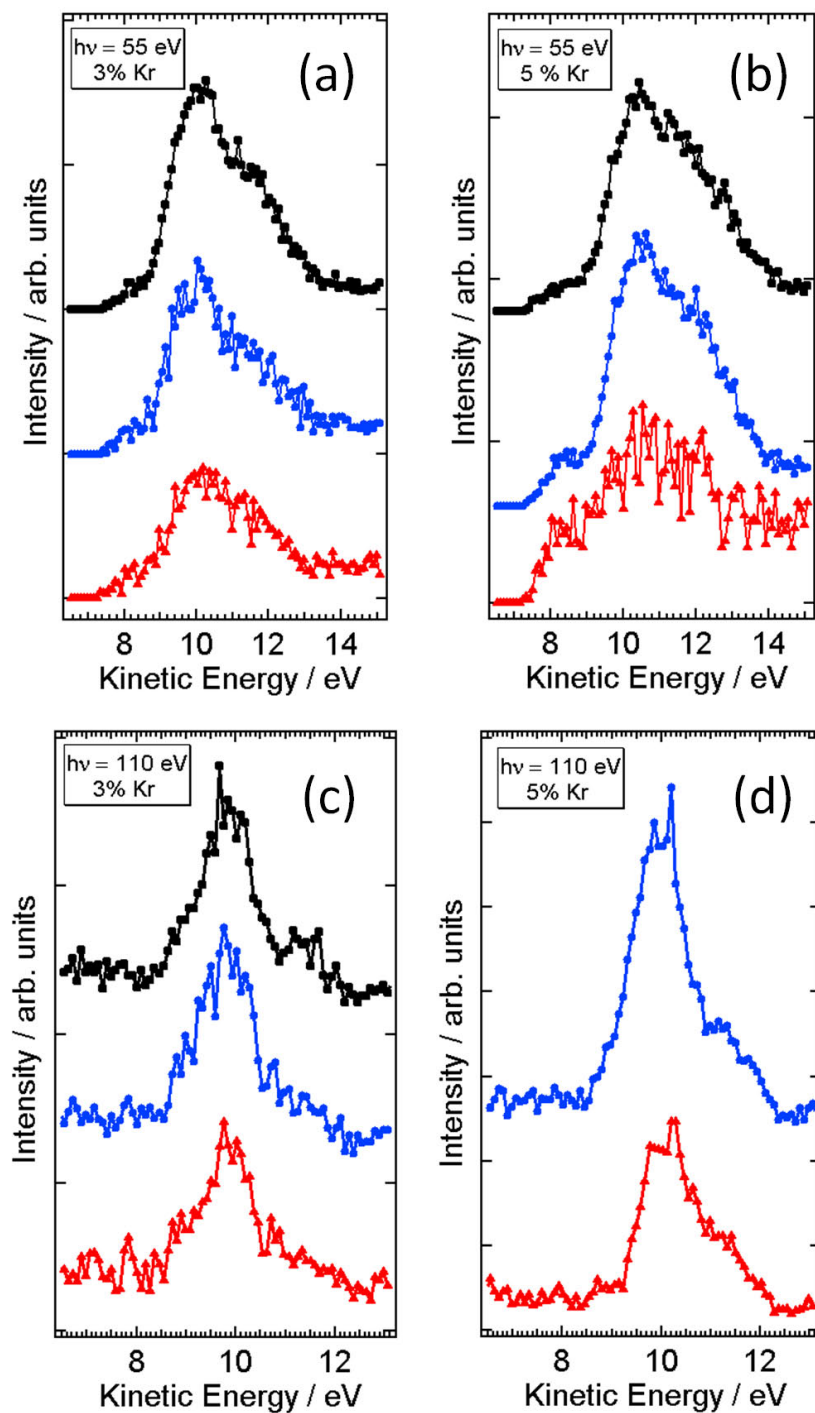


Figure 4.8: Sets of cluster size dependent ICD spectra of NeKr mixed clusters for two photon energies and different mixing ratios: (a) 55 eV, 3 %, (b) 55 eV, 5 %, (c) 110 eV, 3 % and (d) 110 eV, 5 %. The cluster size increases from bottom to top (red triangles, blue circles, black squares).

the ICD peak position as a function of the expansion conditions are not significant and, therefore, the spectra shown in figure 4.8 do not provide clear support for either of the two assumptions. In order to observe the expected behaviour, more investigations on a systematic size increase under otherwise constant and stable experimental conditions have to be performed.

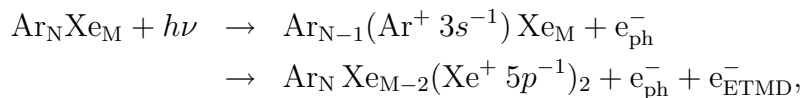
Summarising, it shall be noted that the existence of ICD in NeKr mixed clusters has been shown to appear after Ne  $2s$  photoionisation of the clusters. The kinetic energy of the Ne  $2s$  photoline shifts according to the photon energy used while the energy of the ICD electron remains constant for static experimental conditions. All investigated clusters sizes show an ICD electron that is suspected to emerge from krypton atoms of a core which is surrounded by a closed shell of neon atoms. By increasing the krypton contents of the gas mixture, the ICD peak develops a shoulder at the high kinetic energy side which is attributed to ICD involving neon atoms that have more krypton next neighbours. A cluster size dependent behaviour of the ICD peak could not be observed in our measurements. From this it might be interpreted that the observed ICD feature is characteristic for the interface between the two rare gas layers only and not for the structure of the cluster as a whole [66].

### 4.3 argon-xenon clusters

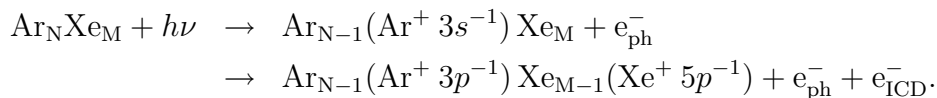
Finally, the system of mixed argon-xenon clusters was investigated. This system is of special interest because the decay channels that are accessible after Ar  $3s$  ionisation depend on the size of the system [119]. Calculations showed, that for an argon-xenon dimer no electronic decay is possible at all after inner valence ionisation due to energetic reasons: The double ionisation potential (DIP) of the argon-xenon dimer is 31.25 eV and lies above the ionisation potential (IP) of Ar  $3s$ . Addition of one more xenon atom changes the situation dramatically. Due to this extra xenon atom, the energetic configuration of the clusters changes such that doubly charged final states can occur even below the Ar  $3s$  ionisation potential. This means that an electronic decay of the trimer system  $\text{ArXe}_2$  is now energetically possible after inner valence ionisation of the argon atom. Moreover, electron transfer mediated decay (ETMD(3), see chapter 2.3) is concluded to be the only possible decay channel of this trimer system, as the only state with a DIP below the IP of Ar  $3s$  is the one where the two positive charges of the final state are located at the two xenon atoms,  $\text{Ar}(\text{Xe}^+ 5p^{-1})(\text{Xe}^+ 5p^{-1})$  [120]. An increased energy difference between the DIP and  $\text{Ar}^+ 3s^{-1}$  suggests that structural changes in the  $\text{ArXe}_2$  trimer have less influence on the accessibility of ETMD(3) than in the case of the similar system  $\text{ArKr}_2$  [119]. This idea is supported by the fact that the DIP of Xe-Xe-ionised final states lies below the Ar  $3s$  IP even for different geometries of the trimer. At the same time, this implies that one cannot extract

information regarding the structure of the trimer by simply detecting the ETMD electron [120].

If the trimer system is now extended to a cluster and xenon atoms appear in the third or even fourth coordination shell around argon, then an interatomic Coulombic decay of Ar  $3s$  ionised states involving these xenon atoms becomes energetically possible. This means that for argon-xenon clusters above a certain cluster size ICD and ETMD would coexist. Due to its higher efficiency, ICD would probably quench the ETMD channel [120]. Therefore, in contrast to argon-krypton mixed clusters, where ETMD(3) was predicted to be the only possible electronic decay channel [119], a competition between ETMD and ICD is expected in the argon-xenon system. The corresponding relaxation pathways can be formulated for the case of ETMD:



and for ICD:



Mixed argon-xenon clusters were produced by coexpanding a gas mixture of argon and xenon through a conical nozzle of 100  $\mu\text{m}$  open diameter. The cluster beam had to pass a conical skimmer (open diameter 1 mm), before being crossed with the synchrotron radiation beam. The emitted electrons were accelerated by applying a potential of +2.2 V on the entrance aperture and drift tube of the magnetic bottle in order to improve the detection efficiency of the very low kinetic energy electrons. To prevent secondary electrons generated on the magnet's surface from penetrating into the interaction region, a potential of +10 V were applied to the magnet while the mesh in front of it was kept grounded.

As a first step to find out whether ETMD and/or ICD are observable in argon-xenon clusters, coincidence spectra at different photon energies were recorded while keeping all other experimental parameters constant. The results of two exemplary measurements, obtained from photoionisation with 32 and 37 eV, respectively, are shown in figures 4.9 and 4.10. In both cases, the original gas mixture contained 5 % xenon. From evaluation of the Ar  $3s$  photolines, a condensation degree of argon of nearly 50 % could be estimated for all plots shown in this chapter, except for the one showing the smallest clusters in figure 4.11 with only about 20 %.

The way the coincidence data are plotted follows the convention used throughout this thesis: the faster electron  $e_1$  along the vertical axis and the slower electron  $e_2$

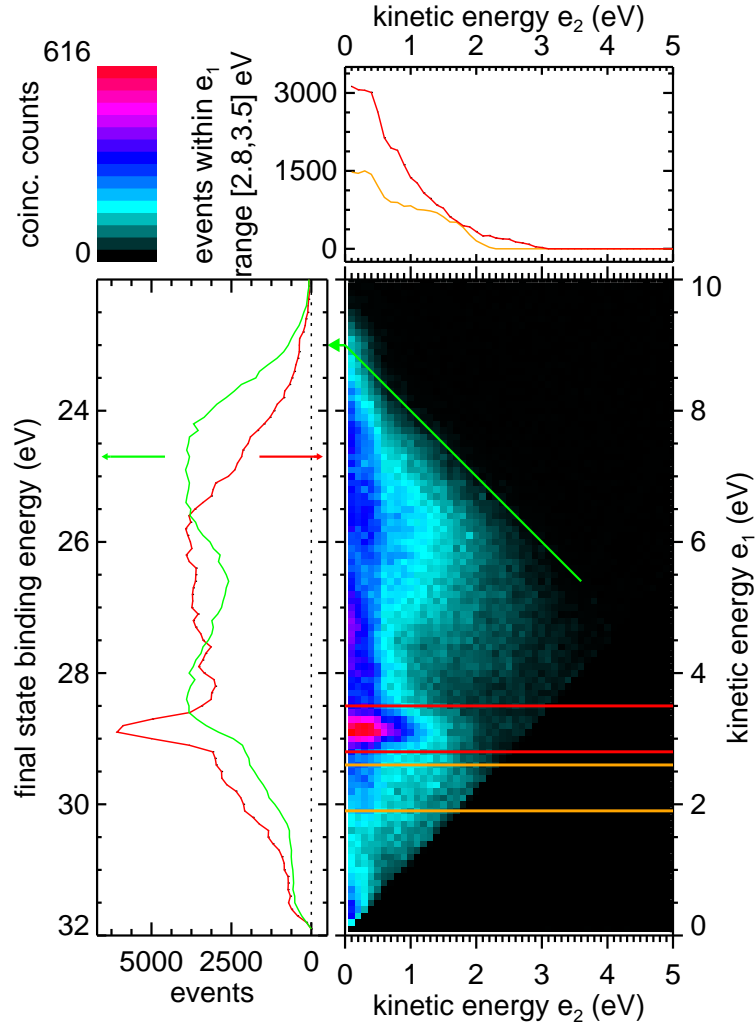


Figure 4.9: Plot of coincident electron pairs emerging from argon-xenon mixed clusters (5 % initial xenon content in the gas mixture) recorded after photoionisation with 32 eV. The photoelectron spectrum on the left hand side (red) is obtained by integration over all energies of the slow electron  $e_2$ . Summation of events belonging to the same final state energy results in the green spectrum on the left to which the left energy scale applies. Integrating the marked regions of interest over the fast electron kinetic energies  $e_1$  leads to the spectra shown in the top panel. For more details see text.

along the horizontal one. The red spectrum to the left is obtained by integrating over all slow electrons. The shown energy distribution of photoelectrons for which a second electron is recorded in coincidence represents the intermediate state of the decay process(es). Atomic photolines are not present in this spectrum since they do not lead to true coincidences and thus are not contained in the map. Additional information can be gained if events of constant sum of electron kinetic energies (as indicated by the green arrow) are added up. This results in

the green spectrum in the left panel, to which the energy scale on the left applies. This spectrum shows the number of coincidence events versus final state binding energy, which is equivalent to a double ionisation spectrum. To my knowledge, so far, no comparable spectra for mixed argon-xenon clusters exist in the literature.

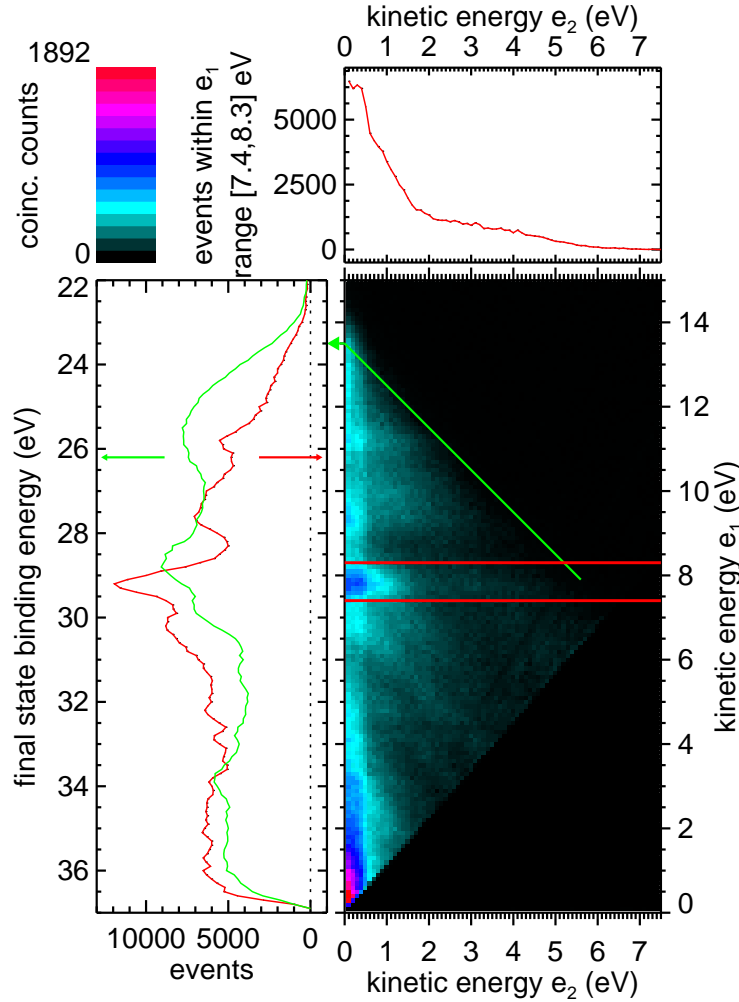


Figure 4.10: Plot of coincident electron pairs emerging from argon-xenon mixed clusters (5 % initial xenon content in the gas mixture) recorded after photoionisation with 37 eV. For more details see figure 4.9 and text.

In the two-dimensional maps of figures 4.9 and 4.10, the energy range in which the Ar 3s cluster photoelectron is expected is marked by the two red bars. Both maps show islands of high intensity within this region of interest. These spectral features confirm that the cluster beam contains mixed clusters of argon and xenon. Moreover, they indicate that the decay of the heterogeneous aggregates subsequent to inner valence ionisation leads to the emission of electrons. As explained above, this is only possible via non-local relaxation mechanisms such



as ETMD and ICD. Integrating the events from the Ar 3s energy range yields the spectra shown in the top panels. In both cases (32 and 37 eV photon energy), the top panel spectra show an intense peak with a maximum at zero eV. The intensity profile then drops, hinting at a step at approx. 0.7 eV, and continues falling toward higher energies, but less steeply. Above 1.5 eV, the signal cannot be clearly distinguished from the background any longer. The orange curve in the upper panel of figure 4.9 was obtained by summing up all events in the coincidence map delimited by the two horizontal orange lines, and is an indication of the background level in the spectrum.

With the knowledge at hand that there is some electronic decay observable in mixed argon-xenon clusters following inner valence ionisation, the focus was shifted on a possible size dependence of the effect. From a gas mixture initially containing 2.5 % xenon, clusters of different sizes were generated by changing the expansion parameters. For the largest clusters presented, the stagnation pressure was 2.12 bar and the nozzle temperature 154.5 K, for the intermediate size 1.5 bar and 158 K were used, and the small ones were obtained by operating the source with 1 bar at 160.5 K. The coincidence plots of this size series recorded at 32 eV photon energy are presented in figure 4.11. Albeit the statistical quality of these three measurements varies considerably, the coincidence plots look essentially the same. All three show the main peak along the argon inner valence line, indicated by the two red bars. An interesting observation, though, is that this peak seems to shift slightly toward lower  $e_1$  energies for smaller clusters. This can be understood by taking the polarisation screening into account, which has been discussed earlier already in chapter 2.2. Integrating over the region of interest marked by the red bars yields the energy spectra given in the right panels. Although the spectra are very similar to each other, a small change in the shoulder of the peak (above 0.7 eV) is observable: it loses in intensity on decreasing the cluster size. In smaller clusters, the lowering of energy levels due to polarisation screening is less strong than in larger ones, wherefore the electrons generated in an autoionisation process possess less kinetic energy. But since this would result in a shift of the whole spectrum to lower energies on decreasing the cluster size, this might not hold as only explanation for the observed intensity decrease of the shoulder relative to the main peak. Instead, this decrease might suggest a second relaxation channel to take place in case of larger clusters. A possible interpretation is that the intensity observed in case of small clusters is solely caused by ETMD. When increasing the cluster size, this would shift to higher energies while the ICD channel would open up, generating electrons in the lower kinetic energy range. Due to the higher efficiency of ICD, the ETMD signal would be quenched [120], resulting in a spectrum that exhibits higher intensity at lower energies.

In order to be able to interpret the other features occurring in the coincidence spectra of mixed argon-xenon clusters, apart from the ETMD/ICD peak, one has to compare these spectra to those recorded for pure clusters of each of the

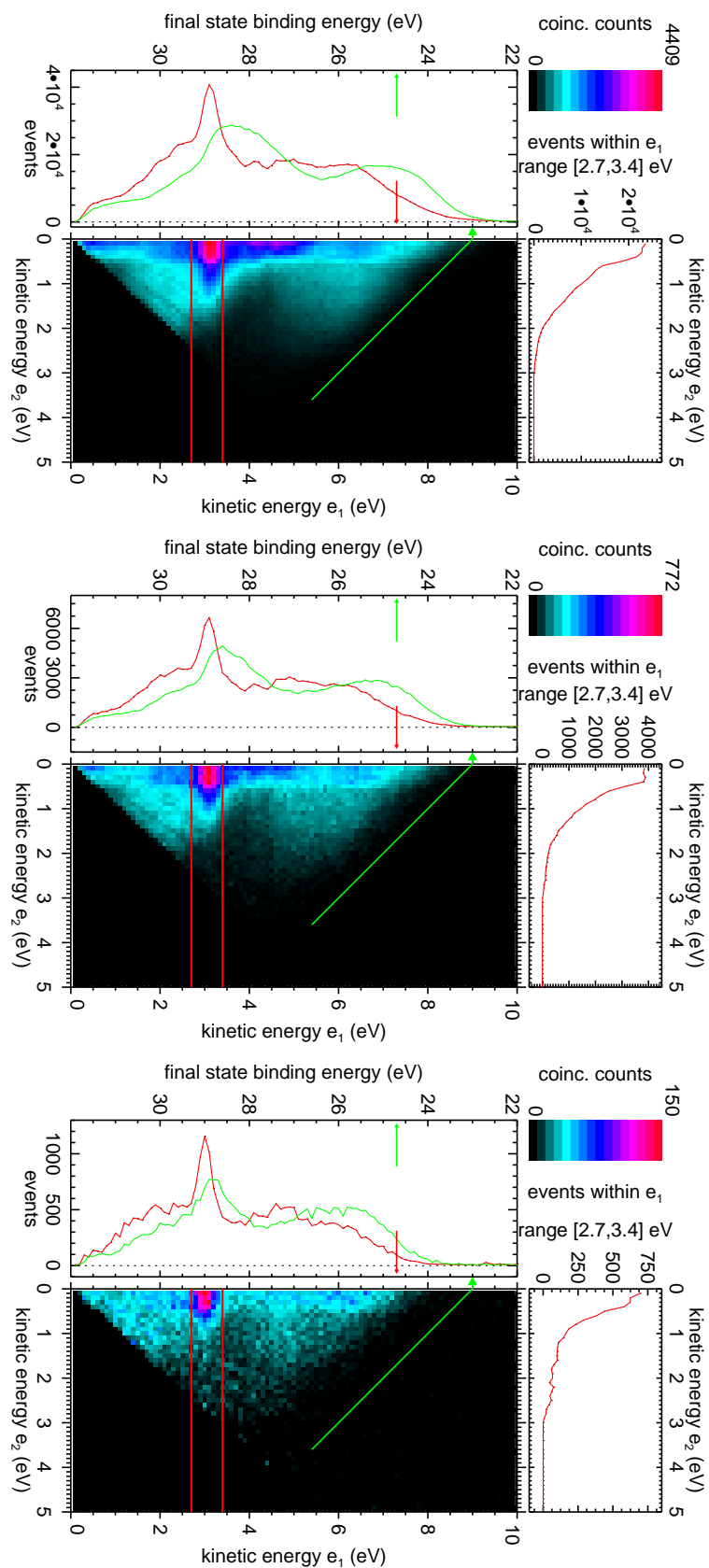


Figure 4.11: Coincidence plots of mixed argon-xenon clusters of decreasing size (from top to bottom) recorded after ionisation with 32 eV.

species. Coincidence spectra recorded for pure argon clusters ( $\langle N \rangle = 6980$ ) and pure xenon clusters ( $\langle N \rangle = 3060$ ) are shown in figure 4.12. For pure argon clusters (left plot), there are no coincidences found along the Ar 3s photoline. This behaves as expected, since pure argon clusters cannot decay via ICD or ETMD after inner valence ionisation. The coincidence map shows no events except for a few counts in the area below (1.7 eV, 0.8 eV). These coincidences might stem from ionisation of two argon outer valence electrons. The coincidence plot obtained from photoionising pure xenon clusters (right plot) instead, shows a broad diagonal along sums of electron kinetic energies ranging from below 6 eV to nearly 10 eV. These events are probably caused by ionisation through electron collision of an outer valence electron with another outer valence electron. The range around

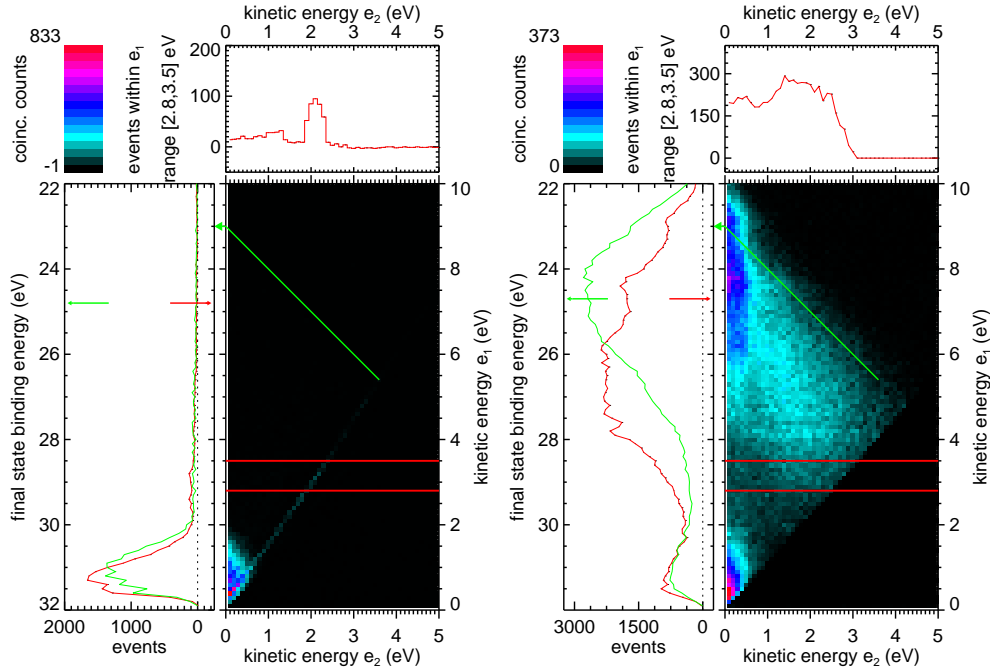


Figure 4.12: Coincidence plots of pure argon (left) and pure xenon clusters (right) recorded after ionisation with 32 eV.

the Ar 3s photoline remains empty for both pure cluster measurements. It can therefore be concluded, that the events observed in this area in all other figures are exclusively caused by mixed argon-xenon clusters and that atoms of both gases participate in the decay. The  $e_1$  kinetic energy of this main feature shifts according to the photon energy. Hence it can be concluded, that this feature is indeed caused by ICD and/or ETMD from mixed argon-xenon clusters.

By using the equilibrium distance between the two atoms of an argon-xenon dimer (4.067 Å [112]), the Coulomb repulsion between argon and xenon can be estimated via equation 2.3.2 as 3.54 eV. This equation corroborated with

equation 2.3.1 should make the energy of the ICD electron assessable. When using these equations, one has to bear in mind that for larger clusters the ionisation potentials of the outer valence electrons (Ar  $3p$  and Xe  $5p$ ) will decrease more than the ionisation potential of Ar  $3s$ . Therefore, it is likely that, in large aggregates, the ICD electron energy will not be negative, which would mean that no ICD electron could escape and measuring ICD would be impossible. Nevertheless, it will probably remain very low, in the 0-2 eV range [121]. Following an equivalent path to equation 2.3.1, one can estimate the energy of an ETMD electron as well: Subtracting the ionisation potential of a Xe  $5p$  electron from the energy difference between Ar  $3s$  and Xe  $5p$  and subtracting the Coulomb repulsion leads to a maximum energy of about 2.6 eV for an ETMD electron. Theoretical calculations determine the minimum energy of an ETMD electron as 1.7 eV for the trimer  $\text{ArXe}_2$  [121], and even higher for larger clusters due to the lowered ionisation potentials.

With these calculations, it can safely be assumed that the clusters investigated were beyond the critical size below which only ETMD would occur. Comparing the energy distributions obtained for the autoionisation electron with the theoretical estimations [121], one could rather argue that mainly ICD has been observed in our experiment. This interpretation would be supported by the fact that ICD, whenever possible, is expected to be much more efficient than ETMD [120], thus dominating the spectra.



# Chapter 5

## water clusters

Water is certainly the most important molecule for life on earth. Although it consists only of three atoms, one oxygen and two hydrogen atoms, it exhibits numerous anomalies (see references in [122]) and is still far from being understood. A main reason for this are the hydrogen bonds that connect different water molecules with each other and which are constantly breaking and reforming [123]. On the way to understanding water, it is helpful to not only investigate isolated molecules in the gas phase or bulk water but also the in-between case of water clusters. Water clusters are agglomerations of a few up to several thousand water molecules. They constitute an important model system since they exhibit properties that go beyond the ones of an isolated water molecule but still are different from those of liquid water. Here, we will focus on one of these properties concerning the electronic dynamics of the system. Similarly to the van der Waals bonds of rare gas clusters, theoreticians proposed that the weak hydrogen bonds present in water clusters and bulk water should allow for a non-local autoionisation process to take place, namely intermolecular Coulombic decay (ICD) [49, 124]. In the water monomer the double ionisation potential (DIP) lies at 34.4 eV [125], above the ionisation potential (IP) of the inner valence level (32.6 eV [126]). For water clusters and liquid water, however, the situation is different, since the two positive charges of a doubly charged final state can distribute over two different monomers (two-site state). Therefore, already for the water dimer, the lowest DIPs have been calculated to be approx. 5 eV below the inner valence IP [127]. In other words, the prerequisite for ICD in pure water clusters, or to be more generally in hydrogen-bonded systems, is fulfilled [49]: the binding energy of the ionised state lies above the double ionisation threshold.

So far ICD in water clusters has escaped experimental observation. This can be understood when relating theoretical estimations and experimental possibilities: For ICD electrons from water, calculations predict a broad and rather unstructured kinetic energy spectrum which peaks at zero eV, shows local maxima at 3

and 5 eV and extends up to 10 eV [127]. This ICD energy spectrum can hardly be distinguished from the contribution of secondary electrons to an energy spectrum recorded with a conventional electron energy analyser, as e. g. the one given in figure 5.1. This spectrum has been obtained from photoionising clusters of mean size 98 with 60 eV photons; it is similar to that for liquid water recorded previously [128]. In the kinetic energy range from 40 to 50 eV, the outer valence bands can be seen; the peak at the low binding energy side (10 – 12 eV) is solely due to electrons emitted from the outer valence levels of water clusters. ICD can take place for the  $2a_1$  inner valence states in the kinetic energy range between 25 and 32 eV, which are mainly derived from O  $2s$  ionisation. Due to the large bandwidth of this line, the contributions from clusters and monomers are inseparable. The expected spectrum of ICD electrons in the low kinetic energy range will be superimposed with that of other secondary electrons of non-negligible intensity.

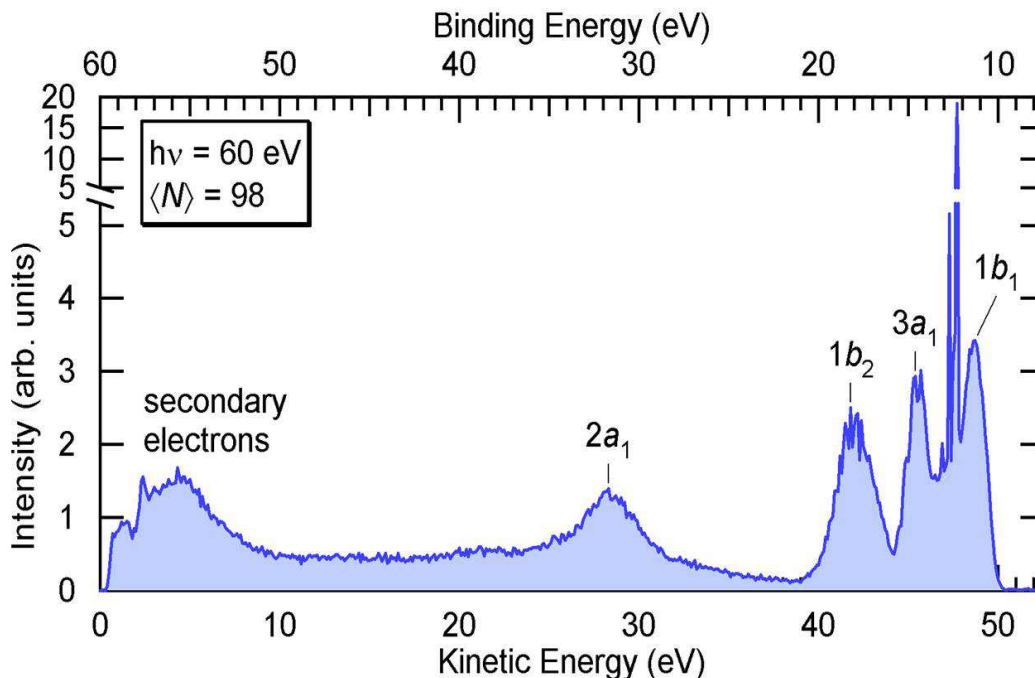


Figure 5.1: Full valence photoelectron spectrum of water clusters of a mean size of 98 molecules. The spectrum was recorded with a hemispherical electron energy analyser after irradiation of the clusters with photons of 60 eV. [25]

Investigating water clusters with a coincidence technique was motivated by the fact that so far, for this system, no experiment succeeded in providing clear evidence for ICD. Therefore, the first beamtime in which we used a magnetic bottle electron spectrometer had two main goals: Firstly, we wanted to find out whether this type of spectrometer is suited to perform the anticipated coincidence experi-

ments, and secondly, we aimed at showing unambiguously that water clusters follow the proposed autoionisation pathway. In order to do so, coincidence spectra of water clusters had to be recorded at different photon energies, so that a change in kinetic energy of the photoelectron could be established. Furthermore, reference spectra of water monomers had to be recorded at otherwise identical experimental settings to ensure that the signal observed does not appear for water monomers. This is a crucial point since ICD is only possible with other monomers in the vicinity of the initially ionised monomer, but not in an isolated one.

In a later beamtime, for which the new set-up was employed, we shifted the focus to deuterated water clusters to address the question whether they behave similar to ‘normal’ water clusters and to what extent the greater deuterium mass influences the dynamics of the system.

## 5.1 ICD in water clusters

The first coincidence experiments on water clusters have been performed using the apparatus described in chapter 3.2.2 and the ‘old’ water cluster source. The clusters were generated by supersonic expansion of water vapour through a conical nozzle of 80  $\mu\text{m}$  diameter. Clusters produced under these conditions are generally called warm since they occupy excited vibrational and rotational states. They are existent in different isomers. The mean sizes of the clusters in our experiment were determined via equation 2.1.4 as  $\langle N \rangle = 40$  and 200, respectively. Such clusters are believed to form amorphous structures, which resemble the hydrogen-bonded network of liquid water rather than that of crystalline ice [129]. After passing a skimmer of 1 mm opening, the cluster jet was crossed with synchrotron light from the undulator beamline UE112 low energy PGMA of BESSY II, which offers variable polarisation of the radiation. For the experiments presented here, the light polarisation was horizontally linear, i. e. within the plane spanned by the photon beam and the central axis of the magnetic bottle spectrometer. The clusters were irradiated with photons of 45, 60 and 80 eV, respectively, which is sufficient to produce inner valence vacancies but does not excite core levels. In order to record even the very low kinetic electrons (down to zero eV), a weak accelerating field (+1.2 V) was applied along the interaction region.

The yield of coincident electron pairs ( $e_1, e_2$ ) from exciting water clusters of mean size  $\langle N \rangle = 40$  with 45 eV photons is shown in the colour-coded map of figure 5.2. In order to remove coincidences arising from the apparatus itself, an equivalent measurement for gaseous helium, recorded at 44.7 eV and scaled with the ratios of the outer valence photoelectron intensities, has been subtracted. By correlating the fast electron energies ( $e_1$ ) with the full valence spectrum given in figure 5.1, we see which parts of the spectrum are characterised by strong emission of low-energy



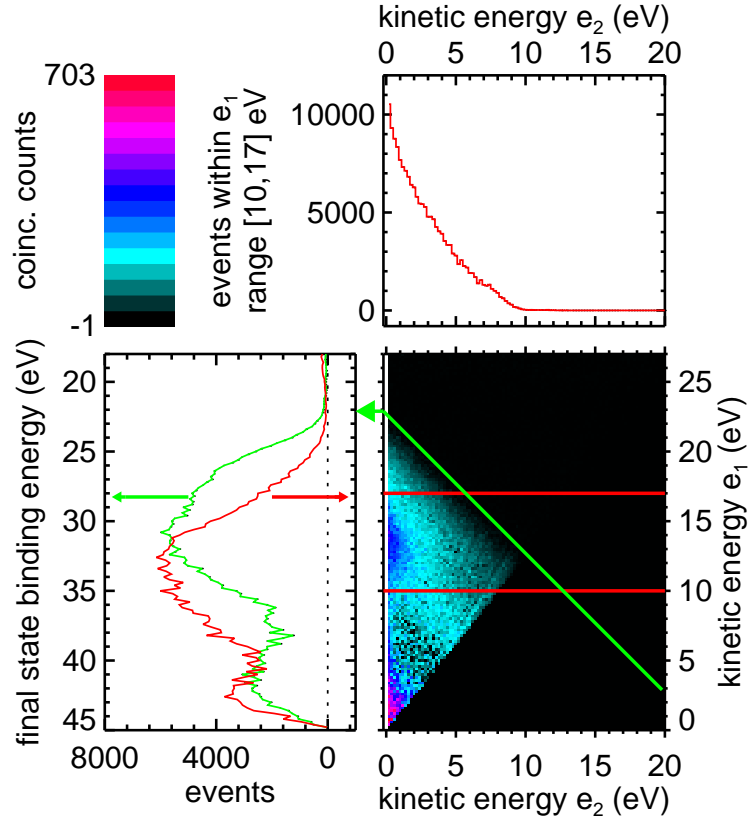


Figure 5.2: Coincidence map of water clusters ( $\langle N \rangle = 40$ ) recorded after photoionisation with 45 eV.

electrons. The most intense feature is marked by the two red lines. Here, the  $e_1$  energies correspond to inner valence ionisation of the water clusters, whereas  $e_2$  energies are below 5 eV. The energy spectrum of the slow electron is obtained by integrating over the fast electron energies  $e_1$  of this range and is shown in the top panel. It consists of a convolution of the singly ionised states with binding energies between 28 and 35 eV [127] and all available two-hole final states. The intensity peaks at zero eV and decreases continuously towards higher kinetic energies. Similar intensity profiles have been found in calculations for water clusters up to the tetramer [127].

The green curve in the left panel is obtained by adding up the coincidence events along diagonals of the same total electron kinetic energy ( $e_1 + e_2$ ). It represents the doubly charged final states which are populated by ICD vs. final two-hole state binding energy. The green arrow marks the minimum final state energy, 22.1 eV, which corresponds to twice the highest occupied molecular orbital ionisation potential of large water clusters [130]. Outer valence single vacancies in numerous combination contribute to the final state spectrum [127]. Since it is not possible to experimentally select certain cluster geometries or specific sizes, the

spectrum is summed over all conformations that are present in the jet. Therefore, a broadened double ionisation spectrum between 23 and 36 eV is observed. These final state energies correspond to the production of two outer valence vacancies, mostly due to ICD. We suggest different processes to contribute to the intensity of the double ionisation spectrum (green curve) observed at higher binding energies: One of them is direct photo double ionisation of uncondensed water molecules which are always present in our cluster jets due to experimental reasons. This can lead to the creation of molecular dicationic states with up to 47 eV binding energy [125].

Another process observable in the coincidence map is intra-cluster electron scattering, which appears as broad falling diagonals. Since this mechanism also leads to two-site final states, it causes a minor contribution to the double ionisation spectrum (green curve). Intensity in the energy region below 5 eV could stem from coincidence events where three particles (or even more) were involved, but only two of them were detected.

The red curve in the left panel is obtained by integrating over all coincidence events for each energy of the fast electron  $e_1$ . It represents the energy distribution of the primary electrons for which a second electron has been recorded.

In order to identify the main feature as ICD, measurements under otherwise identical conditions have been performed for a jet of clusters of mean size  $\langle N \rangle = 200$  and for a beam consisting purely of water monomers. The latter one was produced by leaking water vapour via a needle (inner diameter ca. 250  $\mu\text{m}$ ) from an external reservoir kept at room temperature into the interaction chamber. For the initiating ionisation process, a photon energy of 60 eV was used, which is well above the double ionisation potentials of water monomers and clusters. For molecular water, no ICD feature should be observable since the molecular inner valence hole states do not have sufficient energy to autoionise. Only satellite states of the two hole-one particle type, which in principle could mix with inner valence vacancies, could lead to a similar observation, but they have been found experimentally to be unimportant for molecular water at binding energies above the inner valence ionisation potential [126, 131]. The results obtained from the experiments are shown in figure 5.3. The spectra have been normalised with respect to the accumulation time and the synchrotron radiation intensity. By comparing these two coincidence maps, it becomes obvious that the feature supposed to be the ICD-peak is absent for water monomers. The final state spectrum of water monomers resembles the one for direct photo double ionisation found by Eland [125].

Another important cross-check consists in varying the photon energy used for the initial ionisation process. For the coincidence maps shown in figure 5.4, photon energies of 45, 60 and 80 eV were used. A decrease in photoionisation cross section over this energy range leads to a decreasing intensity of the electron

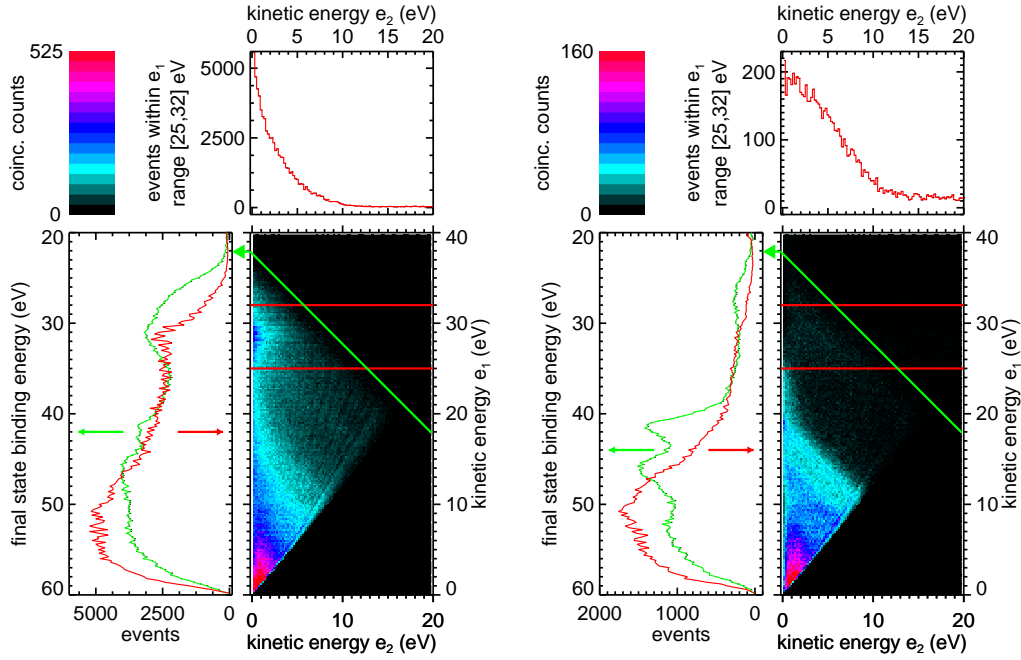


Figure 5.3: Coincidence map of water clusters (left,  $\langle N \rangle = 200$ ) and water monomers (right) recorded after photoionisation with 60 eV.

signal. Therefore, the upper parts of the maps recorded at 60 and 80 eV have been scaled by the factor given in the top right corner in order to improve visibility of the supposedly ICD peak. The  $e_1$  energy of this feature rises linearly with photon energy, from around 14 to 29 and further to 49 eV. At the same time, the energy of the slow electron ( $e_2$ ) remains constant.

From the observed behaviour of the feature in question, we concluded to have unambiguously shown the occurrence of ICD in water clusters. As predicted, the process leads to efficient generation of low-energy electrons which displays in form of a broad, rather unstructured energy spectrum. Parallel to us, Jahnke *et al.* succeeded in discovering ICD from water dimers in another type of coincidence experiment [132].

Experiments [62] and calculations [53, 133] have found ICD to take place on a fs-timescale, and also for water clusters, a transition time in the low fs-range has been suggested [83, 134]. This is even faster than the proton rearrangement associated with ionisation of water [135]. Therefore, ICD is expected to be the dominating relaxation channel, making fluorescence or nuclear rearrangement less important.

It is generally believed that secondary electrons are primarily generated by ionisation of core or valence levels and are subsequently slowed down by (multiple) inelastic scattering events. Here, we have shown that ICD electrons make an

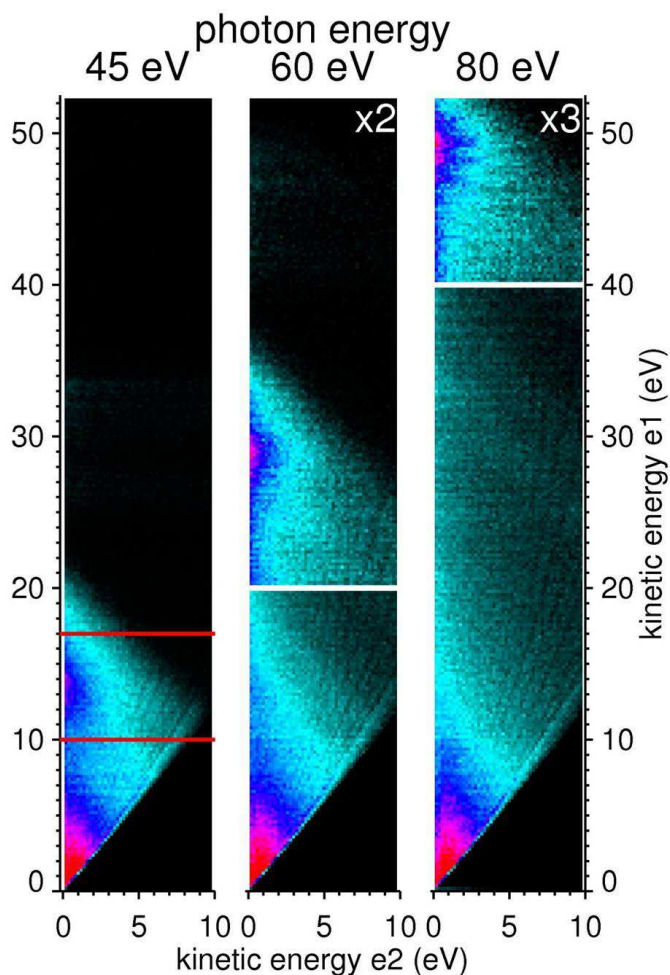


Figure 5.4: Coincidence spectra of water clusters recorded at three different photon energies.

important contribution to the low-kinetic energy spectrum. This suggests to include ICD when considering radiation damage in living tissue since water clusters simulate water molecules in an aqueous environment. Cell damage is primarily induced by double-strand breaks of the involved DNA [136], for which only low doses of ionising radiation are sufficient. A possible mechanism is chemical attack of OH radicals that result from radiolysis of water [136]. Recently, it has been recognised that low-energetic electrons might also present an important mechanism [137, 138], as it was found that they can efficiently induce DNA strand breaks by dissociative attachment [139–141]. Therefore, special attention should be paid to ICD, since it has been found to be a very effective decay channel [107] that immediately leads to the ejection of slow electrons at the site of initial ionisation. Moreover, because ICD is not *a priori* restricted to ionisation of an inner valence electron, but can also be initiated by collision, or be part of a cascade

process following Auger decay [75], the prerequisites for ICD can be fulfilled in different ways, making it an even more relevant process.

## 5.2 clusters from heavy water

Investigating clusters from deuterated water is of vital interest, due to a change of several properties in the bulk phase arising from the increased hydrogen mass. The lower vibrational frequencies increase the strength of the hydrogen bond with respect to ‘normal’ water [122], which allows for explicit studies of the dependence of ICD from a supra-molecular network. Additionally, the stronger hydrogen bonds also imply a better clustering of the molecules.

Analogous to water clusters, the deuterated water clusters have been prepared by heating up the liquid and expanding the generated vapour through a conical nozzle of 80  $\mu\text{m}$  diameter into the vacuum. An accelerating potential of +2.2 V has been applied to aperture and drifttube of the spectrometer to ensure that electrons down to zero eV kinetic energy reach the detector. To prevent secondary electrons emitted from the magnet interfering with the measurement, the magnet was laid onto a potential of +10 V while the mesh in front of it was kept grounded.

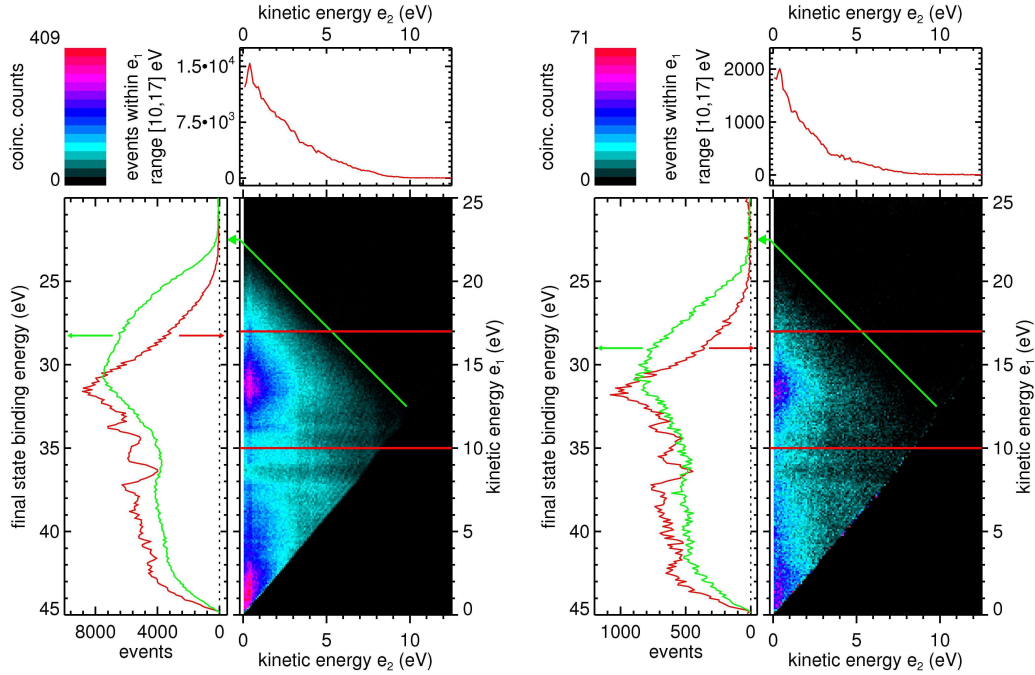


Figure 5.5: Coincidence spectra of deuterated water clusters recorded after photoionisation with 45 eV. The left plot shows results obtained from clusters of mean size  $\langle N \rangle = 135$ , the right one from clusters of mean size  $\langle N \rangle = 42$ .

Coincidence spectra obtained from irradiating deuterated water clusters of different mean size are shown in figure 5.5. Both experiments have been performed under identical conditions except for the cluster source parameters. The data plotted on the left result from a cluster beam of  $\langle N \rangle = 135$ , whereas the data of the right plot stem from a jet of mean size 42. As for the water cluster maps above, the two red bars have been introduced to mark the  $e_1$  energy range corresponding to the inner valence level. For both cluster sizes, a high intensity peak can be found in this area, representing coincidence events from inner valence photoelectrons with very slow electrons. In the top panels, the ICD energy spectra obtained from integrating over the region between the two red bars, is given. Just as one would expect, the intensity does not decrease as steeply for the larger clusters (left) than it does for the smaller ones, and the center of gravity shifts towards higher kinetic energies. Furthermore, the final state spectrum, which is presented by the green curve in the left panels, shows an increased intensity between 23 and 29 eV of final state binding energy and also extends to lower final state binding energies than the spectrum for smaller clusters which is due to the higher kinetic energies of electrons emerging from larger clusters.

In additional measurements, the photon energy dependence of the fast electron  $e_1$  has been cross-checked. Besides, for a beam consisting of deuterated water monomers, no peak that energetically could be ICD was found. This, together with the energetic similarity between water and heavy water, leads us to conclude that ICD takes place in deuterated water clusters as well.

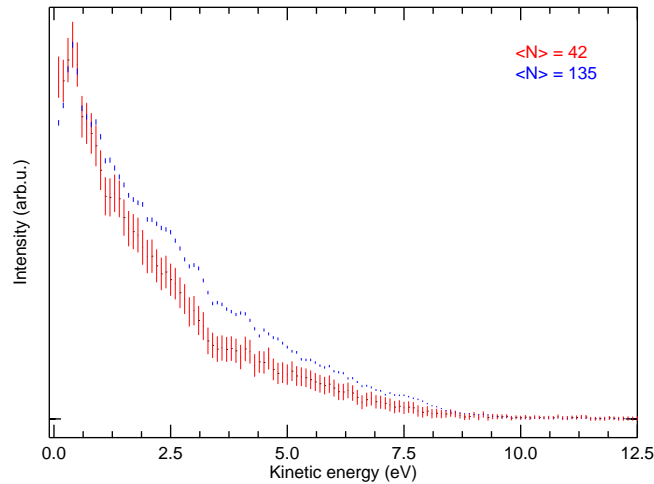


Figure 5.6: Energy spectra of ICD from deuterated water clusters of different mean sizes recorded after photoionisation with 45 eV.

To gain better insight into the size dependence of the autoionisation process, the ICD energy spectra from figure 5.5 have been combined in figure 5.6. Both spectra have been normalised to the same peak intensity for the ease of comparison. The

increase of cluster mean size from 42 (red curve) to 135 (blue curve) does not change the general form of the spectrum, which peaks at approx. 0.4 eV and decreases continuously toward approx. 8 eV. Nevertheless, for the larger clusters, the fraction of electrons possessing higher kinetic energies is larger than for the smaller clusters, which leads to a small shift of the center of gravity of the curves. This is consistent with earlier observations, and can be explained by the increasing energy difference between inner and outer valence levels for increasing cluster size.

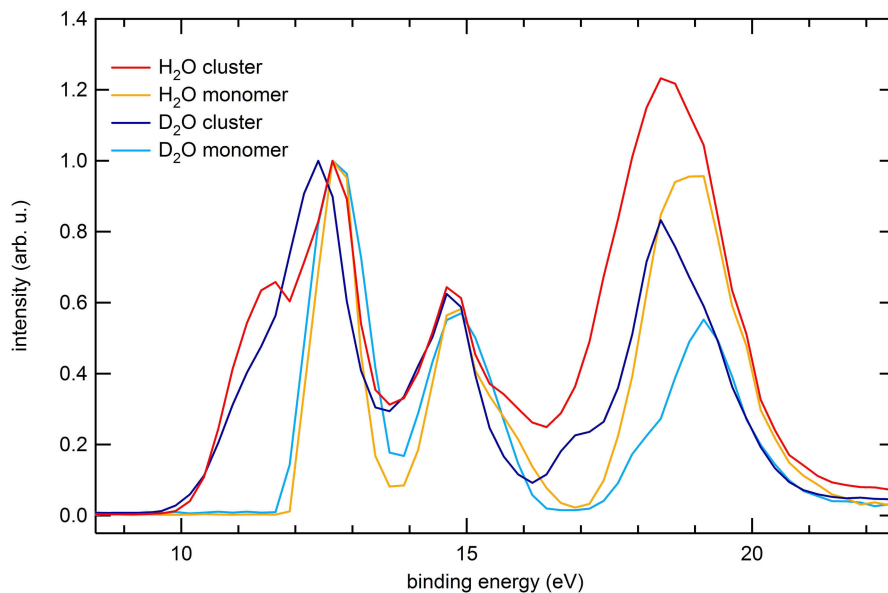


Figure 5.7: Energy spectra of water and deuterated water monomers and clusters recorded with the magnetic bottle spectrometer.

To address the question whether there is a difference between ICD from water and from heavy water, measurements on water clusters have been repeated with the new set-up, using the new water cluster source. Outer valence spectra of water and deuterated water clusters of a mean size  $\langle N \rangle = 135$  as well as of the corresponding monomers are shown in figure 5.7. The monomer spectra were obtained by operating the cluster source off-axis, so that in real terms the cluster beam will not pass the skimmer, and only monomers will reach the interaction region. A possible drawback of this method is, that the alignment of the gas beam with respect to the spectrometer might be different than for the cluster beams, and recording a separate energy calibration scan might be necessary for this case. Photon energies were chosen to be lower than necessary for inner valence ionisation, hence, no ICD signal occurs in these spectra. In case of the water clusters, the contribution due to the clusters in the jet can be seen in the binding energy range between 10 and 12 eV. Also the spectrum for deuterated water clusters shows a shoulder in this energy range, but from the lower intensity

compared to the water cluster spectrum we can conclude on a lower condensation degree.

Figure 5.8 shows ICD energy spectra obtained from coincidence measurements of water clusters and deuterated water clusters. The spectra were recorded after ionisation with 45 eV photons and under otherwise identical experimental conditions. The water cluster beam (red curve) was of mean size  $\langle N \rangle = 120$  and the deuterated water cluster jet (blue curve) of 135. Similarly to figure 5.6, for the ease of comparison, the two curves have been normalised to the same peak intensity. The two spectra look very similar; in both cases, the intensity shows a maximum at about 0.4 eV and then decreases continuously. The fact that the  $\text{H}_2\text{O}$  cluster curve lies above the curve for  $\text{D}_2\text{O}$  clusters, although the latter ones are slightly larger, could simply be due to a marginal higher intensity maximum relative to remainder of the water ICD spectrum. Also, when assuming stronger bonds in deuterated clusters, the electron kinetic energies would be lower. This interpretation would fit with the ICD energy spectrum plotted in figure 5.8, but is, unfortunately, not supported by the outer valence spectra shown in figure 5.7.

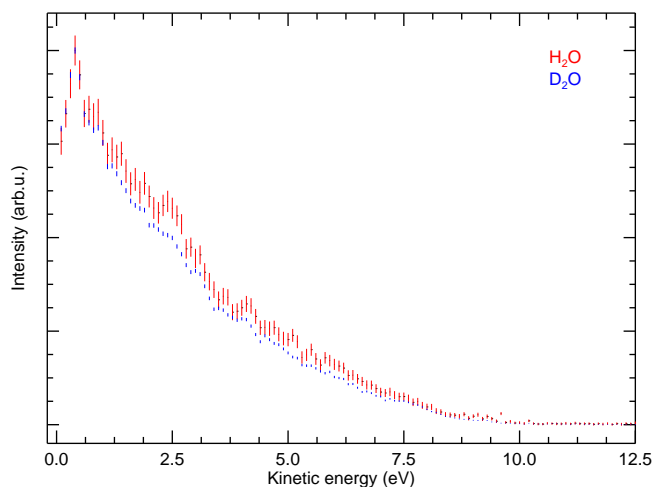


Figure 5.8: Energy spectra of ICD from water clusters and deuterated water clusters ( $\langle N \rangle = 120$  and 135, respectively) recorded after photoionisation with 45 eV.

Therefore, I suggest to return to water and deuterated water clusters and extend the experiments with respect to clustering properties. To record high resolution valence spectra for clusters produced under identical conditions would be of interest in order to determine whether there are deuterium-induced shifts in binding energy observable and to check for possible inherent differences in condensation degrees. These results would assist interpretation of the coincidence data. So far, a clear influence on ICD due to exchanging hydrogen with deuterium cannot be established from our measurement.





# Chapter 6

## conclusion

The aim of this work was to investigate rare gas and water clusters with respect to the occurrence of ICD. About a decade ago, this new type of electronic decay has been predicted by theoreticians to take place in weakly bound, extended systems [49]. Since then, a number of experiments have succeeded in proving its existence in various homogeneous and heterogeneous rare gas clusters [50, 64, 66].

However, despite the theoreticians' prediction that ICD would be a universally occurring phenomenon, so far, no experiment had managed to prove its taking place in hydrogen bonded systems. To address this issue, in a collaborative effort with AG Becker from the Fritz-Haber-Institute in Berlin, an electron-electron coincidence experiment making use of a magnetic bottle spectrometer was performed. It allowed to record coincident electron pairs where both electrons are of similar, low kinetic energy and thus proved suitable for our envisaged experiments on ICD. We succeeded in undoubtedly proving the occurrence of ICD in water clusters [85]. The autoionisation process represents an efficient way of producing low energy electrons, immediately and at the site of initial ionisation. Since water is ubiquitous in nature and the human body consists to more than 50 % of water, ICD should be taken into account when discussing radiation induced DNA damage.

Following the initial success of the experiment, and with the aim of performing new and interesting investigations, a new magnetic bottle spectrometer was then designed and completed with a new vacuum set-up. One of the first systems we investigated using the newly developed instrument was pure neon clusters of various sizes. With the coincidence technique, it was possible to show that the energy spectrum of the ICD electrons does not extend down to zero eV as it does for neon dimers [63]. In addition, we also found evidence for ICD from neon satellite states. Finally, we observed a separate signal from electron pairs due to intra-cluster inelastic scattering, showing a clear dependence on the cluster size.

In the following beamtime, we extended the studies on rare gas clusters to different mixed systems that have not been investigated with respect to ICD so far. In a further study on neon-krypton heterogeneous clusters, we could prove the occurrence of the interatomic Coulombic decay. In this case, the ICD electron is of unusual high kinetic energy: between 9 and 12 eV. The clusters are assumed to consist of a krypton core surrounded by a closed shell of neon atoms. In a systematic study on how the ICD spectrum changes with cluster size and mixing ratio, we found that the ICD peak developed a shoulder on the high kinetic energy side when the krypton content of the mixture was increased from 2 to 5 %. This shoulder was interpreted to arise from ICD where neon atoms close to the larger krypton core were involved. These atoms consequentially have more krypton next neighbours than the ones surrounding smaller krypton cores. The cluster size dependent study did not yield any significant changes in the ICD spectrum. We therefore interpreted the ICD feature as being representative only for the interface between the two cluster components, but not for the cluster structure as a whole.

In further experiments we were concerned with investigating the autoionisation processes occurring in mixed argon-xenon clusters. In this case, electronic decay of inner valence excited states is dependent on the size of the aggregate [119]: Whereas a dimer cannot decay electronically, trimers and larger aggregates might decay via ETMD. Above a certain cluster size, the ICD channel opens and a competition between ETMD and ICD is expected [120]. Our coincidence spectra clearly show an intense signal corresponding to electron pairs of an Ar 3s electron together with a slow electron. The main contribution to the energy spectrum of the slow electron lies below the energies predicted for ETMD [121], meaning that our clusters supposedly were beyond the ‘critical size’.

In a final study, the phenomenon of ICD in water clusters was revisited. Investigations on heavy water did unambiguously show that ICD also takes place in deuterated systems. The energy spectra of deuterated water clusters are very similar to those of ‘normal’ water; no obvious differences in form or energy could be established.

Summarising, we proved that theoretical predictions of the electronic decay of these weakly bound systems are astonishingly precise. Our measured ICD spectra match quite well with the calculated ones, especially if one bears in mind that the cluster beams always consist of a broad distribution of cluster sizes and also monomers.

Although ICD has been investigated on many more systems than described in this thesis, the phenomenon is still far from being completely depleted. For the future, I could imagine some interesting studies concerning the autoionisation processes in weakly bound systems: One could extend the electron-electron coincidence technique and include detection of fragment ions. Also, by performing experi-

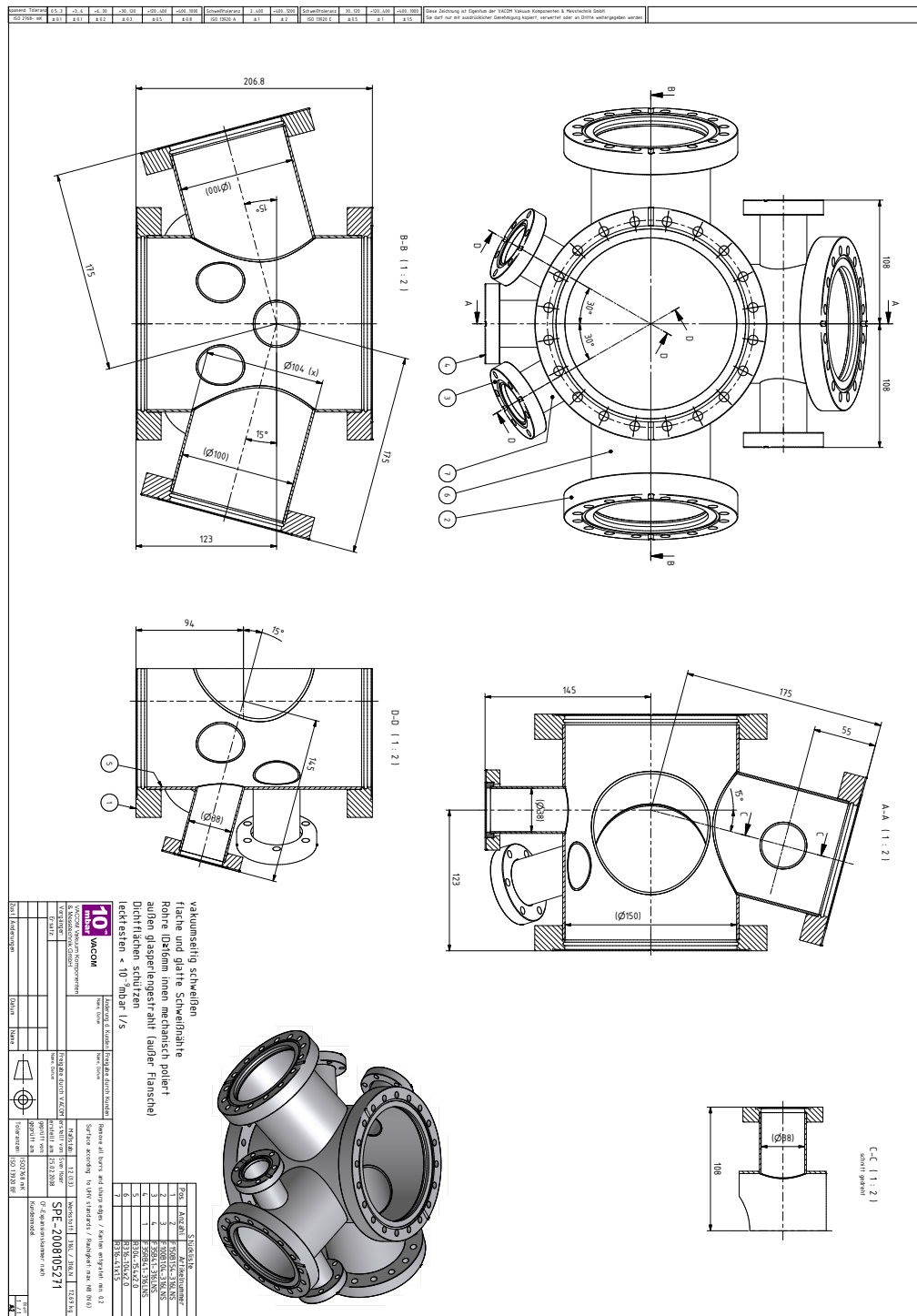
ments at the newly developed free electron lasers (FEL), multiphoton ionisation processes could be studied. In a cluster, multiple autoionisation processes could happen at the same time, probably leading to Coulomb explosion even of large aggregates. Finally, staying with the electron-electron coincidence technique employed for the measurements presented here, many more highly interesting and ‘real world’-relevant systems can be studied, simply start to imagine what can be dissolved in water...



# Appendix A

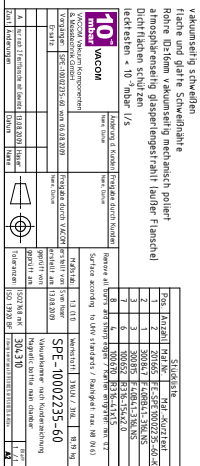
## technical drawings

The following pages contain copies of the technical drawings which have been prepared during the thesis. Most of them belong to the extensive project of constructing a new coincidence set-up based on a magnetic bottle spectrometer which is dedicated to spectroscopy on weakly bound clusters and has been accomplished in 2009. The drawings given here are down-scaled versions of the original ones that often are in A3 or even A2 size. I hope they will serve as a valuable reference for further developments of the set-up and as a source of inspiration for future projects.









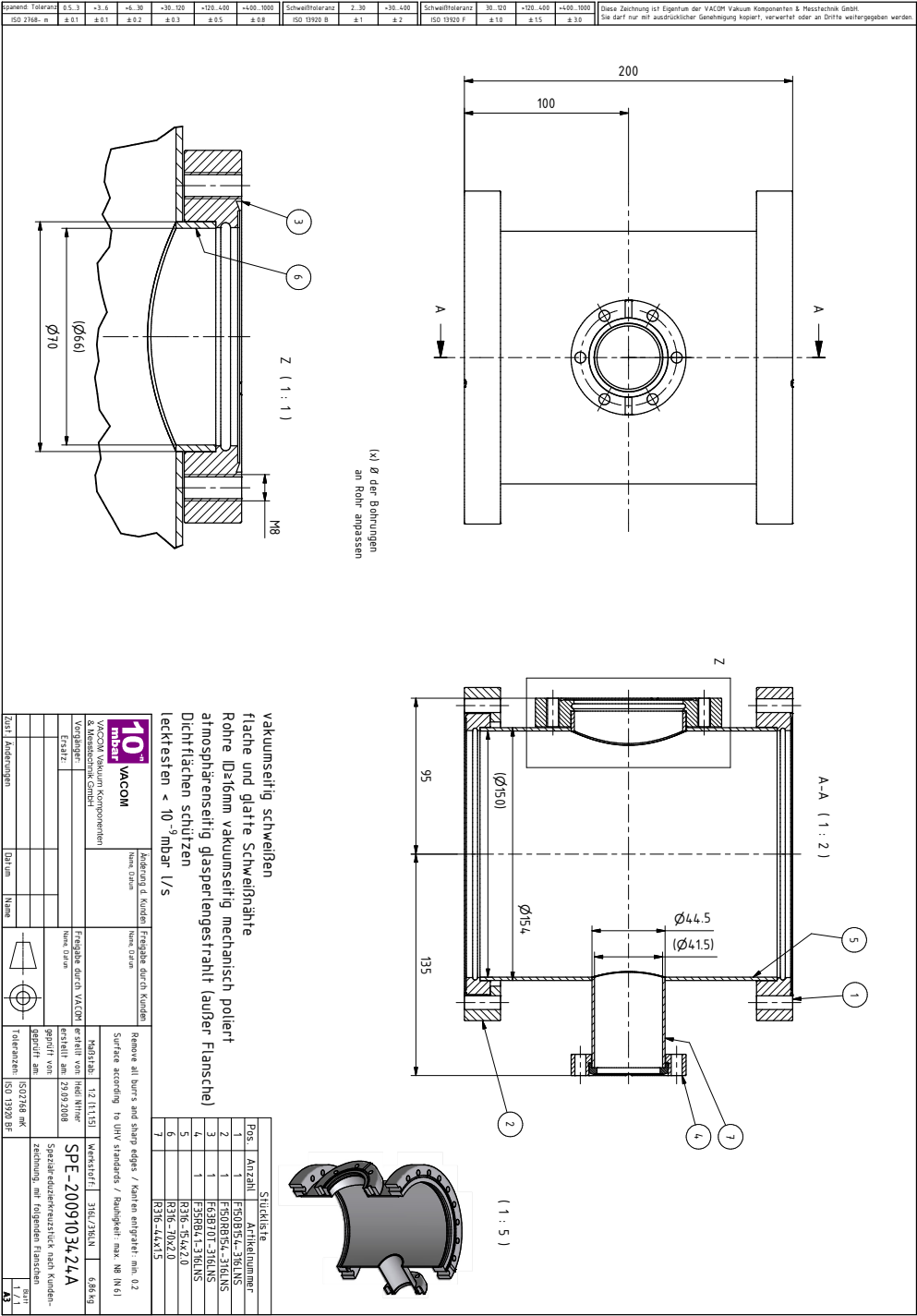
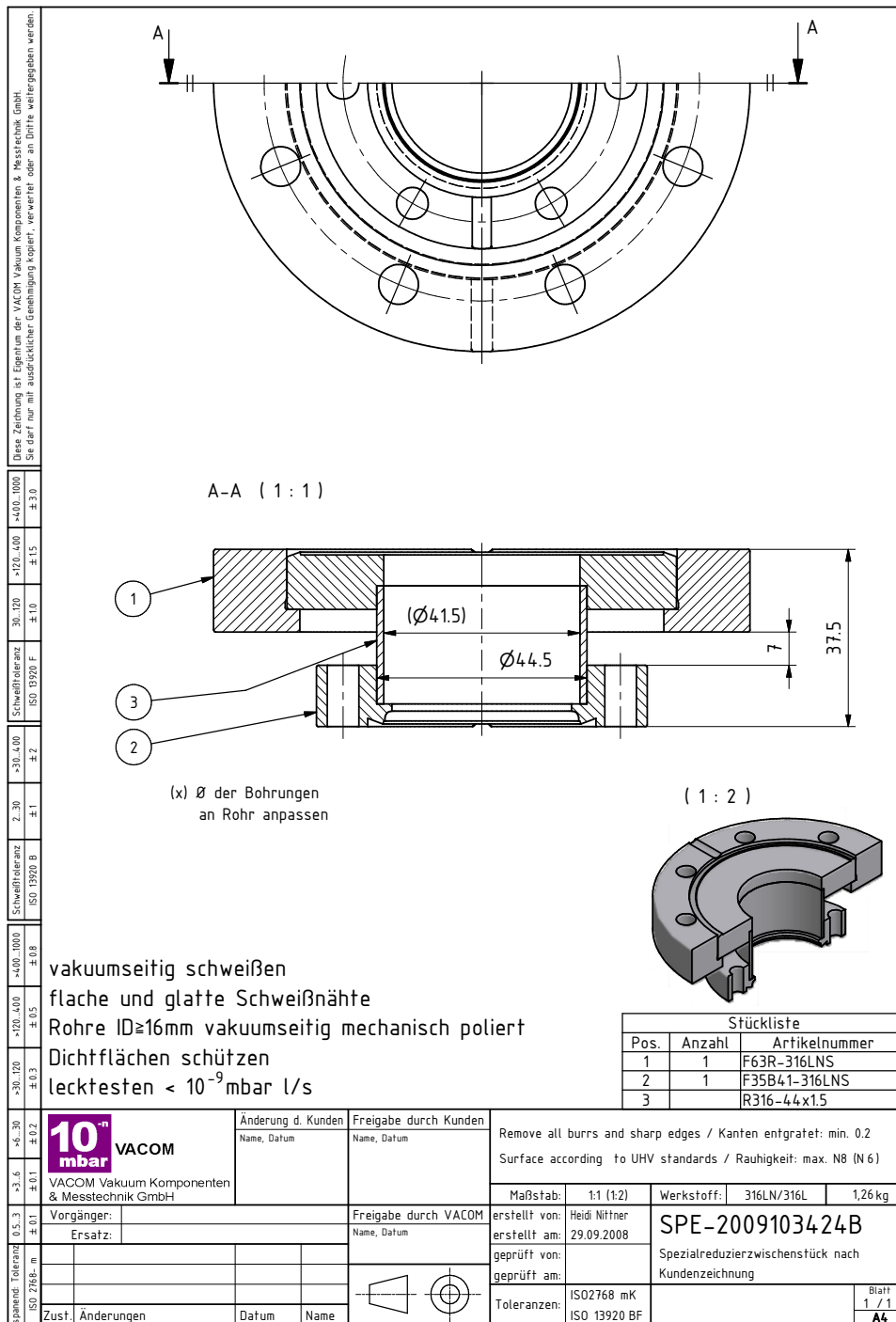


Figure A.4: Vacuum recipient to house the quadrupole mass spectrometer, given as the first and the later modified version and completed with a special adapter.





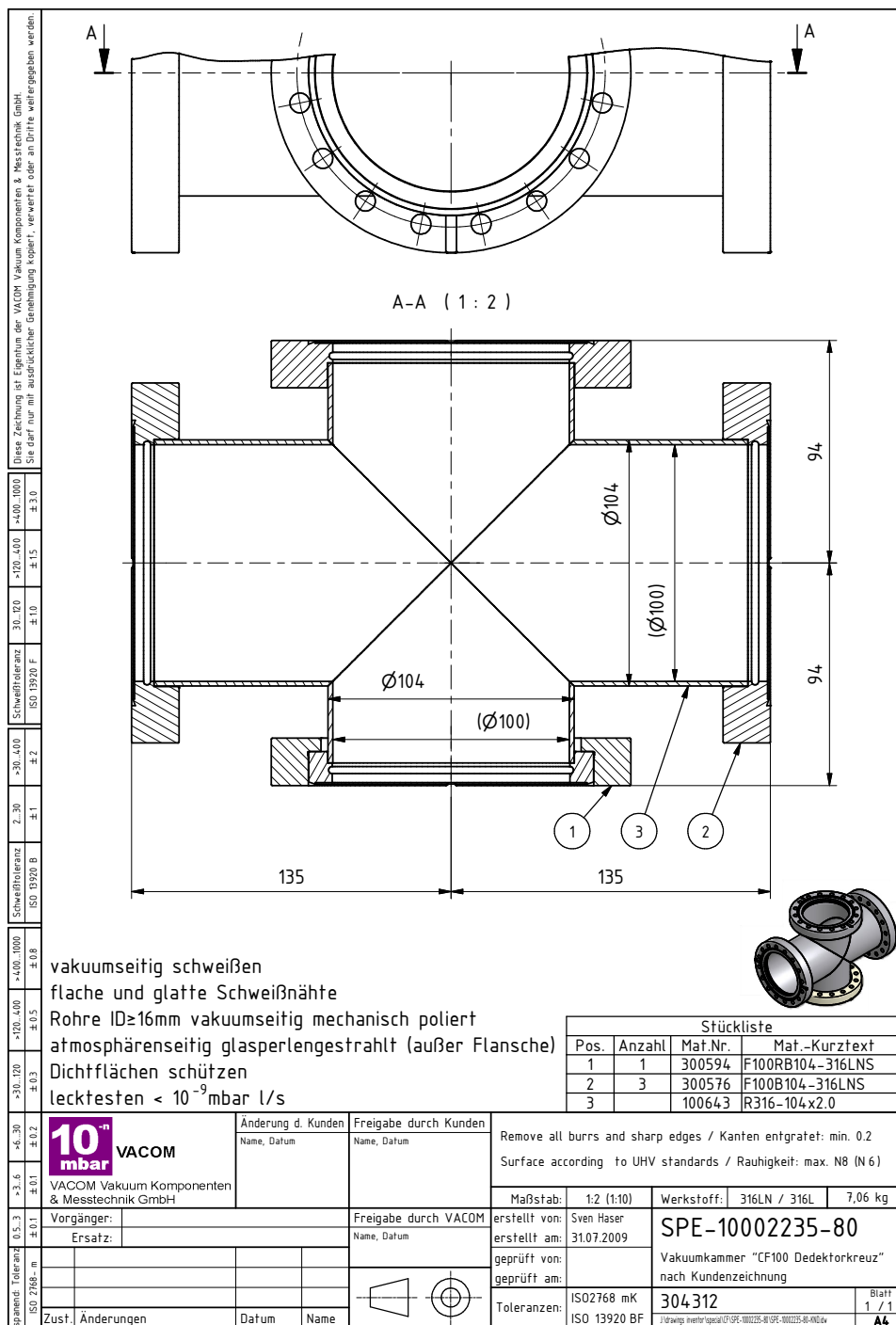
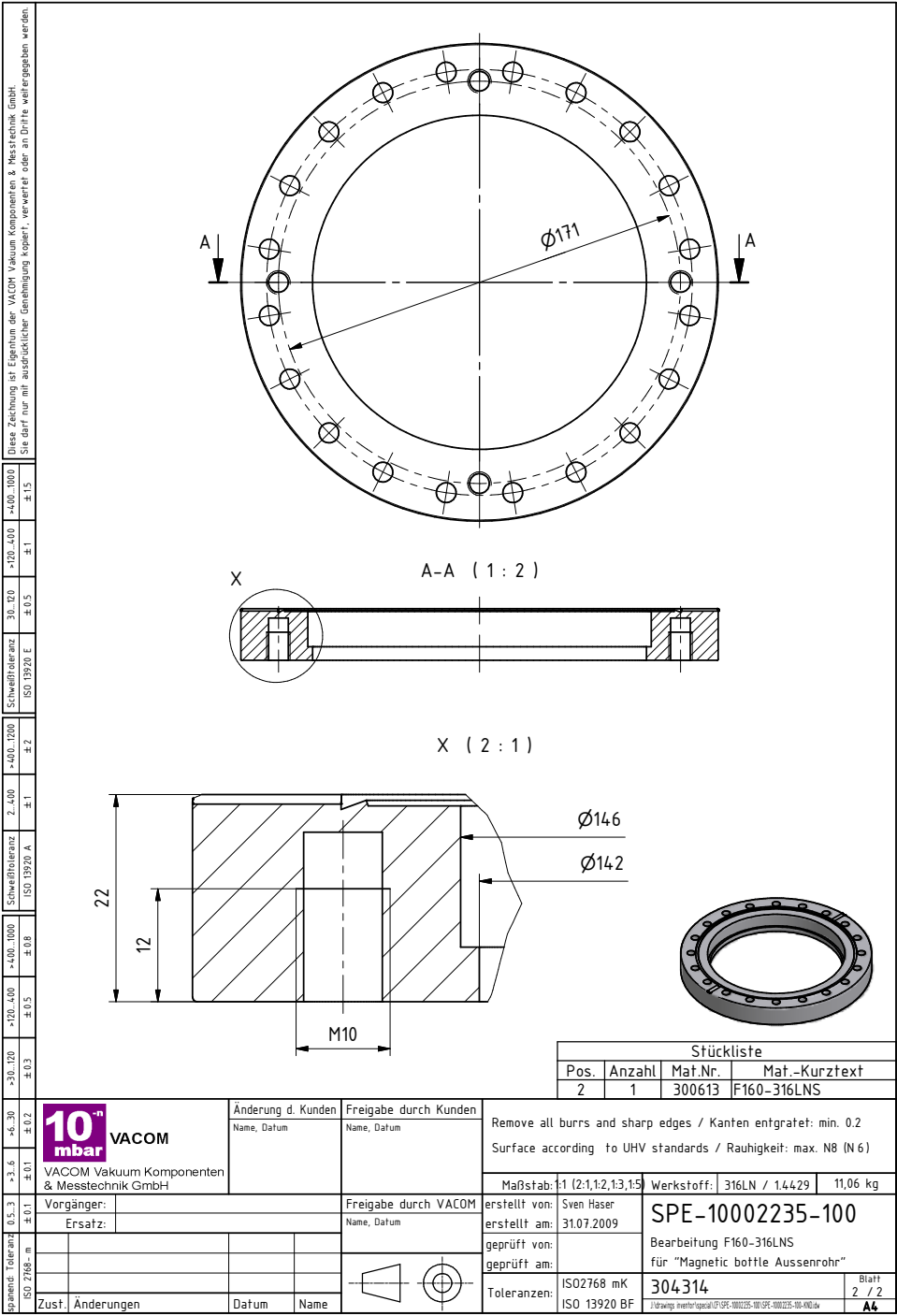


Figure A.6: Vacuum tube of the magnetic bottle spectrometer. The large flange adapts to the main chamber (figure A.3), whereas the small one adapts to the four-way-cross at the detector side (figure A.5).



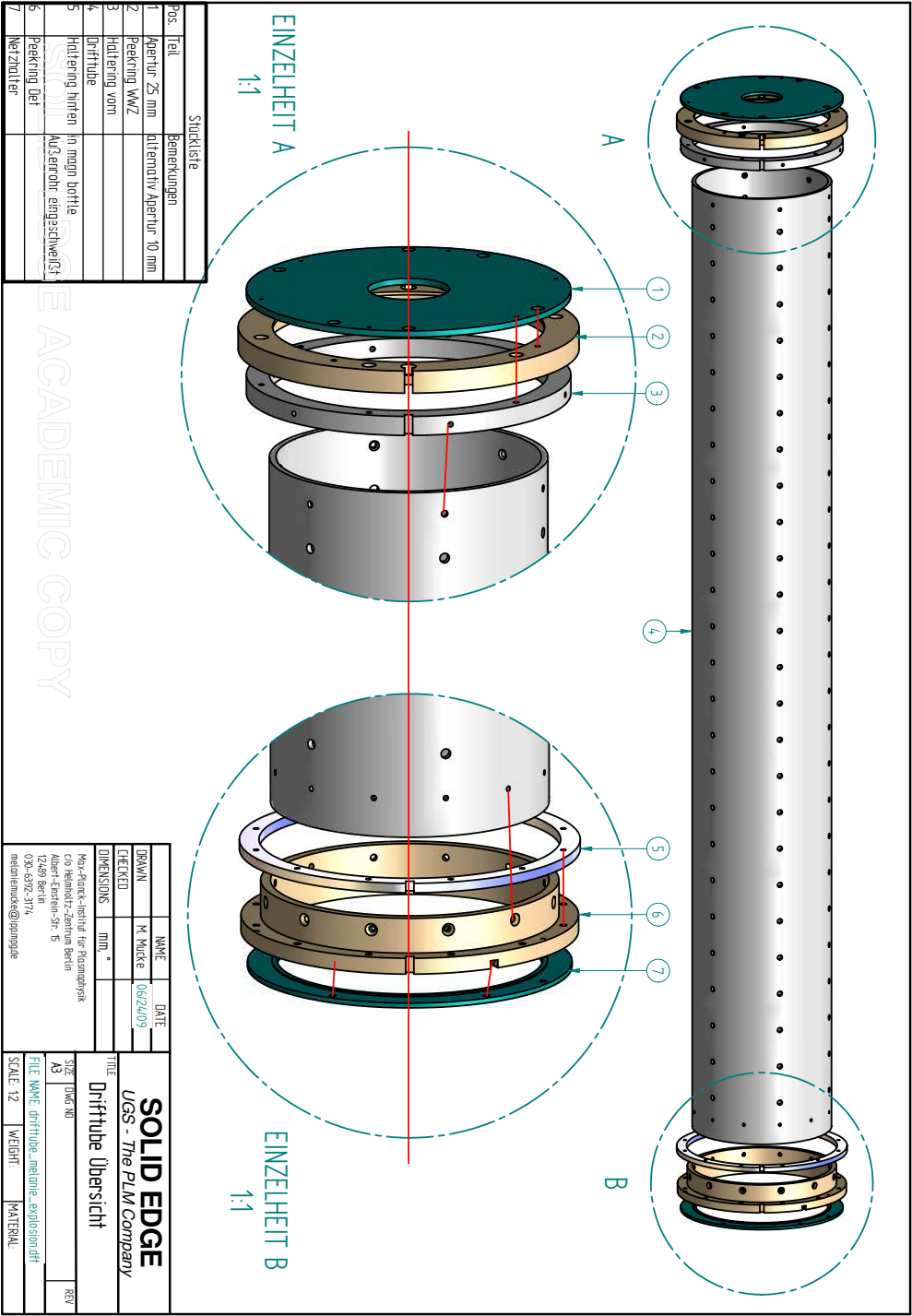


Figure A.7: Inner parts of the magnetic bottle spectrometer in an exploded view.



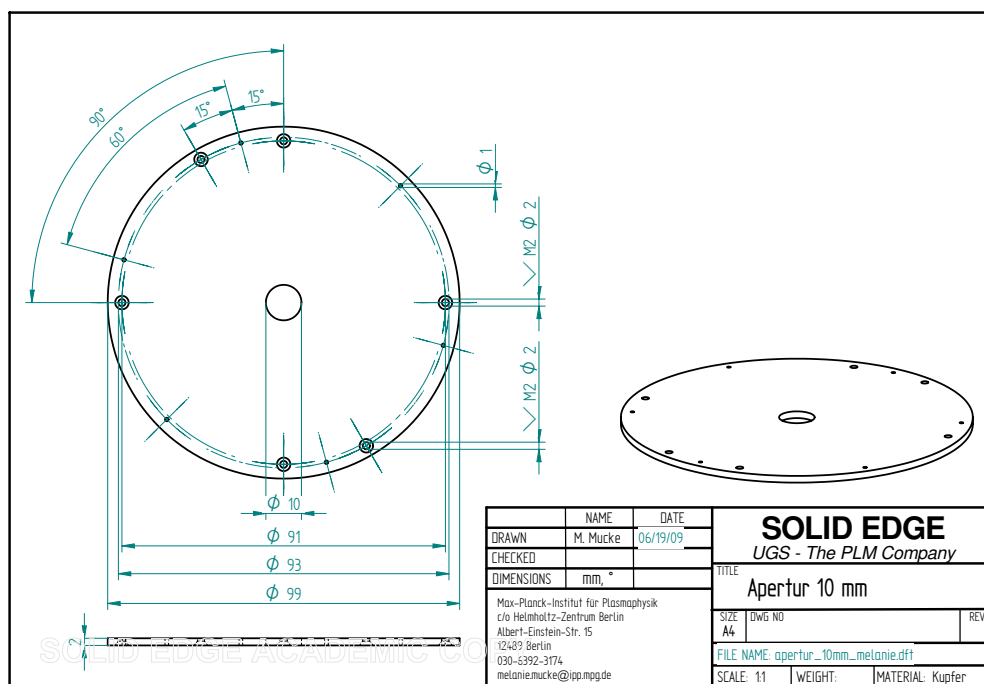


Figure A.8: Apertures to be attached to interaction side of the drifttube.

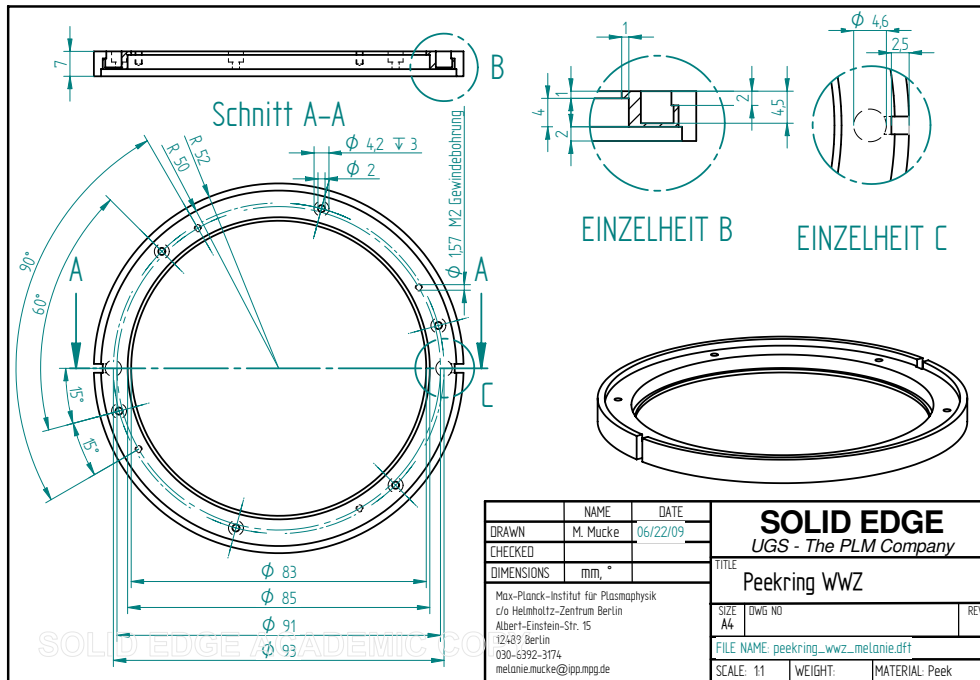


Figure A.9: Peek ring for insulation and attaching the aperture to the drifttube.

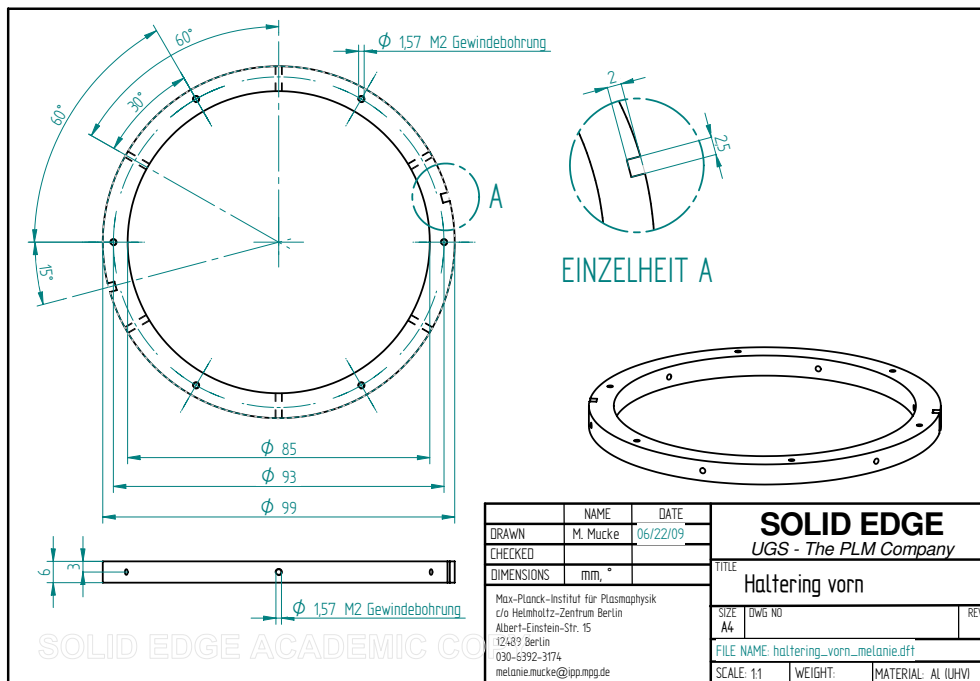


Figure A.10: Ring to fix peek ring from figure A.9 onto the drifttube.







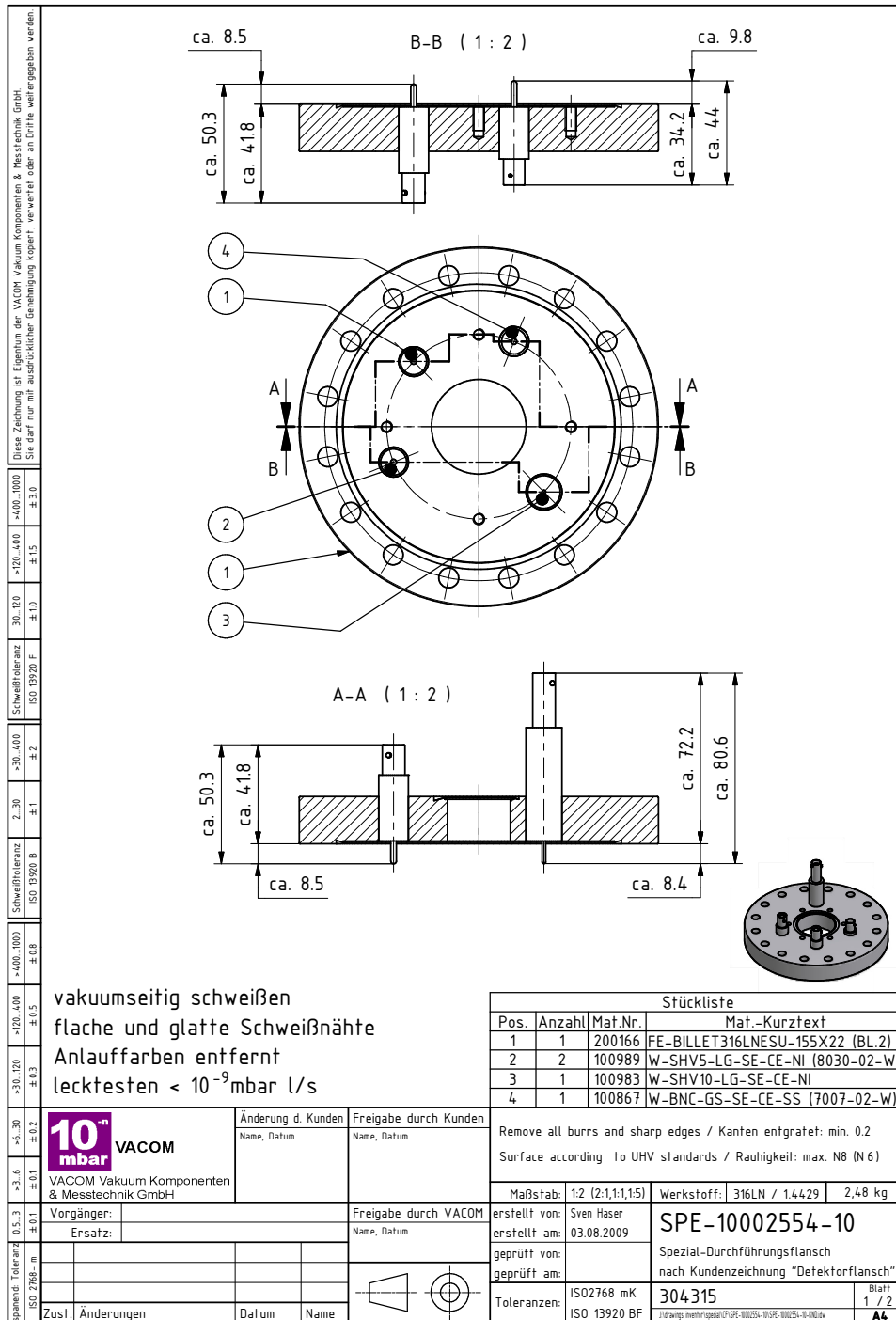


Figure A.15: Flange onto which the detector assembly is mounted.



Technical drawing of a detector holder (Detektorhalterestange) showing front and side views with dimensions and a title block.

**Front View Dimensions:**

- Total length: 207.3
- Left end features: 15 tief, mittig; 8; 5; 1; 13; 20; Entlüftungsbohrung  $\phi$  2
- Right end features: 7; 8

**Side View Dimensions:**

- Left end: M5 Außengewinde
- Right end: M3 Außengewinde

**Quantity:** 4 Stück

**Technical Drawing Table:**

NAME	DATE	<b>SOLID EDGE</b> UGS - The PLM Company	
DRAWN	09/28/09		
CHECKED		TITLE <b>Detektorhalterestange</b>	
DIMENSIONS	mm, *		
Max-Planck-Institut für Plasmaphysik c/o Helmholtz-Zentrum Berlin Albert-Einstein-Str. 15 12489 Berlin 030-6392-3174 melanie.mucke@ipp.mpg.de		SIZE A4	DWG NO REV
		FILE NAME Def_Halterestange.dft	SCALE: 1:1 WEIGHT: MATERIAL: 316LN

**SOLID EDGE ACADEMIC COPY**



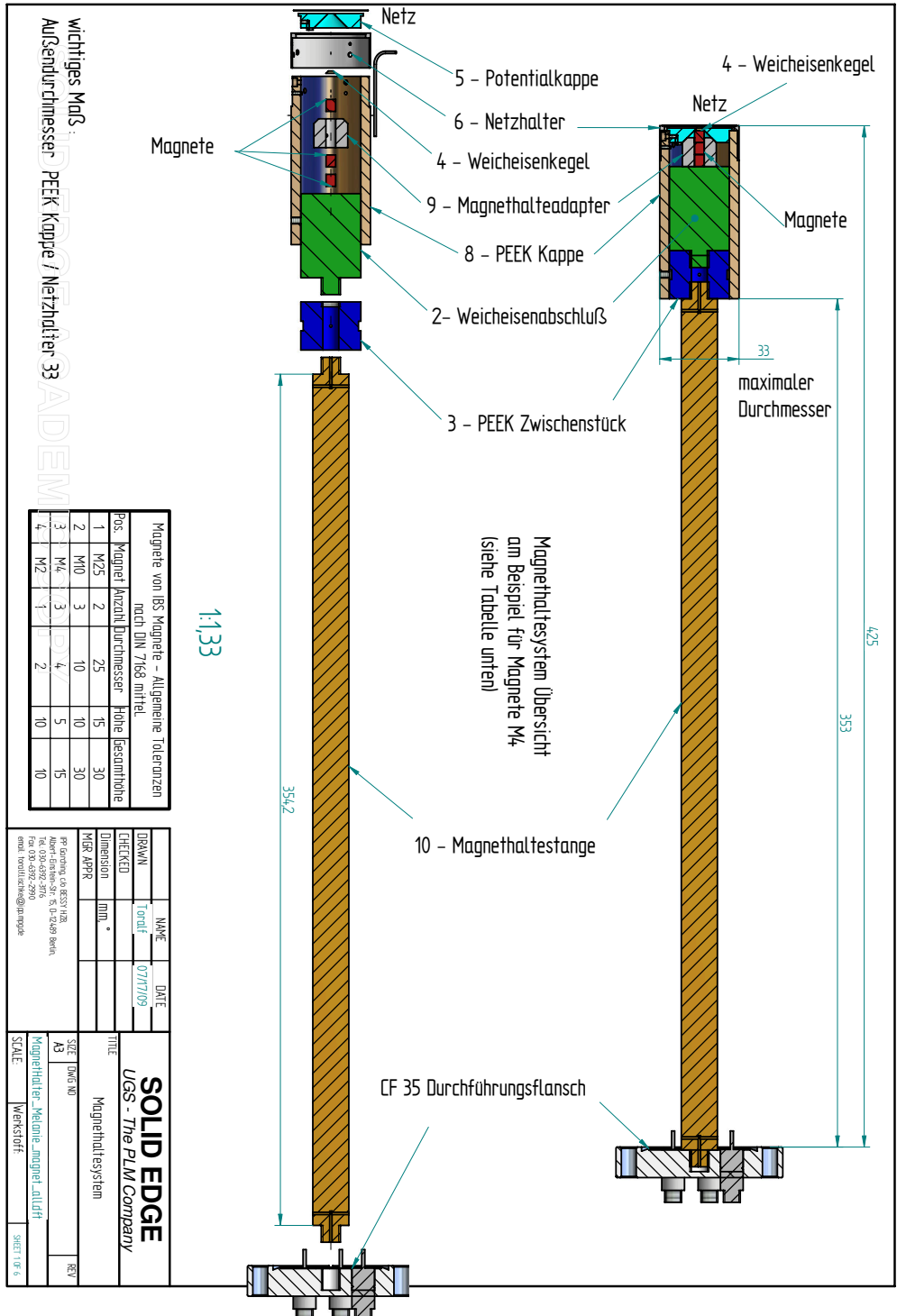
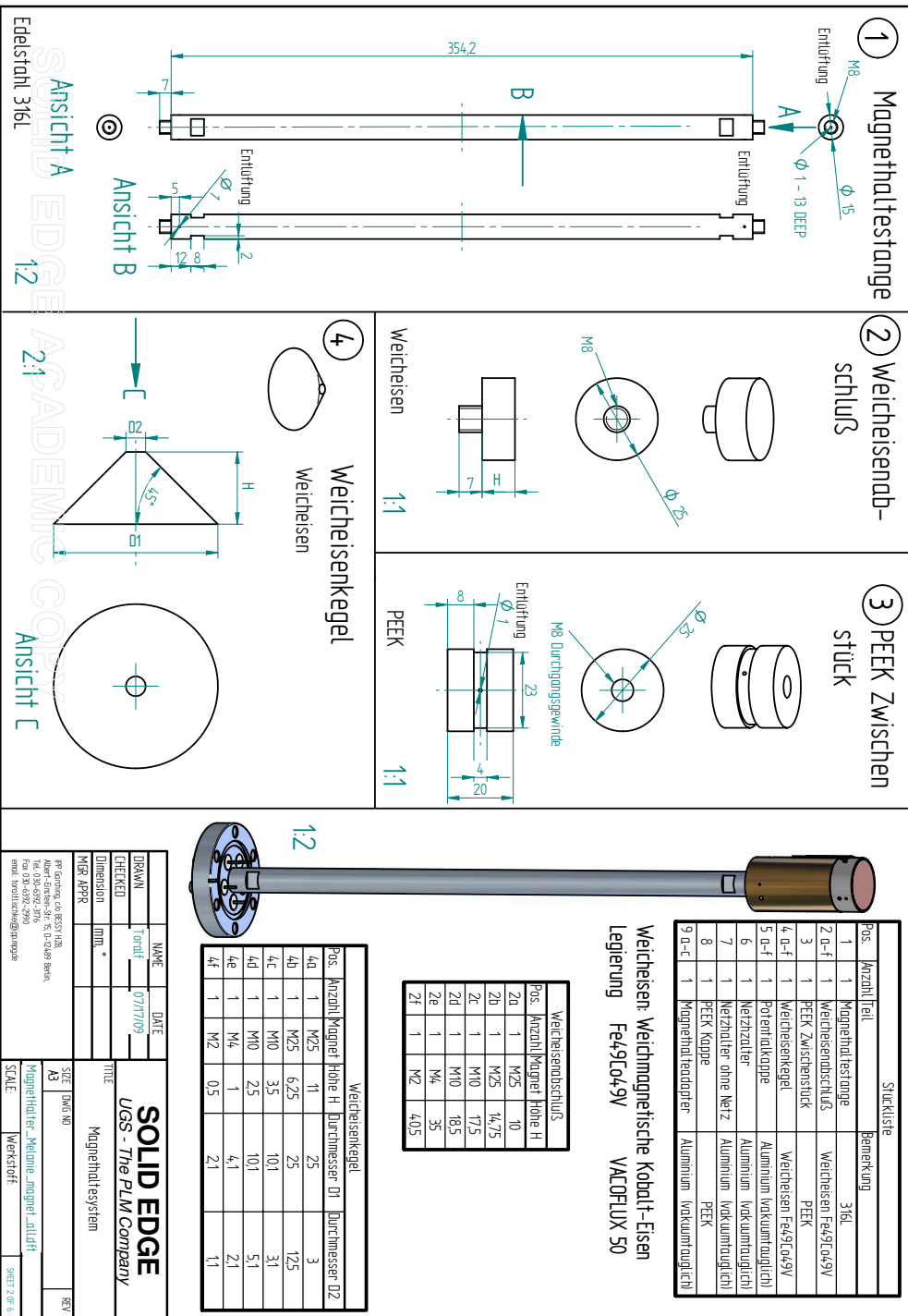
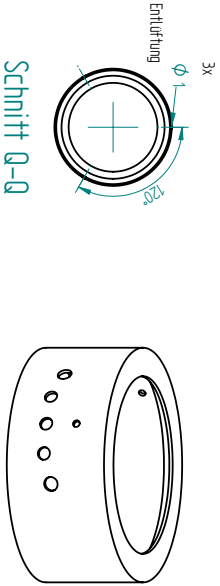


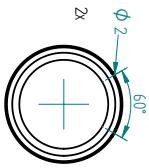
Figure A.18: Modular magnet construction.



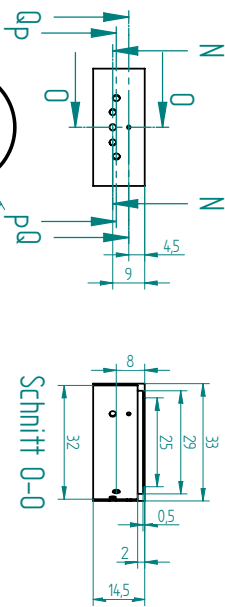
6 Netzhalter



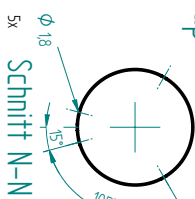
Schnitt Q-Q



Schnitt P-P

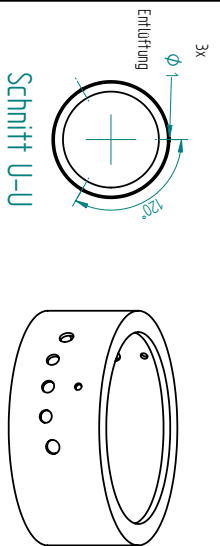


Schnitt O-O

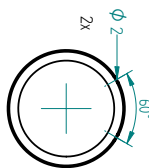


Vakuumtaugliches Aluminium

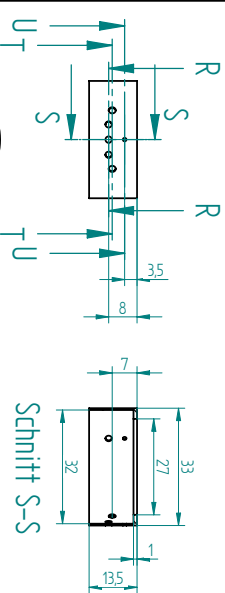
7 Netzhalter ohne Netz



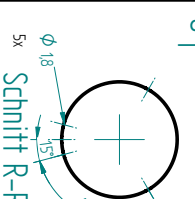
Schnitt U-U



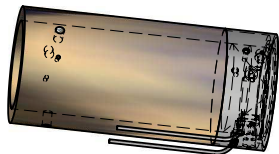
Schnitt T-T



Schnitt S-S

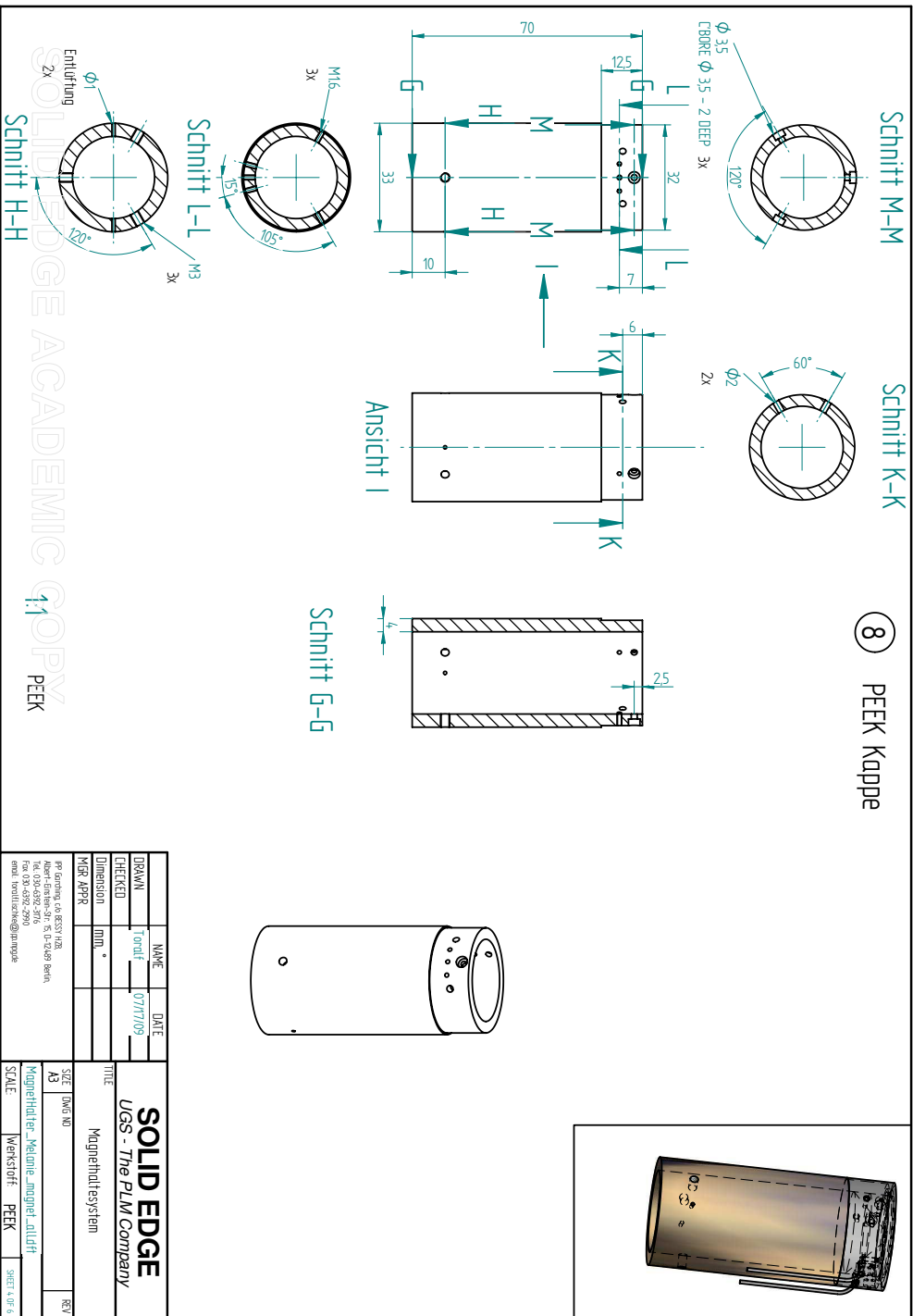


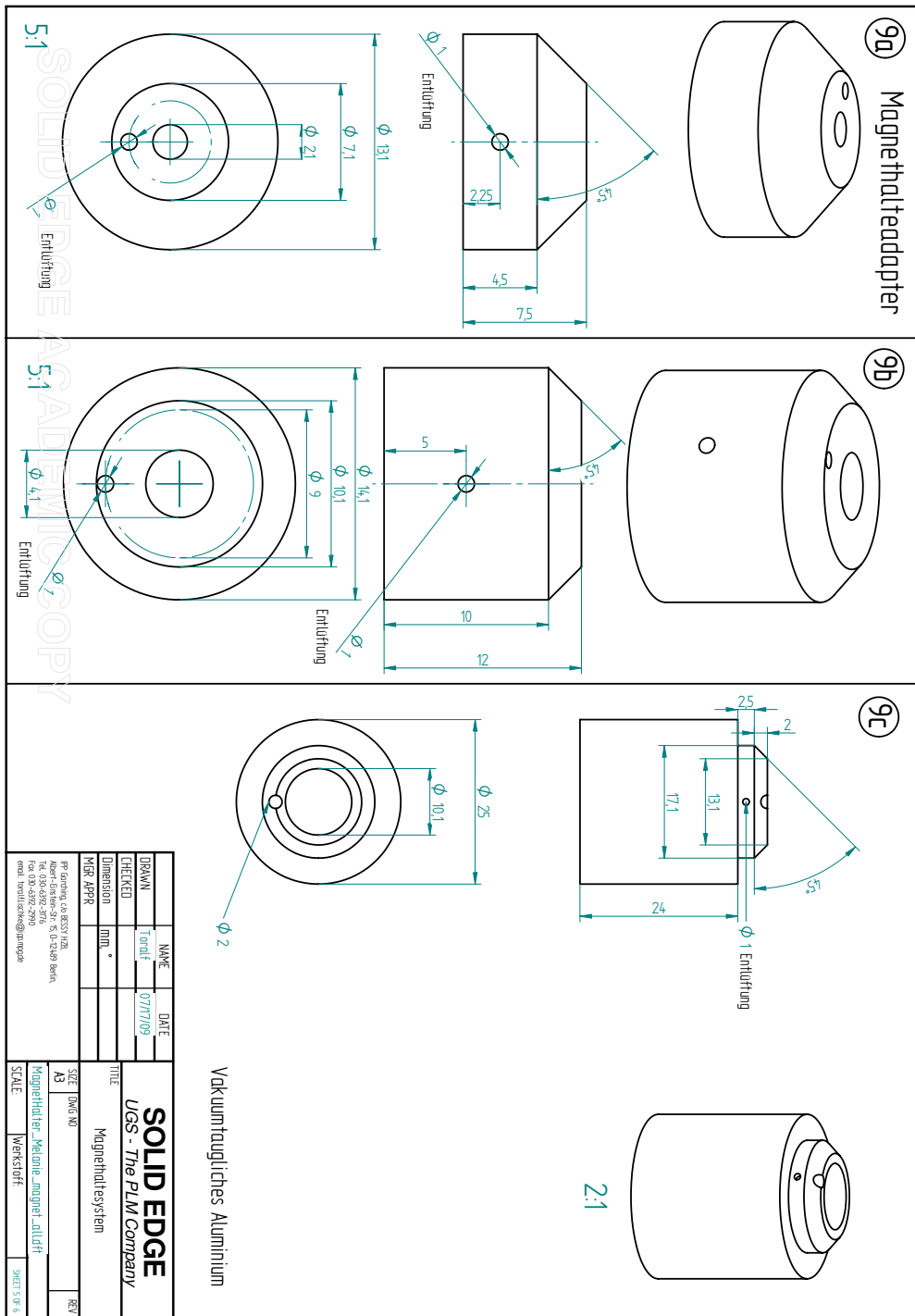
Vakuumtaugliches Aluminium

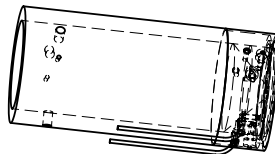
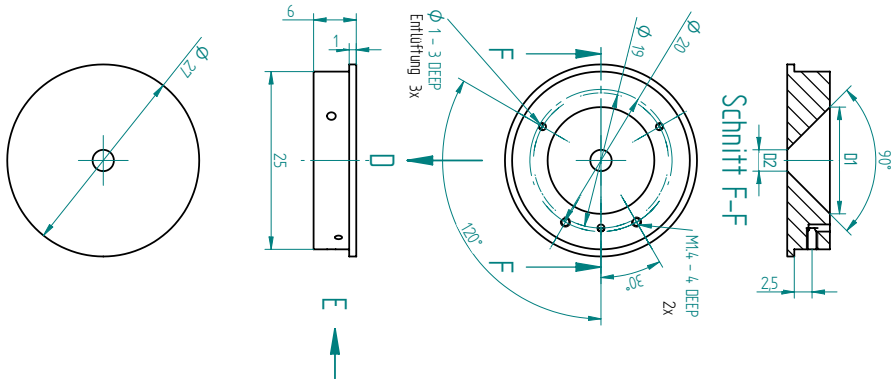


1:1

NAME	DATE	SOLID EDGE	
BROWN	07/11/09	UGS - The PLM Company	
CHECKED		TITLE	
Dimension	mm	Magnethaltesystem	
WGR APPR		SIZE DWS WD	
		A3	
		Magnethalter-Melanie-magnet_alu.dft	
		SCALE	
		Werkstoff Aluminium	
		Sheet 1 of 4	







Potentialkappe	
Pos.	Anzahl/Magnet
5a	1
5b	1
5c	1
5d	1
5e	1
5f	1

<b>SOLID EDGE</b> <i>UGS - The PLM Company</i>		NAME _____ DATE _____	
TITLE _____		DRAWN _____ CHECKED _____ Dimension mm _____ MGR APPR _____	
SIZE (INCH NO) _____ A3		PR FORMING TO BESSY INZ PL 03-03-09 3170 TEL 03-6352-2900 FAX 03-6352-2900 E-MAIL: service@ugr.com.tw	
Magnethol test Magnethol test system		SCALE _____ WEIGHTS: Magnesium Aluminum _____ _____ SHEET 6 OF 6	

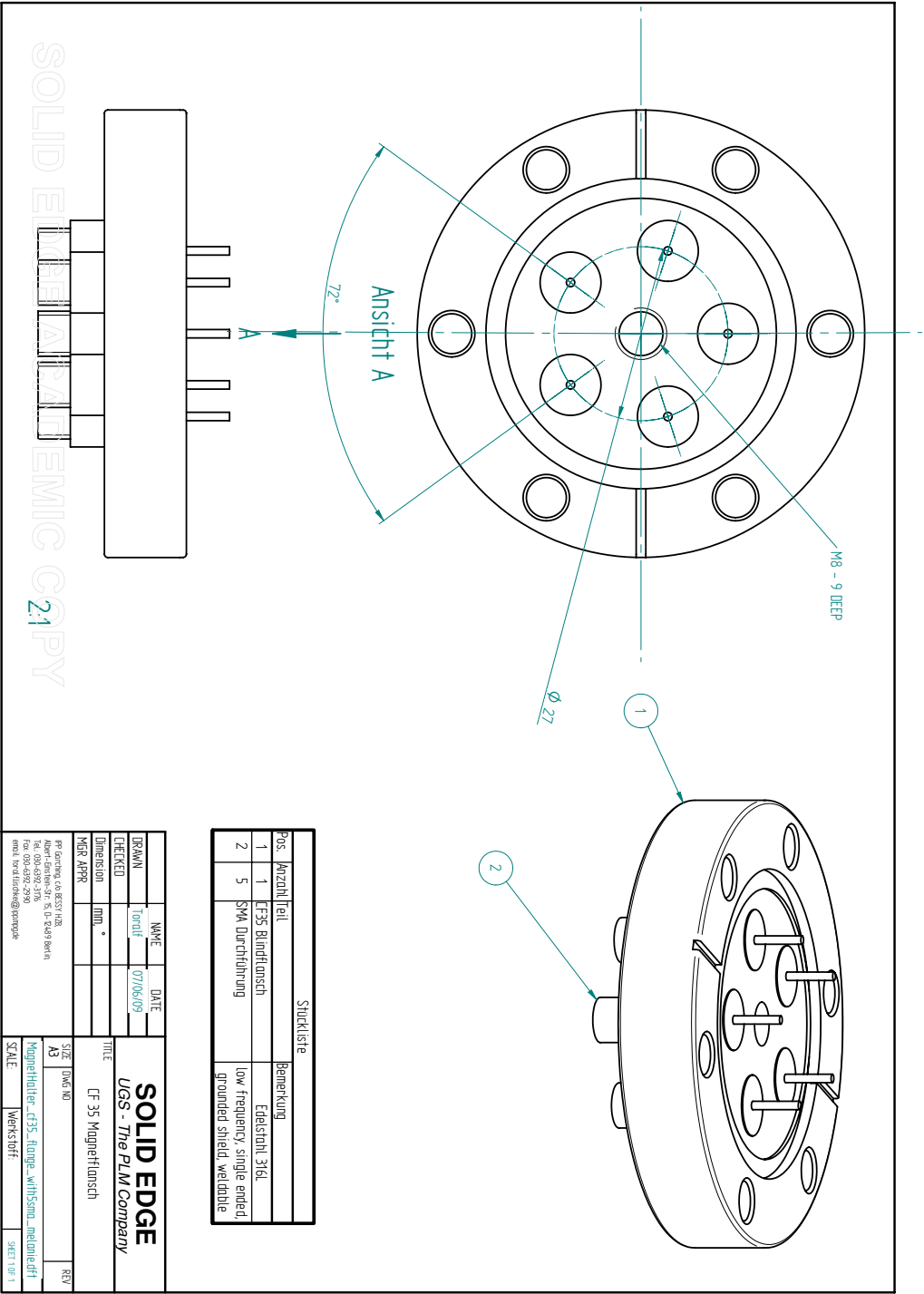


Figure A.19: Flange onto which the magnet is mounted.

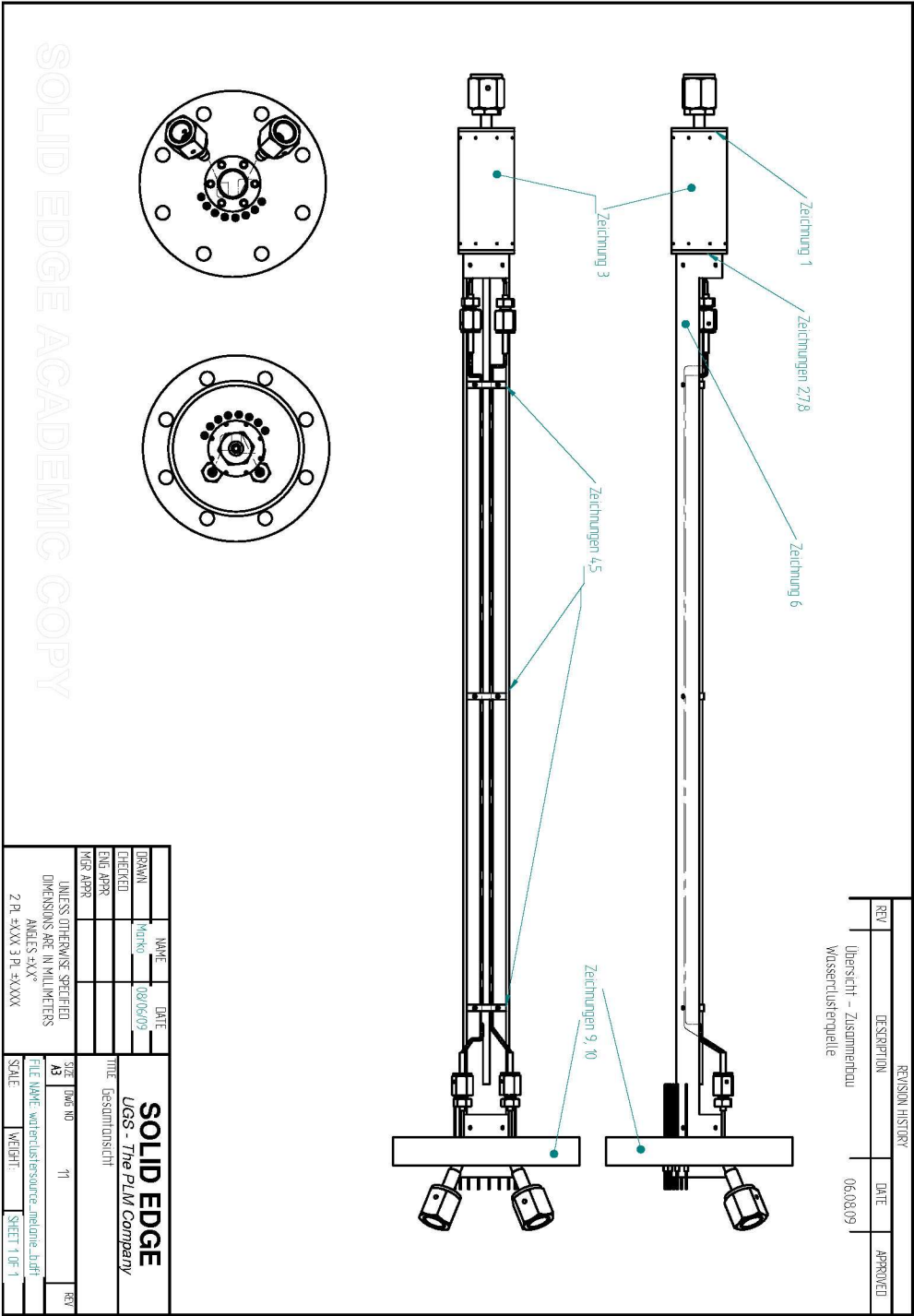


Figure A.20: Water cluster source.



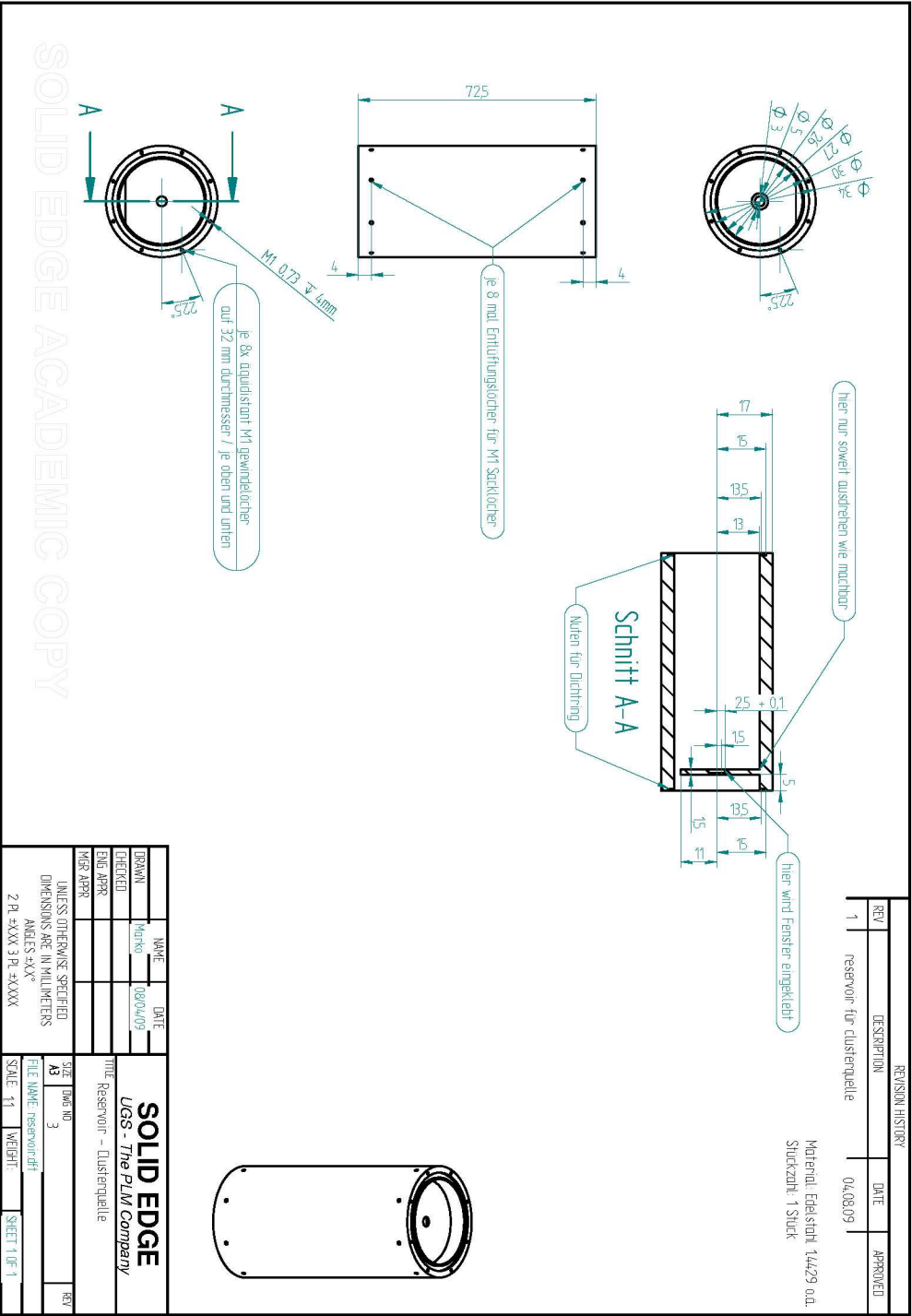


Figure A.21: Reservoir body of water cluster source.

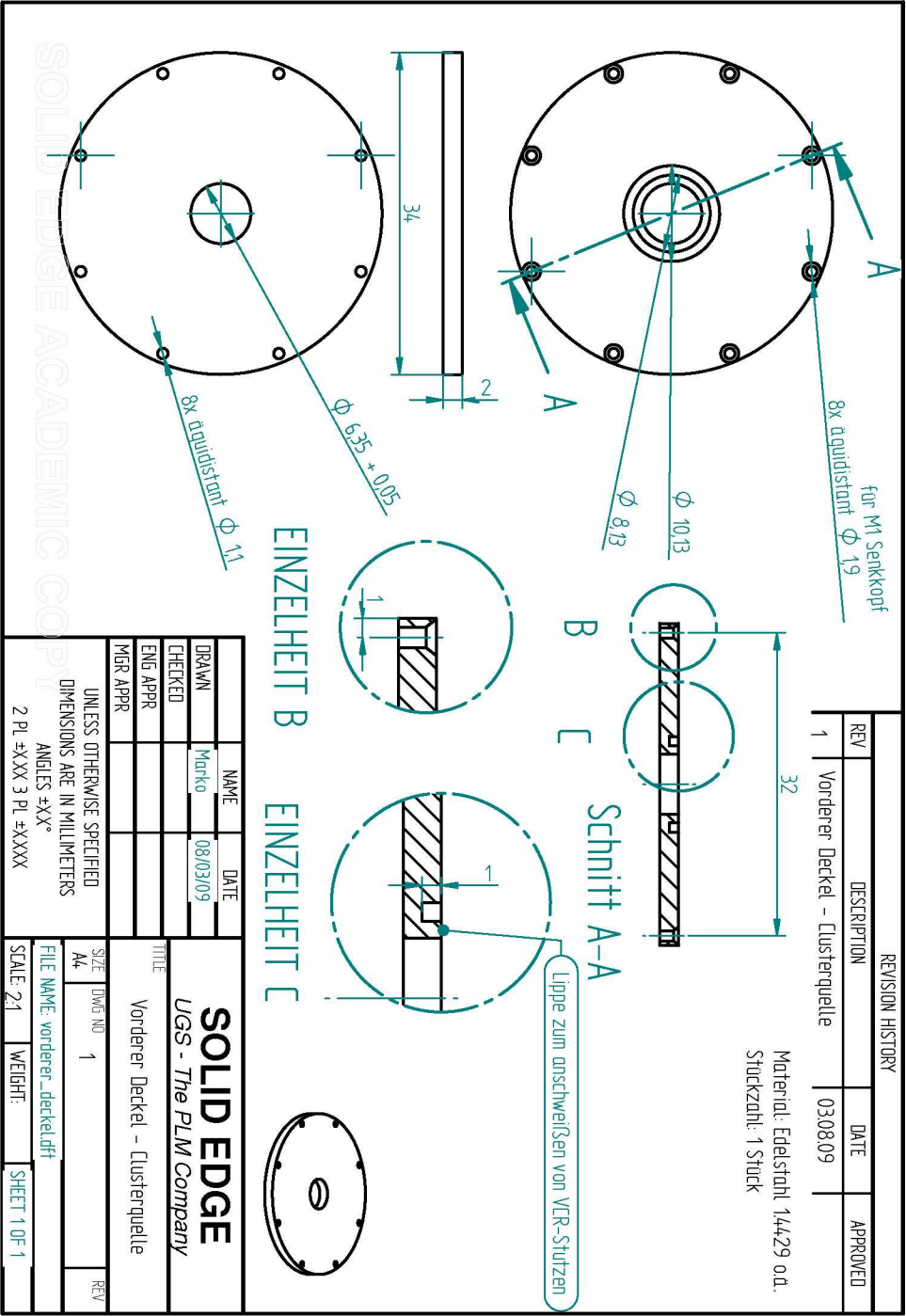


Figure A.22: Water cluster source, lid to close front of reservoir and attach nozzle.

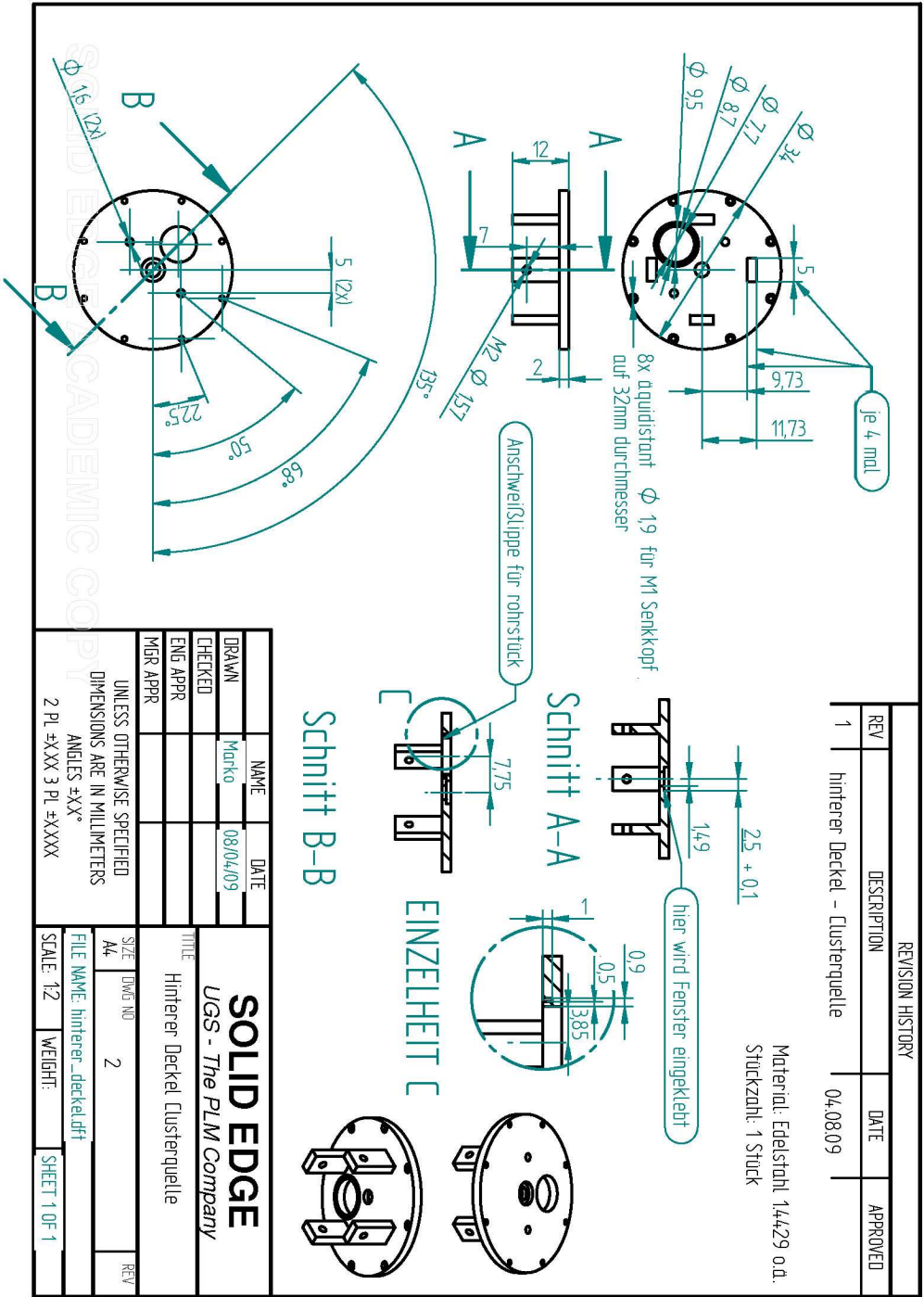


Figure A.23: Water cluster source, lid to close back of reservoir. Connects to mounting tube, holds water supplies and heater.

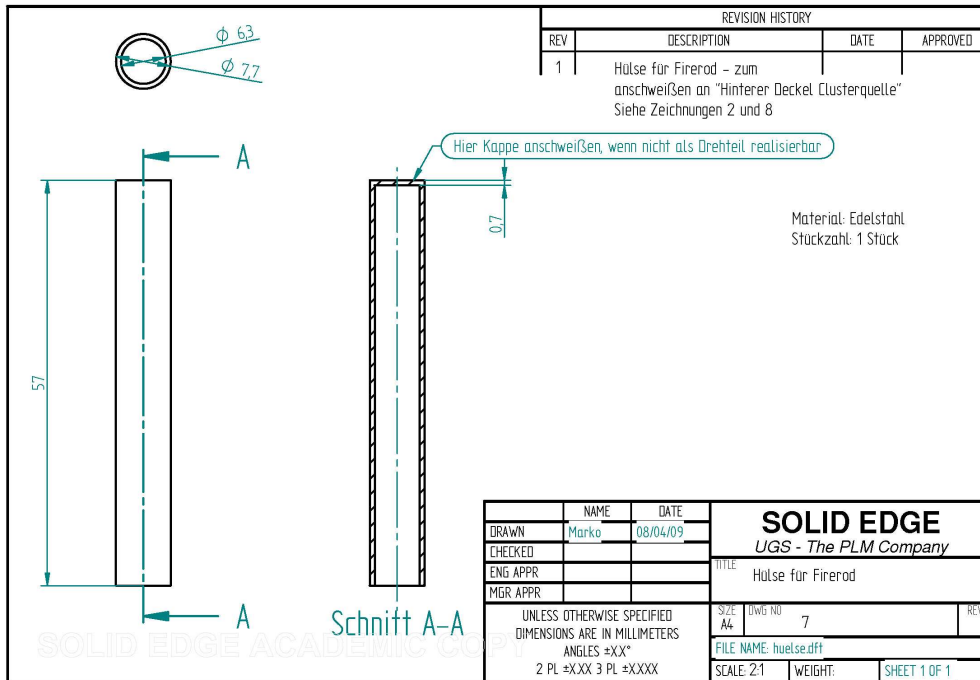


Figure A.24: Water cluster source, cone that holds the heater, welded into back lid.

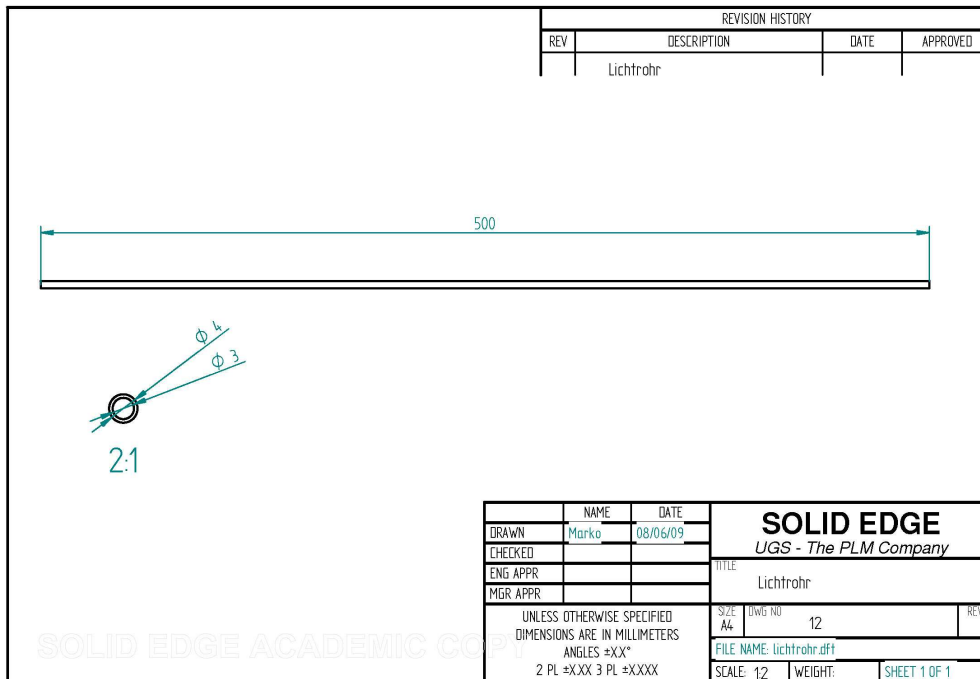


Figure A.25: Water cluster source, light guide tube for laser, fixed on mounting tube.

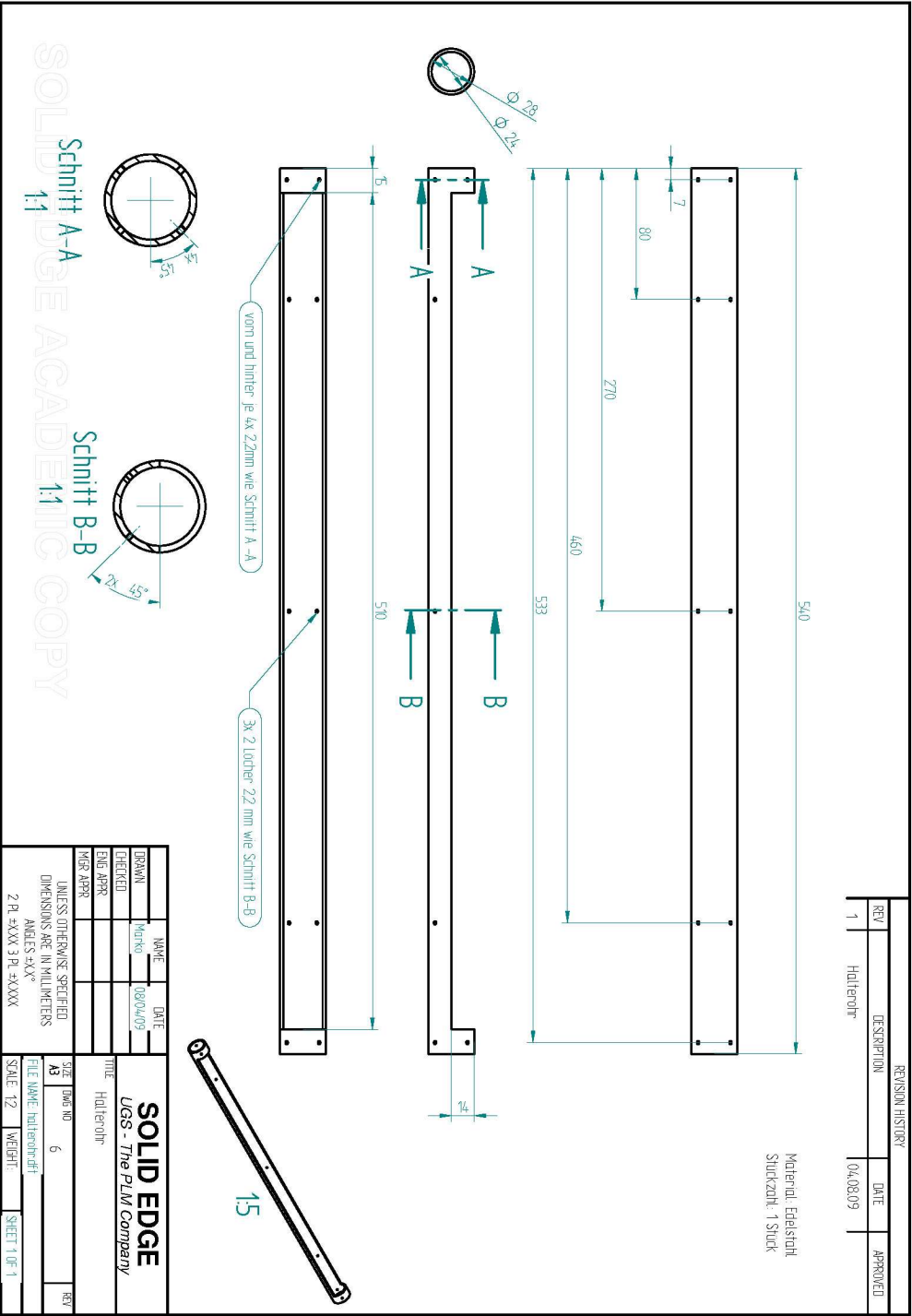


Figure A.26: Water cluster source, open tube to mount reservoir onto flange.

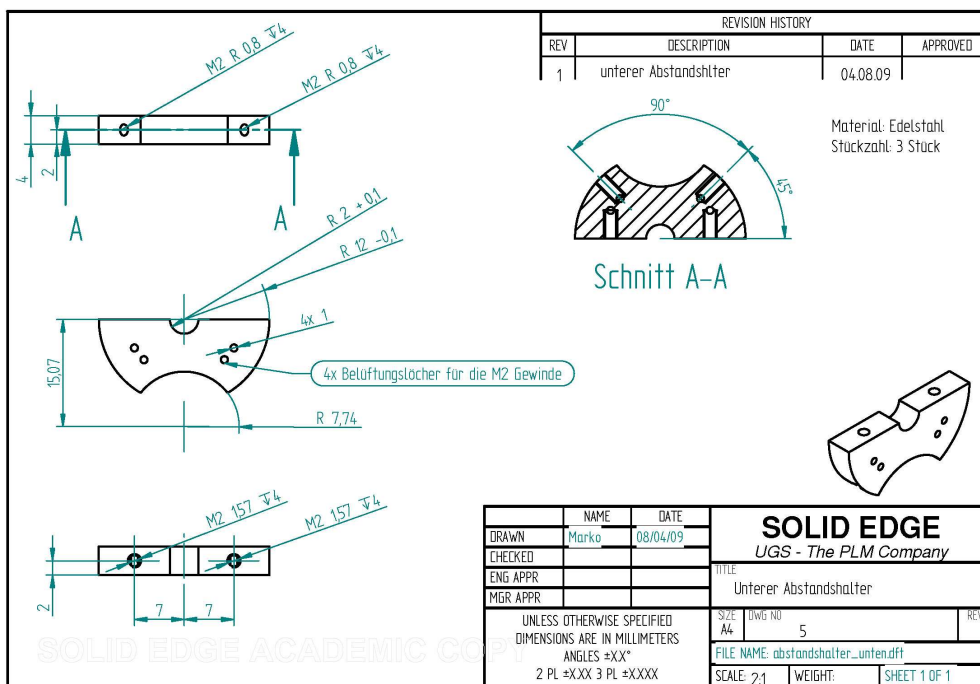
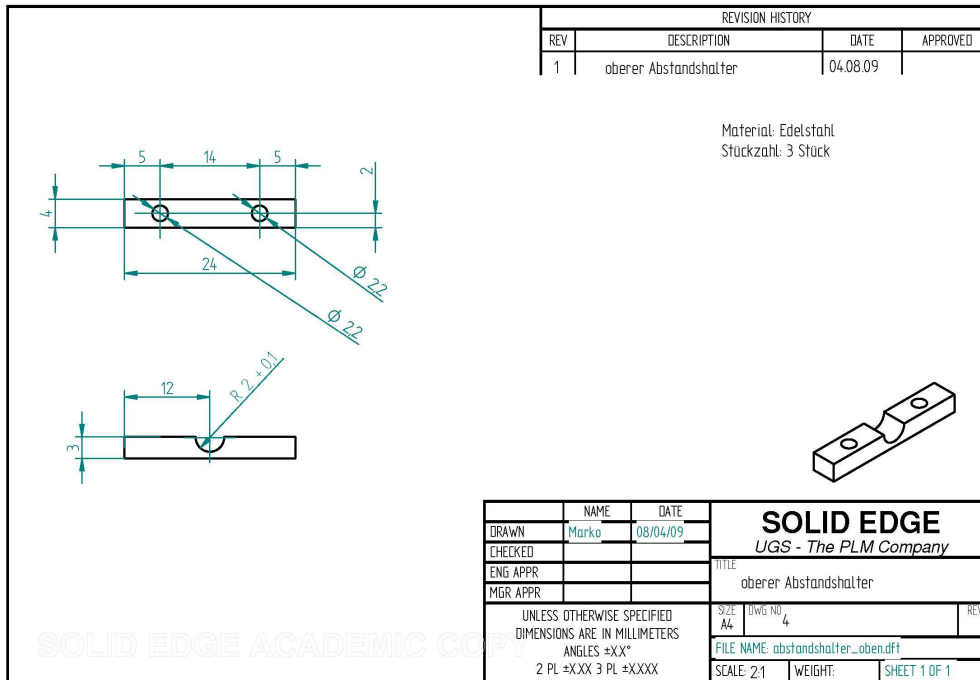
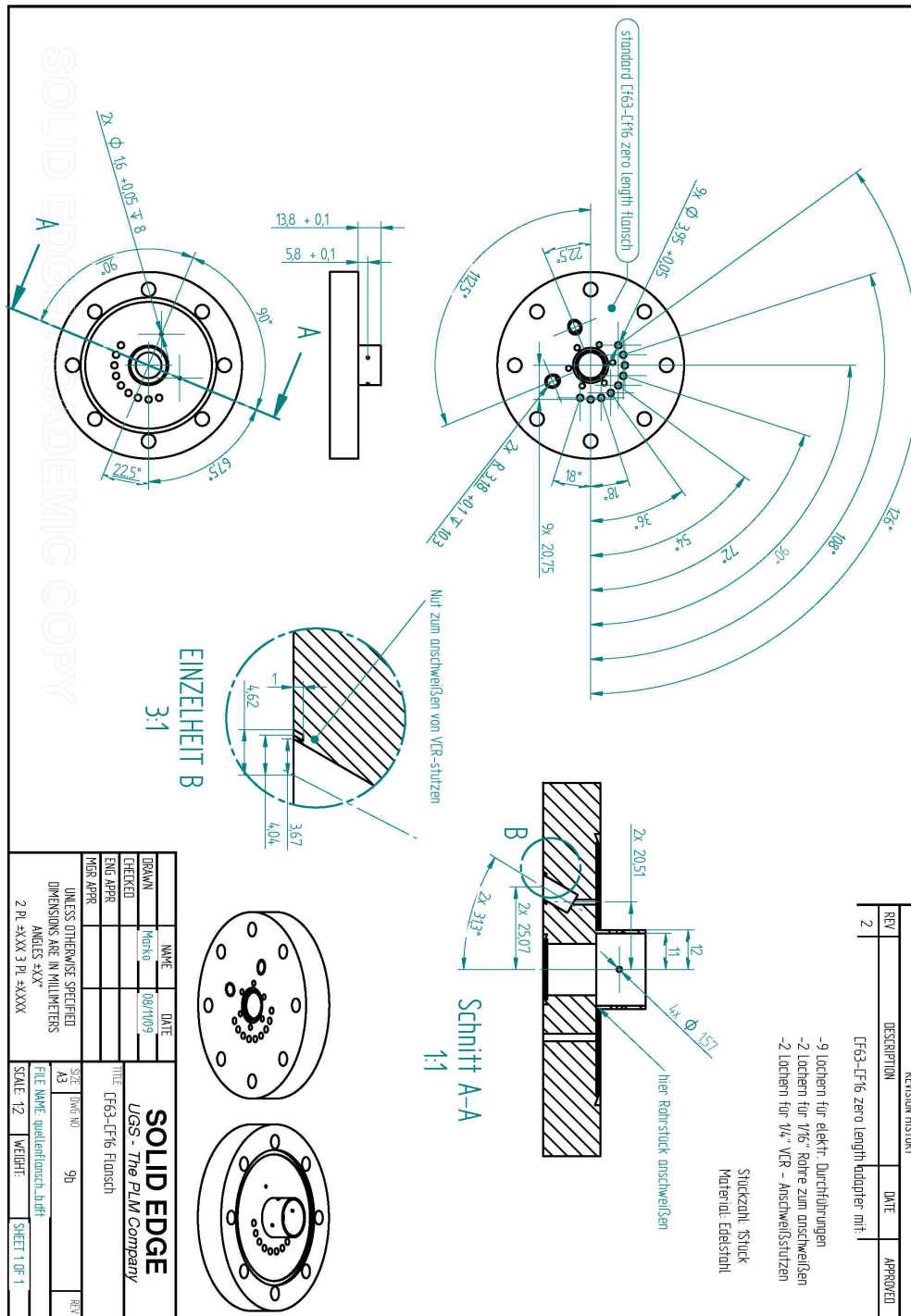


Figure A.27: Water cluster source, mounting parts to fix light guide onto mounting tube.



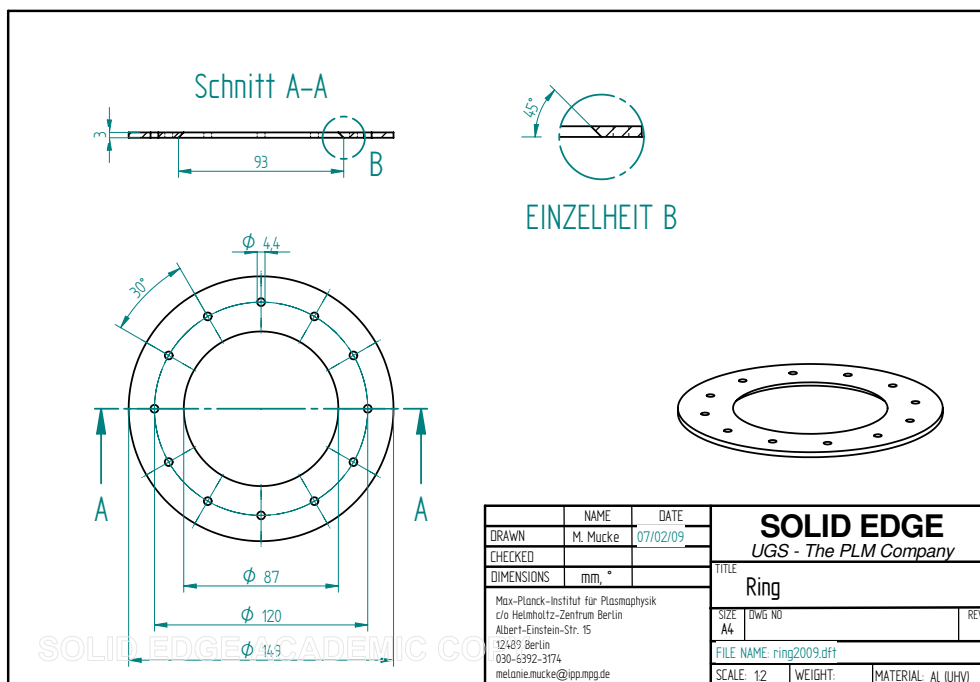
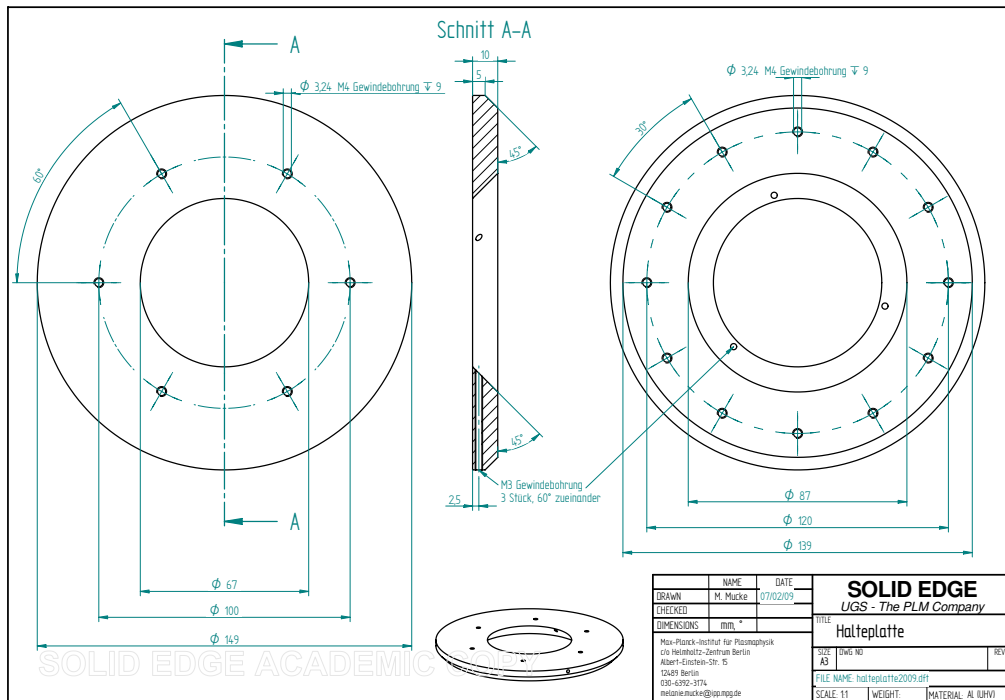
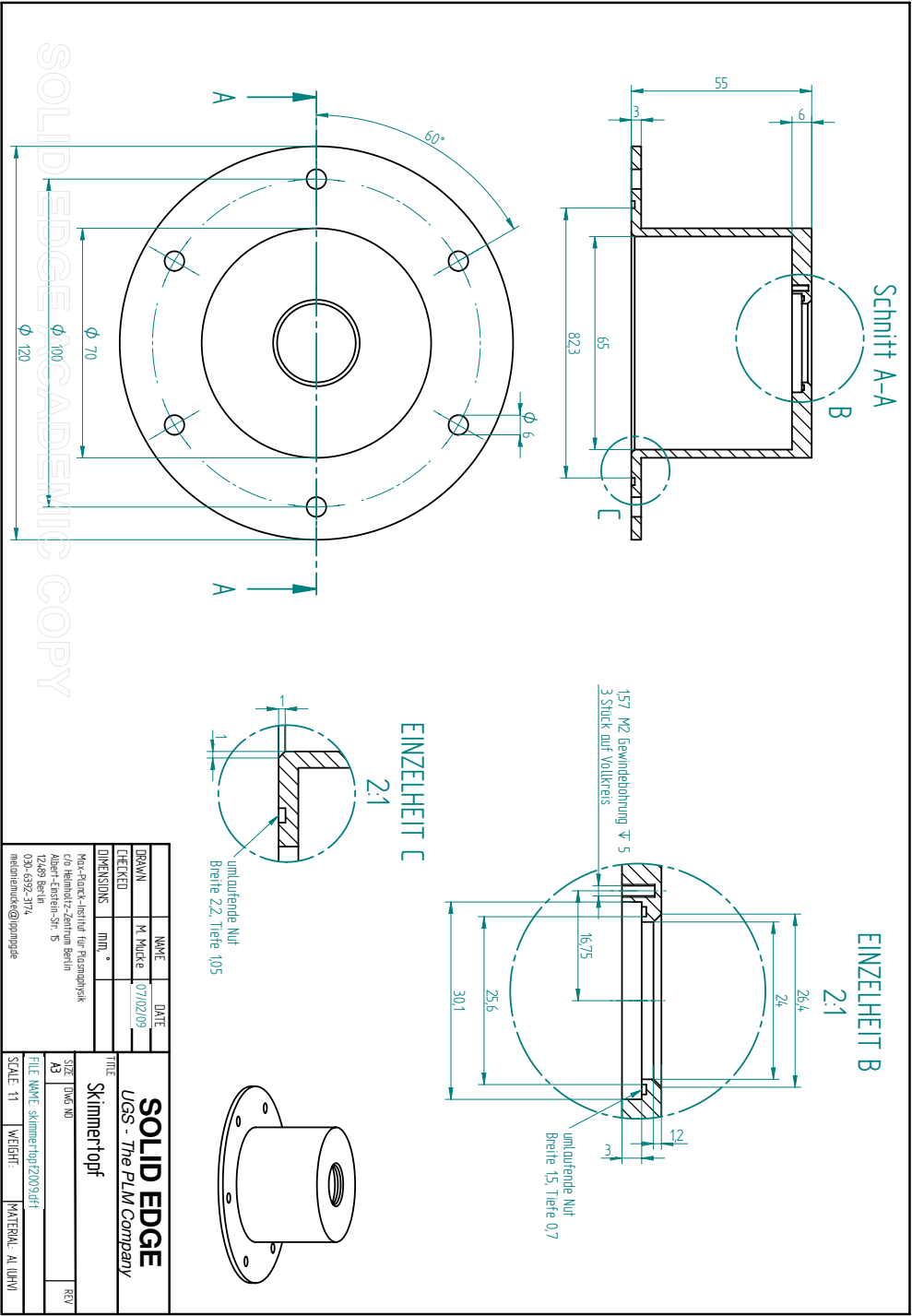


Figure A.29: Skimmer holding construction to create a wall between expansion and main chamber and to allow alignment of the skimmer.





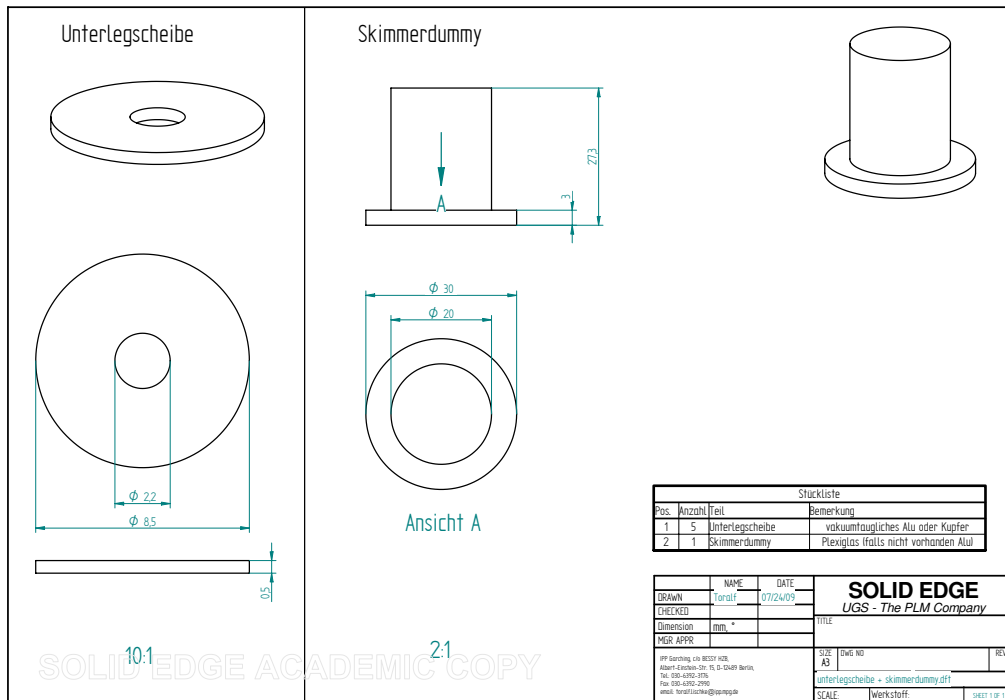


Figure A.30: Skimmer dummy to measure maximum possible shift of cluster source.

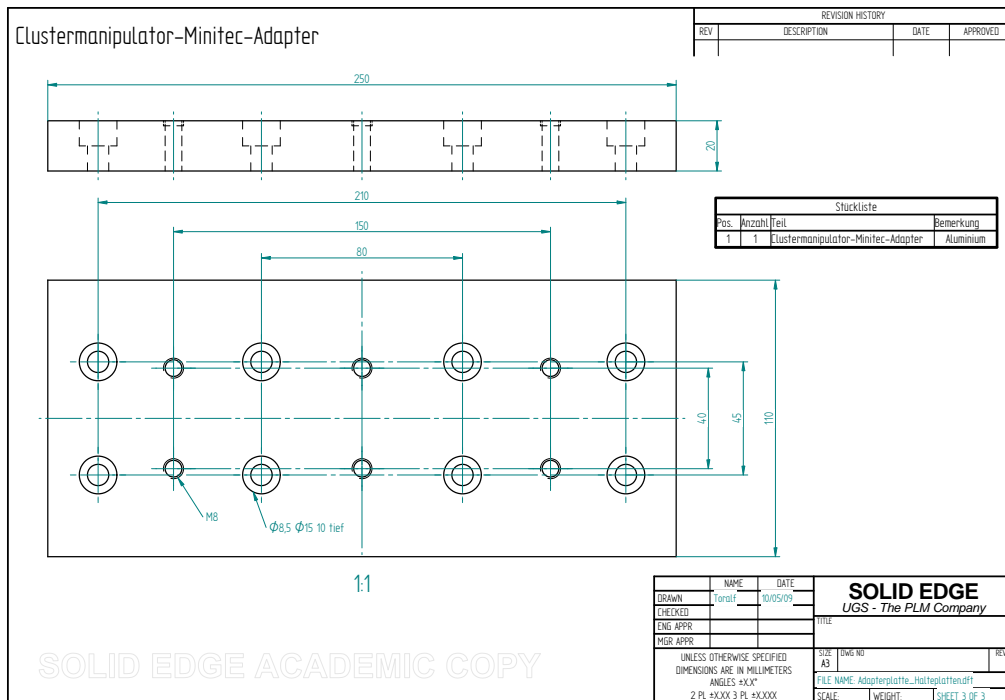


Figure A.31: Plate to fix cluster manipulator support onto minitec frame.

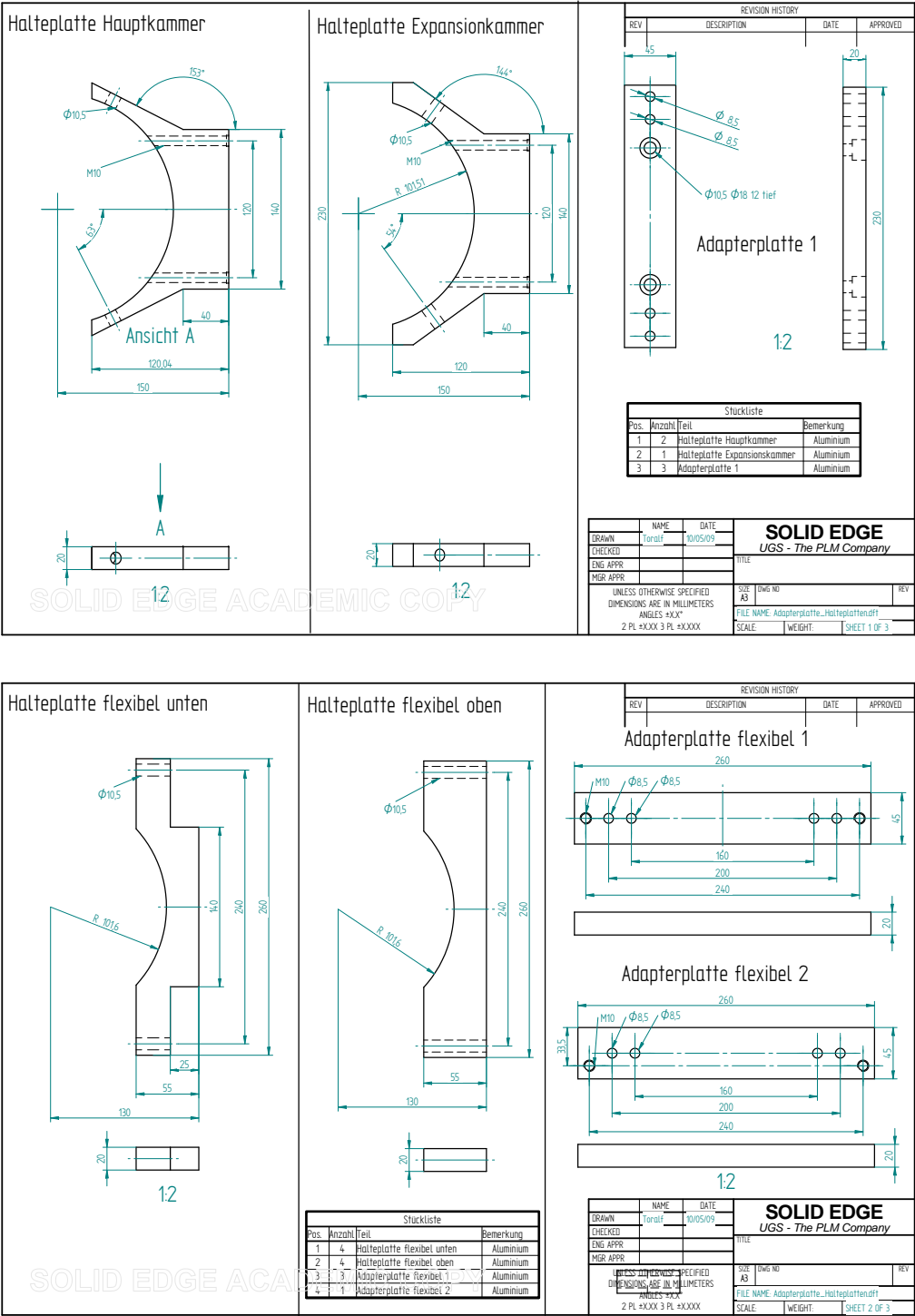


Figure A.32: Mounting plates to fix chamber onto minitec frame.

# references

- [1] H. Hertz, *Über einen Einfluss des ultravioletten Lichtes auf die electrische Entladung*, Ann. Phys. **267** (8), 983–1000, 1887.
- [2] W. Hallwachs, *Über den Einfluss des Lichtes auf electrostatisch geladene Körper*, Ann. Phys. **269** (2), 301–312, 1888.
- [3] P. Lenard, *Über die lichtelektrische Wirkung*, Ann. Phys. **313** (5), 149–198, 1902.
- [4] A. Einstein, *Über einen die Erzeugung und Verwandlung des Lichtes betreffenden heuristischen Gesichtspunkt*, Ann. Phys. **322** (6), 132–148, 1905.
- [5] T. Koopmans, *Über die Zuordnung von Wellenfunktionen und Eigenwerten zu den einzelnen Elektronen eines Atoms*, Physica **1**, 104–113, 1933.
- [6] P. W. Fowler, C. M. Quinn, and D. B. Redmond, *Decorated fullerenes and model structures for water clusters*, J. Chem. Phys. **95** (10), 7678–7681, 1991.
- [7] O. Björneholm, F. Federmann, S. Kakar, and T. Möller, *Between vapor and ice: Free water clusters studied by core level spectroscopy*, J. Chem. Phys. **111** (2), 546–550, 1999.
- [8] A. Lindblad, *A treatise on the geometric and electronic structure of clusters investigated by synchrotron radiation based electron spectroscopies*, PhD thesis, Uppsala Universitet, 2008, Digital Comprehensive Summaries of Uppsala Dissertations from the Faculty of Science and Technology 393. ISBN 978-91-554-7095-1.
- [9] O. Echt, K. Sattler, and E. Recknagel, *Magic numbers for sphere packings: Experimental verification in free xenon clusters*, Phys. Rev. Lett. **47** (16), 1121–1124, 1981.
- [10] H. Haberland, *Clusters of atoms and molecules. theory, experiment, and clusters of atoms* vol. 52 of *Springer Series in Chemical Physics*, Springer Verlag, 1994.

- [11] S. Maruyama, L. R. Anderson, and R. E. Smalley, *Direct injection supersonic clusters beam source for FT-ICR studies of clusters*, Rev. Sci. Instrum. **61** (12), 3686–3693, 1990.
- [12] M. H. Allen and M. L. Vestal, *Design and performance of a novel electrospray interface*, J. Am. Soc. Mass Spectrom. **3**, 18–26, 1992.
- [13] O. F. Hagena and W. Obert, *Cluster formation in expanding supersonic jets: Effect of pressure, temperature, nozzle size, and test gas*, J. Chem. Phys. **56** (5), 1793–1802, 1972.
- [14] D. R. Miller, *Atomic and molecular beam methods*, Number 3181. Oxford University Press, 1988.
- [15] H. Vach, *Impurity dynamics in binary van der Waals clusters created by pick-up*, J. Chem. Phys. **111** (8), 3536–3547, 1999.
- [16] M. Tchapyguine, M. Lundwall, M. Gisselbrecht, G. Öhrwall, R. Feifel, S. Sorensen, S. Svensson, N. Mårtensson, and O. Björneholm, *Variable surface composition and radial interface formation in self-assembled free, mixed Ar/Xe clusters*, Phys. Rev. A **69**, 031201, 2004.
- [17] A. Lindblad, H. Bergersen, T. Rander, M. Lundwall, G. Öhrwall, M. Tchapyguine, S. Svensson, and O. Björneholm, *The far from equilibrium structure of argon clusters doped with krypton or xenon*, Phys. Chem. Chem. Phys. **8**, 1899–1905, 2006.
- [18] O. F. Hagena, *Condensation in free jets: Comparison of rare gases and metals*, Z. Phys. D **4**, 291–299, 1987.
- [19] U. Buck and R. Krohne, *Cluster size determination from diffractive He atom scattering*, J. Chem. Phys. **105** (13), 5408–5415, 1996.
- [20] C. Bobbert, S. Schütte, C. Steinbach, and U. Buck, *Fragmentation and reliable size distributions of large ammonia and water clusters*, Eur. Phys. J. D. **19**, 183–192, 2002.
- [21] *CRC chemistry*, chapter 6.
- [22] V. Schmidt, *Electron spectrometry of atoms using synchrotron radiation* vol. 6 of *Cambridge Monographs on Atomic, Molecular and Chemical Physics*, Cambridge University Press, 1997.
- [23] K.-N. Huang, *Theory of angular distribution and spin polarization of photoelectrons*, Phys. Rev. A **22** (1), 223–239, 1980.

- 
- [24] B. Krässig, M. Jung, D. S. Gemmell, E. P. Kanter, T. LeBrun, S. H. Southworth, and L. Young, *Nondipolar asymmetries of photoelectron angular distributions*, Phys. Rev. Lett. **75** (26), 4736–4739, 1995.
- [25] S. Barth, *Untersuchung des Interatomaren Coulomb-Zerfalls in schwach gebundenen Systemen*, PhD thesis, TU Berlin, 2007.
- [26] A. Kikas, S. J. Osborne, A. Ausmees, S. Svensson, O.-P. Sairanen, and S. Aksela, *High-resolution study of the correlation satellites in photoelectron spectra of the rare gases*, J. Electron Spectros. Relat. Phenom. **77**, 241–266, 1996.
- [27] S. Joshi, S. Barth, S. Marburger, V. Ulrich, and U. Hergenhahn, *2p correlation satellites in neon clusters investigated by photoemission*, Phys. Rev. B **73**, 235404, 2006.
- [28] O. Björneholm, F. Federmann, F. Föcking, T. Möller, and P. Stampfli, *Core level binding energy shifts and polarization screening: A combined experimental and theoretical study of argon clusters*, J. Chem. Phys. **104**, 1846–1854, 1996.
- [29] U. Hergenhahn, S. Barth, V. Ulrich, M. Mucke, S. Joshi, T. Lischke, A. Lindblad, T. Rander, G. Öhrwall, and O. Björneholm, *3p valence photoelectron spectrum of Ar clusters*, Phys. Rev. B **79**, 155448, 2009.
- [30] P. Tsai, Bilin and J. H. D. Eland, *Mass spectra and doubly charged ions in photoionization at 30.4 nm and 58.4 nm*, Int. J. Mass Spectrom. Ion Phys. **36**, 143–165, 1980.
- [31] T. Pattard, T. Schneider, and R. J. M., *On the role of shake-off in single-photon double ionization*, J. Phys. B: At. Mol. Opt. Phys. **36**, L189–L195, 2003.
- [32] J. H. D. Eland, *Complete double photoionisation spectra of small molecules from TOF-PEPECO measurements*, Chem. Phys. **294**, 171–186, 2003.
- [33] C. Bréchnignac, M. Broyer, P. Cahuzac, G. Delacretaz, P. Labastie, and L. Wöste, *Single-photon double ionization of mercury clusters using synchrotron radiation*, Chem. Phys. Lett. **133** (1), 45–48, 1987.
- [34] U. Hergenhahn, A. Kolmakov, M. Riedler, A. R. B. de Castro, O. Löfken, and T. Möller, *Observation of excitonic satellites in the photoelectron spectra of Ne and Ar clusters*, Chem. Phys. Lett. **351**, 235–241, 2002.
- [35] M. Göppert-Mayer, *Über Elementarakte mit zwei Quantensprüngen*, Ann. Phys. **401**, 273–294, 1931.

- 
- [36] H. Wabnitz, L. Bittner, A. R. B. de Castro, R. Döhrmann, P. Gürtler, T. Laarmann, W. Laasch, J. Schulz, A. Swiderski, K. von Haefen, T. Möller, B. Faatz, A. Fateev, J. Feldhaus, C. Gerth, U. Hahn, E. Saldin, E. Schneidmiller, K. Sytchev, K. Tiedtke, R. Treusch, and M. Yurkov, *Multiple ionization of atom clusters by intense soft X-rays from a free-electron laser*, Nature **420**, 482–485, 2002.
- [37] H. Wabnitz, A. R. B. de Castro, P. Gürtler, T. Laarmann, W. Laasch, J. Schulz, and T. Möller, *Multiple ionization of rare gas atoms irradiated with intense VUV radiation*, Phys. Rev. Lett. **94**, 023001, 2005.
- [38] P. Auger, *Sur l'effet photoélectrique composé*, J. Phys. Radium **6**, 205–208, 1925.
- [39] K. Ueda, H. Fukuzawa, X.-J. Liu, K. Sakai, G. Prümper, Y. Morishita, N. Saito, I. H. Suzuki, K. Nagaya, H. Iwayama, M. Yao, K. Kreidi, M. Schöffler, T. Jahnke, S. Schössler, R. Dörner, T. Weber, J. Harries, and Y. Tamenori, *Interatomic Coulombic decay following the Auger decay: Experimental evidence in rare-gas dimers*, J. Electron Spectros. Relat. Phenom. **166-167**, 3–10, 2008.
- [40] F. Tarantelli and L. S. Cederbaum, *Foreign imaging in Auger spectroscopy: The Si 2p spectrum of silicon tetrafluoride*, Phys. Rev. Lett. **71** (4), 649–652, 1993.
- [41] S. Sheinerman, P. Lablanquie, F. Penent, J. Palaudoux, J. H. D. Eland, T. Aoto, Y. Hikosaka, and K. Ito, *Electron correlation in Xe 4d Auger decay studied by slow photoelectron-Auger electron coincidence spectroscopy*, J. Phys. B: At. Mol. Opt. Phys. **39**, 1017–1033, 2006.
- [42] U. Hergenhahn, A. De Fanis, G. Prümper, A. K. Kazansky, N. M. Kabachnik, and K. Ueda, *A study of photoelectron recapture due to post-collision interaction in Ne at the 1s photoionization threshold*, J. Phys. B: At. Mol. Opt. Phys. **38**, 2843–2857, 2005.
- [43] P. Lablanquie, S. Sheinerman, F. Penent, R. I. Hall, M. Ahmad, Y. Hikosaka, and K. Ito, *Dynamics and post-collision interaction effects in two electron decay from the xenon 4d hole*, Phys. Rev. Lett. **87** (5), 053001, 2001.
- [44] M. Y. Kuchiev and S. A. Sheinerman, *The post collision interaction in the inner-shell photoionisation of Ar and Xe*, J. Phys. B: At. Mol. Opt. Phys. **18**, L551–L556, 1985.

- 
- [45] N. Scherer, H. Lörch, T. Kerkau, and V. Schmidt, *Postcollision interaction in the coincident emission of photoelectrons and Auger electrons at small relative angles*, Phys. Rev. Lett. **82** (23), 4615–4618, 1999.
  - [46] N. Scherer, H. Lörch, T. Kerkau, and V. Schmidt, *Exchange interference between coincident photoelectrons and Auger electrons*, J. Phys. B: At. Mol. Opt. Phys. **34**, L339–L344, 2001.
  - [47] H. Ishii, Y. Iketaki, T. Watabe, T. Takayanagi, K. Wakiya, H. Suzuki, and F. Koike, *Post-collision interaction in Auger-electron emission of rare-gas atoms following electron-impact ionization*, Phys. Rev. A **43** (1), 134–142, 1991.
  - [48] A. Lindblad, R. F. Fink, H. Bergersen, M. Lundwall, T. Rander, R. Feifel, G. Öhrwall, M. Tchapyguine, U. Hergenhahn, S. Svensson, and O. Björneholm, *Postcollision interaction in noble gas clusters: Observation of differences in surface and bulk line shapes*, J. Chem. Phys. **123**, 211101, 2005.
  - [49] L. S. Cederbaum, J. Zobeley, and F. Tarantelli, *Giant intermolecular decay and fragmentation of clusters*, Phys. Rev. Lett. **79** (24), 4778–4781, 1997.
  - [50] S. Marburger, O. Kugeler, U. Hergenhahn, and T. Möller, *Experimental evidence for interatomic Coulombic decay in Ne clusters*, Phys. Rev. Lett. **90** (20), 203401, 2003.
  - [51] U. Hergenhahn, *Interatomic and intermolecular Coulombic decay: The early years*, J. Electron Spectros. Relat. Phenom. page accepted, 2011.
  - [52] J. Zobeley, R. Santra, and L. S. Cederbaum, *Electronic decay in weakly bound heteroclusters: Energy transfer versus electron transfer*, J. Chem. Phys. **115** (11), 5076–5088, 2001.
  - [53] R. Santra and L. S. Cederbaum, *Non-hermitian electronic theory and applications to clusters*, Phys. Rep. **368**, 1–117, 2002.
  - [54] N. Moiseyev, R. Santra, J. Zobeley, and L. S. Cederbaum, *Fingerprints of the nodal structure of autoionizing vibrational wave functions in clusters: Interatomic Coulombic decay in Ne dimer*, J. Chem. Phys. **114** (17), 7351–7360, 2001.
  - [55] S. Scheit, L. S. Cederbaum, and H.-D. Meyer, *Time-dependent interplay between electron emission and fragmentation in the interatomic Coulombic decay*, J. Chem. Phys. **118** (5), 2092–2107, 2003.
  - [56] S. Scheit, V. Averbukh, H.-D. Meyer, N. Moiseyev, R. Santra, T. Sommerfeld, J. Zobeley, and L. S. Cederbaum, *On the interatomic Coulombic decay in the Ne dimer*, J. Chem. Phys. **121**, 8393–8398, 2004.



- 
- [57] K. Harth, M. Raab, and H. Hotop, *Odd Rydberg spectrum of  $^{20}\text{NeI}$ : High resolution laser spectroscopy and multichannel quantum defect theory analysis*, Z. Phys. D **7**, 213–225, 1987.
- [58] W. Persson, *The spectrum of singly ionized neon, Ne II*, Phys. Scripta **3**, 133–155, 1971.
- [59] S. M. Cybulski and R. R. Toczyłowski, *Ground state potential energy curves for  $\text{He}_2$ ,  $\text{Ne}_2$ ,  $\text{Ar}_2$ ,  $\text{He-Ne}$ ,  $\text{He-Ar}$ , and  $\text{Ne-Ar}$ : A coupled-cluster study*, J. Chem. Phys. **111** (23), 10520–10528, 1999.
- [60] J. A. D. Matthew and Y. Komninos, *Transition rates for interatomic Auger processes*, Surf. Sci. **53**, 716–725, 1975.
- [61] V. Averbukh, I. B. Müller, and L. S. Cederbaum, *Mechanism of interatomic Coulombic decay in clusters*, Phys. Rev. Lett. **93**, 263002, 2004.
- [62] G. Öhrwall, M. Tchapyguine, M. Lundwall, R. Feifel, H. Bergersen, T. Rander, A. Lindblad, J. Schulz, S. Peredkov, S. Barth, S. Marburger, U. Hergenhahn, S. Svensson, and O. Björneholm, *Femtosecond interatomic Coulombic decay in free neon clusters: Large lifetime differences between surface and bulk*, Phys. Rev. Lett. **93** (17), 173401, 2004.
- [63] T. Jahnke, A. Czasch, M. S. Schöffler, S. Schössler, A. Knapp, M. Kász, J. Titze, C. Wimmer, K. Kreidi, R. E. Grisenti, A. Staudte, O. Jagutzki, U. Hergenhahn, H. Schmidt-Böcking, and R. Dörner, *Experimental observation of interatomic Coulombic decay in neon dimers*, Phys. Rev. Lett. **93** (16), 163401, 2004.
- [64] S. Barth, S. Marburger, S. Joshi, V. Ulrich, O. Kugeler, and U. Hergenhahn, *Interface identification by non-local autoionization transitions*, Phys. Chem. Chem. Phys. **8**, 3218–3222, 2006.
- [65] M. Lundwall, W. Pokapanich, H. Bergersen, A. Lindblad, T. Rander, G. Öhrwall, M. Tchapyguine, S. Barth, U. Hergenhahn, S. Svensson, and O. Björneholm, *Self-assembled heterogeneous argon/neon core-shell clusters studied by photoelectron spectroscopy*, J. Chem. Phys. **126**, 214706, 2007.
- [66] T. Arion, M. Mucke, M. Förstel, A. M. Bradshaw, and U. Hergenhahn, *Interatomic Coulombic decay in mixed Ne-Kr clusters*, J. Chem. Phys. **134** (7), 074306, 2011.
- [67] R. Santra, J. Zobeley, and L. S. Cederbaum, *Electronic decay of valence holes in clusters and condensed matter*, Phys. Rev. B **64**, 245104, 2001.
- [68] G. B. Armen, H. Aksela, T. Åberg, and S. Aksela, *The resonant Auger effect*, J. Phys. B: At. Mol. Opt. Phys. **33**, R49–R92, 2000.

- 
- [69] M. N. Piancastelli, *Auger resonant Raman studies of atoms and molecules*, J. Electron Spectros. Relat. Phenom. **107**, 1–26, 2000.
- [70] K. Gokhberg, V. Averbukh, and L. S. Cederbaum, *Interatomic decay of inner-valence-excited states in clusters*, J. Chem. Phys. **124**, 144315, 2006.
- [71] S. Barth, S. Joshi, S. Marburger, V. Ulrich, A. Lindblad, G. Öhrwall, O. Björneholm, and U. Hergenhahn, *Observation of resonant interatomic Coulombic decay in Ne clusters*, J. Chem. Phys. **122**, 241102, 2005.
- [72] T. Aoto, K. Ito, Y. Hikosaka, E. Shigemasa, F. Penent, and P. Lablanquie, *Properties of resonant interatomic Coulombic decay in Ne dimers*, Phys. Rev. Lett. **97**, 243401, 2006.
- [73] R. Santra and L. S. Cederbaum, *Coulombic energy transfer and triple ionization in clusters*, Phys. Rev. Lett. **90** (15), 153401, 2003.
- [74] R. Santra and L. S. Cederbaum, *Erratum: Coulombic energy transfer and triple ionization in clusters*, Phys. Rev. Lett. **94**, 199901, 2005.
- [75] Y. Morishita, X.-J. Liu, N. Saito, T. Lischke, M. Kato, G. Prümper, M. Oura, H. Yamaoka, Y. Tamenori, I. H. Suzuki, and K. Ueda, *Experimental evidence of interatomic Coulombic decay from the Auger final states in argon dimers*, Phys. Rev. Lett. **96**, 243402, 2006.
- [76] X.-J. Liu, N. Saito, H. Fukuzawa, Y. Morishita, S. Stoychev, A. Kuleff, I. H. Suzuki, Y. Tamenori, R. Richter, G. Prümper, and K. Ueda, *Evidence of sequential interatomic decay in argon trimers obtained by electron-triple-ion coincidence spectroscopy*, J. Phys. B: At. Mol. Opt. Phys. **40**, F1–F7, 2007.
- [77] Y. Morishita, N. Saito, I. H. Suzuki, H. Fukuzawa, X.-J. Liu, K. Sakai, G. Prümper, K. Ueda, H. Iwayama, K. Nagaya, M. Yao, K. Kreidi, M. Schöffler, T. Jahnke, S. Schössler, R. Dörner, T. Weber, J. Harries, and Y. Tamenori, *Evidence of interatomic Coulombic decay in ArKr after Ar 2p Auger decay*, J. Phys. B: At. Mol. Opt. Phys. **41**, 025101, 2008.
- [78] J. Viefhaus, S. Cvejanović, B. Langer, T. Lischke, G. Prümper, D. Rolles, A. V. Golovin, A. N. Grum-Grzhimailo, N. M. Kabachnik, and U. Becker, *Energy and angular distributions of electrons emitted by direct double Auger decay*, Phys. Rev. Lett. **92** (8), 83001, 2004.
- [79] J. Viefhaus, M. Braune, S. Korica, A. Reinköster, D. Rolles, and U. Becker, *Auger cascades versus direct double Auger: relaxation processes following photoionization of the Kr 3d and Xe 4d, 3d inner shells*, J. Phys. B: At. Mol. Opt. Phys. **38**, 3885–3903, 2005.

- 
- [80] P. Lablanquie, L. Andric, J. Palaudoux, U. Becker, M. Braune, J. Vieffhaus, J. H. D. Eland, and F. Penent, *Multielectron spectroscopy: Auger decays of the argon 2p hole*, J. Electron Spectros. Relat. Phenom. **156-158**, 51–57, 2007.
- [81] K. Sakai, S. Stoychev, T. Ouchi, I. Higuchi, M. Schöffler, T. Mazza, H. Fukuzawa, K. Nagaya, M. Yao, Y. Tamenori, A. I. Kuleff, N. Saito, and K. Ueda, *Electron-transfer-mediated decay and interatomic Coulombic decay from the triply ionized states in argon dimers*, Phys. Rev. Lett. **106**, 033401, 2011.
- [82] J. Titze, M. S. Schöffler, H.-K. Kim, F. Trinter, M. Waitz, J. Voigtsberger, N. Neumann, B. Ulrich, K. Kreidi, R. Wallauer, M. Odenweller, T. Havermeier, S. Schössler, M. Meckel, L. Foucar, T. Jahnke, A. Czasch, L. P. H. Schmidt, O. Jagutzki, R. E. Grisenti, H. Schmidt-Böcking, H. J. Lüdde, and R. Dörner, *Ionization dynamics of helium dimers in fast collisions with  $He^{++}$* , Phys. Rev. Lett. **106**, 033201, 2011.
- [83] I. B. Müller and L. S. Cederbaum, *Electronic decay following ionization of aqueous  $Li^+$  microsolvation clusters*, J. Chem. Phys. **122**, 094305, 2005.
- [84] M. Förstel, M. Mucke, T. Arion, A. M. Bradshaw, and U. Hergenhahn, *Autoionization mediated by electron transfer*, Phys. Rev. Lett. **106** (3), 33402, 2011.
- [85] M. Mucke, M. Braune, S. Barth, M. Förstel, T. Lischke, V. Ulrich, T. Arion, U. Becker, A. Bradshaw, and U. Hergenhahn, *A hitherto unrecognized source of low-energy electrons in water*, Nature Phys. **6**, 143–146, 2010.
- [86] H. Wiedemann, *Synchrotron radiation*, Advanced Texts in Physics. Springer Verlag, Berlin, Heidelberg, New York, 2003.
- [87] V. Ulrich, *Untersuchung von Autoionisationsprozessen in kleinen Molekülen und Clustern mittels hochauflösender Elektronen-Koinzidenzspektroskopie*, PhD thesis, TU Berlin, 2007.
- [88] H. Wiedemann, Synchrotron radiation primer, online 1998.
- [89] S. Sasaki, K. Kakuno, T. Takada, T. Shimada, K.-i. Yanagida, and Y. Miyahara, *Design of a new type of planar undulator for generating variably polarized radiation*, Nucl. Instrum. Methods Phys. Res. A **331**, 763–767, 1993.
- [90] S. Sasaki, *Analysis for a planar variably-polarizing undulator*, Nucl. Instrum. Methods Phys. Res. A **347**, 83–86, 1994.

- 
- [91] P. Kruit and F. H. Read, *Magnetic field paralleliser for  $2\pi$  electron-spectrometer and electron-image magnifier*, J. Phys. E: Sci. Instrum. **16**, 313–324, 1983.
- [92] T. Tsuboi, E. Y. Xu, Y. K. Bae, and K. T. Gillen, *Magnetic bottle electron spectrometer using permanent magnets*, Rev. Sci. Instrum. **59** (8), 1357–1362, 1988.
- [93] K. Rademann, T. Rech, B. Kaiser, U. Even, and F. Hensel, *A new coincidence technique for vacuum ultraviolet photoelectron spectroscopy of neutral clusters in a molecular beam*, Rev. Sci. Instrum. **62** (8), 1932–1941, 1991.
- [94] H. Handschuh, G. Ganteför, and W. Eberhardt, *Vibrational spectroscopy of clusters using a "magnetic bottle"*, Rev. Sci. Instrum. **66** (7), 3838–3843, 1995.
- [95] T. Ohdaira, R. Suzuki, T. Mikado, H. Ohgaki, M. Chiwaki, and T. Yamazaki, *An apparatus for high-resolution positron-annihilation induced Auger-electron spectroscopy using a time-of-flight technique*, Appl. Surf. Sci. **116**, 177–180, 1997.
- [96] C. Lüder and K. H. Meiwes-Broer, *Electron detachment energies of  $Pb_n^-$  ( $n = 24 - 204$ ) determined in a simple magnetic bottle photoelectron spectrometer*, Chem. Phys. Lett. **294**, 391–396, 1998.
- [97] F. Penent, P. Lablanquie, R. I. Hall, J. Palaudoux, K. Ito, Y. Hikosaka, T. Aoto, and J. H. D. Eland, *Coincidence Auger spectroscopy*, J. Electron Spectros. Relat. Phenom. **144-147**, 7–11, 2005.
- [98] K. L. J. Knappenberger, C. E. J. Jones, M. A. Sobhy, and A. W. J. Castleman, *Versatile cluster based photoelectron spectrometer*, Rev. Sci. Instrum. **77**, 123901, 2006.
- [99] J. H. D. Eland, O. Vieuxmaire, T. Kinugawa, P. Lablanquie, R. I. Hall, and F. Penent, *Complete two-electron spectra in double photoionization: The rare gases Ar, Kr, and Xe*, Phys. Rev. Lett. **90** (5), 053003, 2003.
- [100] J. L. Wiza, *Microchannel plate detectors*, Nucl. Instrum. Methods **162**, 587–601, 1979.
- [101] S. P. Marburger, *Experimentelle Untersuchungen zum Interatomaren Coulomb Zerfall an Neon Clustern: Nachweis eines ultraschnellen nicht-lokalen Zerfallskanals*, PhD thesis, TU Berlin, 2004.
- [102] N. Vaval and L. S. Cederbaum, *Ab initio lifetimes in the interatomic Coulombic decay of neon clusters computed with propagators*, J. Chem. Phys. **126**, 164110, 2007.

- 
- [103] S. D. Stoychev, A. I. Kuleff, F. Tarantelli, and L. S. Cederbaum, *On the interatomic electronic processes following Auger decay in neon dimer*, J. Chem. Phys. **129**, 074307, 2008.
- [104] T. Jahnke, A. Czasch, M. Schöffler, S. Schössler, M. Kász, J. Titze, K. Kreidi, R. E. Grisenti, A. Staudte, O. Jagutzki, L. P. H. Schmidt, S. K. Semenov, N. A. Cherepkov, H. Schmidt-Böcking, and R. Dörner, *Photoelectron and ICD electron angular distributions from fixed-in-space neon dimers*, J. Phys. B: At. Mol. Opt. Phys. **40**, 2597–2606, 2007.
- [105] A. M. Dias, *Study of electronic transitions by interatomic Coulombic decay in neon dimer*, Physica B **403**, 3490–3494, 2008.
- [106] T. Jahnke, A. Czasch, M. Schöffler, S. Schössler, M. Kász, J. Titze, K. Kreidi, R. E. Grisenti, A. Staudte, O. Jagutzki, L. P. H. Schmidt, T. Weber, H. Schmidt-Böcking, K. Ueda, and R. Dörner, *Experimental separation of virtual photon exchange and electron transfer in interatomic Coulombic decay of neon dimers*, Phys. Rev. Lett. **99**, 153401, 2007.
- [107] S. Barth, S. Marburger, O. Kugeler, V. Ulrich, S. Joshi, A. M. Bradshaw, and U. Hergenhahn, *The efficiency of interatomic Coulombic decay in Ne clusters*, Chem. Phys. **329**, 246–250, 2006.
- [108] P. Bolognesi, L. Avaldi, D. R. Cooper, M. Coreno, R. Camilloni, and G. C. King, *High-resolution threshold photoelectron measurements of the  $\text{Ne}^+ 2p^4nl$  satellite states*, J. Phys. B: At. Mol. Opt. Phys. **35**, 2927–2948, 2002.
- [109] A. Knop, H. W. Jochims, A. L. D. Kilcoyne, A. P. Hitchcock, and E. Rühl, *Zero-kinetic-energy photoelectron spectroscopy of  $\text{Ar}(2p)$ -excited argon clusters*, Chem. Phys. Lett. **223**, 553–560, 1994.
- [110] L. S. Cederbaum, private communication 2010.
- [111] J. F. Ogilvie and F. Y. H. Wang, *Potential-energy functions of diatomic molecules of the noble gases i. like nuclear species*, J. Mol. Struct. **273**, 277–290, 1992.
- [112] J. F. Ogilvie and F. Y. H. Wang, *Potential-energy functions of diatomic molecules of the noble gases ii. unlike nuclear species*, J. Mol. Struct. **291**, 313–322, 1993.
- [113] D. C. Patton and M. R. Pederson, *A theoretical study of rare-gas diatomic molecules with the generalized-gradient approximation to density functional theory*, Int. J. Q. Chem. **69**, 619–627, 1998.

- 
- [114] L. O. Werme, T. Bergmark, and K. Siegbahn, *The high resolution  $L_{2,3}MM$  and  $M_{4,5}NN$  Auger spectra from krypton and  $M_{4,5}NN$  and  $N_{4,5}OO$  Auger spectra from xenon*, Phys. Scripta **6**, 141–150, 1972.
  - [115] S. Peredkov, A. Kivimäki, S. L. Sorensen, J. Schulz, N. Mårtensson, , G. Öhrwall, M. Lundwall, T. Rander, A. Lindblad, H. Bergersen, S. Svensson, O. Björneholm, and M. Tchapyguine, *Ioniclike energy structure of neutral core-excited states in free Kr clusters*, Phys. Rev. A **72**, 021201 (R), 2005.
  - [116] L. Avaldi, G. Dawber, N. Gulley, H. Rojas, G. C. King, R. Hall, M. Stuhel, and M. Zitnik, *A study of  $Ne^{2+}$  and  $Ar^{2+}$  satellite states observed by ‘threshold photoelectrons coincidence’ spectroscopy*, J. Phys. B: At. Mol. Opt. Phys. **30**, 5197–5212, 1997.
  - [117] M. Lundwall, H. Bergersen, A. Lindblad, G. Öhrwall, M. Tchapyguine, S. Svensson, and O. Björneholm, *Preferential site occupancy observed in coexpanded argon-krypton clusters*, Phys. Rev. A **74**, 043206, 2006.
  - [118] O. Björneholm, F. Federmann, F. Föcking, and T. Möller, *Core level photoelectron and x-ray absorption spectroscopy of free argon clusters: Size-dependent energy shifts and determination of surface atom coordination*, Phys. Rev. Lett. **74** (15), 3017–3020, 1995.
  - [119] E. Faßhauer, N. V. Kryzhevoi, and M. Pernpointner, *Possible electronic decay channels in the ionization spectra of small clusters composed of Ar and Xe: A four-component relativistic treatment*, J. Chem. Phys. **133**, 014303, 2010.
  - [120] E. Faßhauer, *Untersuchung elektronischer Zerfallsreaktionen kleiner, inner-valent ionisierter Edelgascluster mit Methoden der relativistischen Quantenchemie*, Diplomarbeit, Ruprecht-Karls-Universität Heidelberg 2009.
  - [121] E. Faßhauer, private communication 2010.
  - [122] anomalous properties of water, <http://www.lsbu.ac.uk/water/anmlies.html>.
  - [123] S. Ashihara, N. Huse, A. Espagne, E. T. J. Nibbering, and T. Elsaesser, *Ultrafast structural dynamics of water induced by dissipation of vibrational energy*, J. Phys. Chem. A **111** (5), 743–746, 2007.
  - [124] J. Zobeley, L. S. Cederbaum, and F. Tarantelli, *Intermolecular Coulombic decay of molecular clusters: Identification of the decay mechanism using a new hole-population analysis*, J. Phys. Chem. A **103** (50), 11145–11160, 1999.

- [125] J. H. D. Eland, *Double photoionisation spectra of methane, ammonia and water*, Chem. Phys. **323**, 391–396, 2006.
- [126] M. S. Banna, B. H. McQuaide, R. Malutzki, and V. Schmidt, *The photoelectron spectrum of water in the 30–140 eV photon energy range*, J. Chem. Phys. **84** (9), 4739–4744, 1986.
- [127] I. B. Müller and L. S. Cederbaum, *Ionization and double ionization of small water clusters*, J. Chem. Phys. **125**, 204305, 2006.
- [128] B. Winter, R. Weber, W. Widdra, M. Dittmar, M. Faubel, and I. V. Hertel, *Full valence band photoemission from liquid water using EUV synchrotron radiation*, J. Phys. Chem. A **108**, 2625–2632, 2004.
- [129] V. Buch, S. Bauerecker, J. P. Devlin, U. Buck, and J. K. Kazimirski, *Solid water clusters in the size range of tens-thousands of  $H_2O$ : a combined computational/spectroscopic outlook*, Int. Rev. Phys. Chem. **23** (3), 375–433, 2004.
- [130] S. Barth, M. Ončák, V. Ulrich, M. Mucke, T. Lischke, P. Slavíček, and U. Hergenbahn, *Valence ionization of water clusters: From isolated molecules to bulk*, J. Phys. Chem. A **113** (48), 13519–13527, 2009.
- [131] S. Y. Truong, A. J. Yench, A. M. Juarez, S. J. Cavanagh, P. Bolognesi, and G. C. King, *Threshold photoelectron spectroscopy of  $H_2O$  and  $D_2O$  over the photon energy range 12–40 eV*, Chem. Phys. **355**, 183–193, 2009.
- [132] T. Jahnke, H. Sann, T. Havermeier, K. Kreidi, C. Stuck, M. Meckel, M. Schöffler, N. Neumann, R. Wallauer, S. Voss, A. Czasch, O. Jagutzki, A. Malakzadeh, F. Afaneh, T. Weber, H. Schmidt-Böcking, and R. Dörner, *Ultrafast energy transfer between water molecules*, Nature Phys. **6**, 139–142, 2010.
- [133] A. I. Kuleff and L. S. Cederbaum, *Tracing ultrafast interatomic electronic decay processes in real time and space*, Phys. Rev. Lett. **98**, 083201, 2007.
- [134] O. Vendrell, S. D. Stoychev, and L. S. Cederbaum, *Generation of highly damaging  $H_2O^+$  radicals by inner valence shell ionisation of water*, Chem. Phys. Chem. **11**, 1006–1009, 2010.
- [135] A. Furuhashi, M. Dupuis, and K. Hirao, *Reactions associated with ionization in water: A direct ab initio dynamics study of ionization in  $(H_2O)_{17}$* , J. Chem. Phys. **124**, 164310, 2006.
- [136] J. F. Ward, *The complexity of DNA damage: relevance to biological consequences*, Int. J. Radiat. Biol. **66** (5), 427–432, 1994.

- [137] M. Folkard, K. M. Prise, B. Vojnovic, S. Davies, M. J. Roper, and B. D. Michael, *Measurement of DNA damage by electrons with energies between 25 and 4000 ev*, Int. J. Radiat. Biol. **64** (6), 651–658, 1993.
- [138] S. M. Pimblott and J. A. La Verne, *Production of low-energy electrons by ionizing radiation*, Rad. Phys. Chem. **76**, 1244–1247, 2007.
- [139] B. D. Michael and P. O'Neill, *Molecular biology: A sting in the tail of electron tracks*, Science **287** (5458), 1603–1604, 2000.
- [140] B. Boudaïffa, P. Cloutier, D. Hunting, M. A. Huels, and L. Sanche, *Resonant formation of DNA strand breaks by low-energy (3 to 20 eV) electrons*, Science **287**, 1658–1660, 2000.
- [141] X. Pan, P. Cloutier, D. Hunting, and L. Sanche, *Dissociative electron attachment to DNA*, Phys. Rev. Lett. **90** (20), 208102, 2003.



## thanks...

For those who have no more time left to read:

Thanks to all the people without whose support this thesis would not have been possible.

And for those who like a bit more detail:

I am happy to have had the chance of joining our small research group that seemed to belong everywhere - officially to the IPP in Garching, historically to the FHI in Berlin, and experimentally to BESSY II (or now HZB) at the other end of Berlin.

Thanks to Uwe, the head of this group, for having the master plan on his mind and for spending so much engagement on it throughout the whole time. It was rewarded with some nice publications. Thank you for giving me this challenging opportunity of letting a new experiment grow up under my hands and performing up-to-date research by exploring a so young process.

Thanks to all the other group members as well. Although being quite different individuals, we played in one team when it came to beamtimes. After my experiences from the past, I felt relieved to find sociable colleagues and a harmonic atmosphere to work in.

Thanks to Alex who had a smile to spend whenever he came around. :-)

Thanks to Toralf who was always willing to lend a helpful hand. Without all our discussions on design details and your help in the construction, the new magnetic bottle would probably not have worked out in time.

Thanks to Marko for his contribution in constructing the new water cluster source as well as some other bits and pieces, and for simulating the argon spectrum.

Thanks to Tiberiu for analysis and help in interpretation of the results on Ne-Kr. I really appreciated that you made some time available for discussions or solving problems available whenever needed, as well as giving me valuable advice for the thesis.

Thanks to Hans-Peter who decided to work with us instead of enjoying his retirement, sharing his useful experiences with us.

Thanks to Markus from AG Becker - our joint beamtime was a real success.

And when it comes to make a degree out of it - thanks to Prof. T. Möller for supervision on the part of the Technical University Berlin.

Thanks to Raimund - the idea of joining you as a post-doc was a good source of motivation to getting this final step of the PhD done.

Thanks to my friends, close by and far away, for being there and sharing their time with me, helping to fill life with more than just working and sleeping. No doubt I enjoyed that!

Special thanks go to my parents, who always believed in me, encouraged me till the very end and supported me in any possible way. You are the best parents I could wish for.

And last but not least: Thanks to Oliver, who had to cheer me up so often during the months of writing. Without your love this work might not have completed. I am so happy to have you.